REPORT DOCUMENTATION PAGE

Form Approved
OMB No. 0704-0188

1. AGENCY USE ONLY *(Leave blank)*	2. REPORT DATE	3. REPORT TYPE AND DATES COVERED
	9 Jan 97	

4. TITLE AND SUBTITLE
Doppler Radar Investigation of Tornadic and Lightning Producing Storms In Northeast Colorado

5. FUNDING NUMBERS

6. AUTHOR(S)
Richard Michael Lucci

7. PERFORMING ORGANIZATION NAME(S) AND ADDRESS(ES)
Colorado State University

8. PERFORMING ORGANIZATION REPORT NUMBER
96-115

9. SPONSORING/MONITORING AGENCY NAME(S) AND ADDRESS(ES)
DEPARTMENT OF THE AIR FORCE
AFIT/CI
2950 P STREET
WPAFB OH 45433-7765

10. SPONSORING/MONITORING AGENCY REPORT NUMBER

11. SUPPLEMENTARY NOTES
~~Unlimited~~

12a. DISTRIBUTION AVAILABILITY STATEMENT

Unlimited

12b. DISTRIBUTION CODE

13. ABSTRACT *(Maximum 200 words)*

14. SUBJECT TERMS	15. NUMBER OF PAGES	
	151	
	16. PRICE CODE	

17. SECURITY CLASSIFICATION OF REPORT	18. SECURITY CLASSIFICATION OF THIS PAGE	19. SECURITY CLASSIFICATION OF ABSTRACT	20. LIMITATION OF ABSTRACT

DISCLAIMER NOTICE

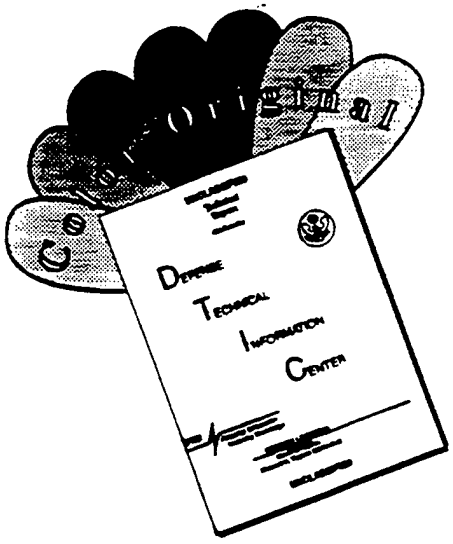

THIS DOCUMENT IS BEST QUALITY AVAILABLE. THE COPY FURNISHED TO DTIC CONTAINED A SIGNIFICANT NUMBER OF COLOR PAGES WHICH DO NOT REPRODUCE LEGIBLY ON BLACK AND WHITE MICROFICHE.

THESIS

DOPPLER RADAR INVESTIGATION OF TORNADIC AND LIGHTNING PRODUCING STORMS IN NORTHEAST COLORADO

Submitted by

Richard Michael Lucci

Department of Atmospheric Science

In partial fulfillment of the requirements

for the Degree of Master of Science

Colorado State University

Fort Collins, Colorado

Summer 1996

COLORADO STATE UNIVERSITY

May 31, 1996

WE HEREBY RECOMMEND THAT THE THESIS PREPARED UNDER OUR SUPERVISION BY RICHARD M. LUCCI ENTITLED DOPPLER RADAR INVESTIGATION OF TORNADIC AND LIGHTNING PRODUCING STORMS IN NORTHEAST COLORADO BE ACCEPTED AS FULFILLING IN PART REQUIREMENTS FOR THE DEGREE OF MASTER OF SCIENCE.

Committee on Graduate Work

Richard E. Eykholt

Michael T. Montgomery

Adviser

Department Head

ABSTRACT OF THESIS

DOPPLER RADAR INVESTIGATION OF TORNADIC AND LIGHTNING PRODUCING STORMS IN NORTHEAST COLORADO

Kinematic, microphysical, and electrical characteristics of two multi-cell thunderstorms observed in northeast Colorado were investigated using single- and dual-Doppler radar and cloud-to-ground (CG) lightning data. These particular thunderstorms were chosen because of their generation of weak short-lived tornadoes and CG lightning dominated by positive flashes. Storm data was collected using the multiparameter, CSU-CHILL, and the National Center for Atmospheric Research (NCAR) Mile High Doppler radars. Various radar analysis methods were employed in an effort to infer origins of rotation, tornado formation mechanisms, and the storm structure responsible for the observed lightning patterns. Single-Doppler techniques included multiparameter measurements, calculations of azimuthal shear, histogram analyses, a study of constant altitude and vertical cross-section data, and an examination of the unedited reflectivity and radial velocity fields. Dual-Doppler data was used to synthesize the three-dimensional wind field.

The synoptic, meteorological conditions in which these thunderstorms developed were found to be similar to those referred to as a High Plains "day 2" scenario. In the first case study, a thunderstorm cell initially produced moderate rates of negative CG lightning and then ceased CG activity as the cell underwent rapid intensification. This cell later

produced three positive CG flashes upshear of the main reflectivity core and generated a weak tornado (gustnado) along its outflow boundary. Dual-Doppler data revealed intense updrafts in excess of 40 m s^{-1}. The positive flashes and initial generation of the shear-induced vorticity were found to be concurrent with the formation of hail-induced downdrafts. An azimuthal shear feature associated with the formation of the gustnado was tracked and no apparent link was found to the mid-level mesocyclone.

The thunderstorm of the second case study produced persistent dominant CG flashes of positive polarity. A column of positive differential reflectivity (Z_{dr}) was used to infer the presence of a strong updraft containing supercooled droplets which contributed to the formation of a large ice and hail mass aloft. A unique hail curtain extended from this region to the surface, along the edge of the main updraft, producing an intense region of horizontal shear which spawned an observed tornado. The existence of a well- organized and intense updraft was believed to be the primary ingredient necessary to produce the observed lightning patterns and weak tornadoes not associated with a mid-level mesocyclone for both case studies.

Richard M. Lucci
Atmospheric Science Department
Colorado State University
Fort Collins, CO 80523
Summer 1996

ACKNOWLEDGMENTS

I would like to express my appreciation to my adviser, Dr. Steven A. Rutledge, for his guidance, patience, and encouragement during my program of study. I thank Dr. Michael T. Montgomery and Dr. Richard E. Eykholt for serving on my advisory committee and for expertly reviewing this thesis. I wish to thank the CSU-CHILL radar staff for their assistance and for providing data, especially Pat Kennedy and Dave Brunkow. I am grateful to NCAR/ATD for furnishing the MHR and KFTG radar data and NCAR/RAP for the spotter reports. My fellow students in the "radar meteorology group" were especially helpful during the past two years for not only their assistance, and advice but also for their companionship: especially Larry Carey, Walt Peterson, Terry Schuur, Tom Saxen, and Jon Erdman. I am indebted to Paul Hein for his computer system administration and valuable support in using a vast array of computer hardware and software. The U. S. Air Force officers, also in this graduate program, provided much needed and appreciated camaraderie while assigned away from an Air Force installation. I deeply thank my wife, Cynthia, and two boys, Matthew and Jared, for their unfailing love, constant encouragement, patience, and sacrifice during many long hours of study and research. Finally, I thank God for His grace and mercy that allowed me to endure through the many challenges encountered while completing this degree.

The U. S. Air Force supported this research under its Air Force Institute of Technology (AFIT) graduate meteorology program and paid all salary and tuition costs.

TABLE OF CONTENTS

CHAPTER 1

INTRODUCTION

1.1 Background

Radar observations made by single and multiple Doppler radars combined with numerical simulations have clarified certain aspects concerning the initiation and maintenance of mid-level storm-scale rotation (mesocyclones) associated with supercell thunderstorms. It has been found that the updrafts within supercells usually begin to rotate as a result of tilting of low-level horizontal vorticity associated with strong vertical shear of the environmental winds (Klemp, 1987). An early promise of Doppler radar has been the detection of tornadoes and the determination of wind speeds (Atlas, 1963). Unfortunately, knowledge concerning the dynamics and generation of tornadoes has not progressed as rapidly as once believed possible. This is due in part to the inability to collect high spatial and temporal resolution data in the vicinity of these vortices over a period encompassing its complete life-cycle (Wakimoto and Atkins, 1996). Previous studies, such as those conducted by Burgess (1976), focused on the mesocyclone as the main source of the tornado's vorticity. Mesocyclones were felt to be of particular importance for tornadogenesis due to their detection by Doppler radars at mid-levels and the subsequent observation of a tornado at the surface. In fact, in a study of 37 storms containing mesocyclones, Burgess discovered that mesocyclones preceded the occurrence of tornadoes in all the storms which produced observed tornadoes.

In recent years, a greater awareness of nonmesocyclone tornadoes, especially those located along low-level intersecting boundaries, has been investigated (Wakimoto and Wilson, 1989). Although these tornadoes are usually weaker than those directly associated with mesocyclones, they have been shown (Fujita, 1979) to cause fatalities and significant property damage and therefore represent a significant weather hazard. The specific mechanisms involved in the origination of these vortices were beyond the data resolution of this thesis. However, the observations presented herein will serve as another "piece of the puzzle" as researchers attempt to better understand and predict this phenomenon.

Upon initial investigation into the case studies presented in this thesis, it was found that the thunderstorms examined produced an abnormally high percentage of positive cloud-to-ground lightning. Previous studies have indicated that lightning flashes which lower positive charge to the earth's surface typically constitute only a small fraction of the total cloud-to-ground lightning (Fuquay, 1982; Reap and MacGorman, 1989). It has been noted that positive cloud-to-ground flashes are sometimes dominant in severe thunderstorms that produce tornadoes and large hail (Rust et al., 1985; MacGorman and Burgess, 1994; and others). Since cloud-to-ground lightning data is readily available to both researchers and forecasters on a real-time basis, a correlation between lightning observations, Doppler radar data, and the likelihood of tornado occurrence could prove invaluable to improving the lead time for severe weather warnings given to the general public. Again, without high spatial and temporal in situ measurements, this present study can only expect to add to the existing research and infer additional evidence of a correlation between abnormal lightning patterns and severe weather.

1.2 Overview of Data

This thesis consists of the investigation of two separate storms involving weak nonmesocyclone tornadoes and dominant positive cloud-to-ground lightning fractions. Lightning data for both case studies was provided by the National Lightning Detection Network (NLDN) consisting of a network of magnetic direction-finding antennas concentrated throughout the continental United States. Several antennas are located in the vicinity of northeastern Colorado adding to the confidence of these observations. The tornado locations in both cases were confirmed either through chase team, local spotter, or general public reports.

Radar data for the first case study of 23 July 1993 was obtained from the Colorado State University (CSU) CHILL and National Center for Atmospheric Research (NCAR) Mile High (10 cm wavelength) Doppler radars. Measurements of horizontal reflectivity (Z_h) and radial velocity (V_r) were obtained. Three-dimensional winds were synthesized from the radial velocity data provided by this dual-Doppler radar configuration.

Radar data for the second case study of 7 June 1995 was obtained primarily from the CSU-CHILL radar. The National Weather Service (NWS) WSR-88D Doppler radar (KFTG) located at the Denver International Airport (KDIA) provided an overview of the thunderstorm morphology. Although the investigation of this case study was constrained to a single-Doppler analysis, additional insight was gained through the use of the CSU-CHILL's polarimetric-diverse capabilities. The radar data used in this thesis provided indications of the bulk hydrometeor and kinematic properties of these storms, and in conjunction with the lightning data, provided insight into storm electrification processes.

This thesis is organized into six chapters. Following this introductory chapter, Chapter 2 contains background material on the theories of nonmesocyclone tornadoes and storm electrification. Chapter 3 offers detailed information on the processing and analysis of radar data along with theories concerning the Doppler radar detection of tornadoes. The first case study of a multi-cell tornadic thunderstorm is presented in Chapter 4. The second case study is presented in Chapter 5, where a very unique storm configuration was observed. A discussion of the results of the analyses are presented in Chapter 6, including some recommendations for further research.

CHAPTER 2

STRUCTURE AND THEORIES OF NONMESOCYCLONE TORNADOES AND STORM ELECTRICITY

2.1 Nonmesocyclone Tornadoes

Tornado formation is not restricted to supercell thunderstorms. Doswell and Burgess (1993) define the single distinguishing characteristic of a supercell as the presence of a deep, persistent mesocyclone. Since classic supercells probably account for the majority of violent tornadoes, past conceptual models of tornadoes concentrated on the mesocyclone as the precursor to tornado formation. This close relationship between the mesocyclone and tornado points to the conservation of angular momentum as an explanation of these types of tornadoes. Nevertheless, supercell tornadogenesis is certainly more complicated than the simple "spin up" of the mesocyclone through low-level frictional interaction with the ground (increasing low-level convergence resulting in a concentrated vortex) and the cascade of energy down to the tornado.

Tornadoes do not occur exclusively from mesocyclones. Also, most mesocyclones do not spawn tornadoes. Burgess et al. (1993) claim that statistics from 20 years of Doppler radar operation in Oklahoma indicate that only 30 to 50% of detected mesocyclones produce tornadoes. With the advances and implementation of a nationwide Doppler radar network, the fraction of storms with a radar-detectable mesocyclone is larger than was previously identified (Burgess et al., 1993).

Figure 2.1 illustrates a widely adapted model of a supercell by Davies-Jones (1986) which suggests two locations for possible tornadogenesis. The first is associated with the mesocyclone and located within the hook echo. The second possible location for tornadogenesis in a supercell is along the flanking line at the leading edge of the rear-flank downdraft. Wakimoto and Atkins (1996) observed the latter in the Newcastle, Texas tornado, on 29 May 1994, during the Verification of the Origins of Rotation in Tornadoes Experiment (VORTEX). They speculate that without high-resolution radar data and ground chase teams, the Newcastle tornado may have been mistakenly classified as a tornado collocated with a parent mesocyclone.

Although nonmesocyclone tornadoes are generally weaker and shorter-lived than their mesocyclone counterparts (Wakimoto and Wilson, 1989 and Davies-Jones, 1986), they are still capable of inflicting significant damage and fatalities (Fujita, 1979). Documented case studies show damage estimates can be as high as F3 (Fujita, 1981) with nonsupercell tornadoes (Wakimoto and Wilson, 1989). Wakimoto and Wilson also suggest that a large fraction of nonmesocyclone tornadoes may go undetected by radar beyond ranges of 50 km and with marginal warning lead times. This is due to the resolution limits of the radar, the rapid development and dissipation of the tornado, and the typical upward refraction of a radar beam, thus preventing low-level rotation to be observed at longer ranges.

The classification of nonmesocyclone vortices is not simple and is a controversial topic. Examples of several categories of "nonsupercell" moist convective vortices are the landspout, in an analogy with the waterspout (Bluestein, 1985); cold air funnels (Cooley, 1978); gustnadoes, small scale, short-lived vortices developed along a thunderstorm gust front or outflow boundary; and a variety of fair weather vortices (relatively long-lived funnel

clouds associated with ordinary cumulus or dissipating cumulus clouds) (Doswell and Burgess, 1993).

2.1.1 Origins of Rotation

The proposed mechanisms by which nonmesocyclone convective vortices arise are considered in this section. Even though nonsupercell tornadoes have been studied for several years, the previous mind-set has been that these vortices are weak and small and do not pose a serious threat to property or mankind. The origin of rotation has been focused primarily on the supercell's mid-level storm-scale rotation center (mesocyclone).

It is generally accepted that all tornadoes form through the amplification of either existing or locally created vorticity (Davies-Jones, 1986). The origin of this existing vorticity is the fundamental difference between nonmesocyclone- and mesocyclone-associated tornadoes. Forbes and Wakimoto (1983) proposed that some vortices develop in response to boundary-layer vorticity generation associated with horizontal shears from microbursts' outflow boundaries. Brady and Szoke (1989) and Wakimoto and Wilson (1989) suggested that nonmesocyclone preexisting vertical vorticity is generated by horizontal shear instabilities associated with surface convergence boundaries even prior to cloud formation. Supercells, on the other hand, create their own parent vortex and boundary during the storm's mature stage.

Wakimoto and Atkins (1996) concluded that the Newcastle tornado first developed as a low-level shear feature along a flanking line. Evidence of preexisting vortices on convergence boundaries from Doppler radar has been documented by Wilczak et al. (1992) and such preexisting vortices may be argued to be associated with "dark spots" observed on the sea surface before the occurrence of a visible waterspout (Wakimoto and Wilson, 1989).

Regardless of the exact mechanism of vorticity generation, most researchers agree that most nonmesocyclone tornadoes have their origin in the pre-tornadic boundary layer vorticity.

2.1.2 Theories of Tornadogenesis

The tornado's concentrated vorticity must originate from the local amplification of generated or preexisting vorticity. Hence, the focus on nonmesocyclone tornadogenesis should be on the processes enhancing the low-level vorticity. The vector form of the vorticity equation can be expressed as

$$\frac{d}{dt}\vec{\omega}_a = (\vec{\omega}_a \cdot \vec{\nabla})\vec{u} - \vec{\omega}_a(\vec{\nabla} \cdot \vec{u}) + \frac{\vec{\nabla}\rho \times \vec{\nabla}p}{\rho^2} + \vec{\nabla} \times \frac{\vec{\mathcal{F}}}{\rho} \tag{2.1}$$

Equation (2.1) states that the rate of change of the absolute vorticity following the motion is given by the sum of the four terms on the right called the vortex tilting term, the vortex tube stretching or divergence term, the solenoidal or baroclinic term, and the frictional term. The only term in the vorticity equation which can be responsible for a rapid intensification (exponential growth) is the stretching term. Numerous case studies have concluded that tornadogenesis has occurred through the amplification of this vertical vorticity through stretching (Bluestein, 1985; Wakimoto and Wilson, 1989; Wilczak et al., 1992; Wakimoto and Atkins, 1996). This rapid amplification through stretching is a common final step in both the popular nonmesocyclone- and mesocyclone-associated tornadogenesis theories.

Surface convergence and the resulting updraft is the primary mechanism for the vortex stretching and intensification into tornadoes. Wakimoto and Atkins (1996) showed that when the initial shear feature of the Newcastle tornado became collocated with a strong updraft, rapid and intense stretching resulted in an F3 tornado despite the absence of a mid-level mesocyclone.

Wilczak et al. (1992) also cited that although stretching was important during the formation of a Colorado nonmesocyclone tornado, the tilting of horizontal vorticity had a comparable magnitude and was present near the rotation center prior to tornado formation. The formation mechanism for this case appears more complicated than in the simple model and combines some characteristics of both mesocyclone and nonmesocyclone tornadogenesis.

2.2 Storm Electricity and Lightning

Lightning is one of the most impressive and most common severe weather events on earth. In periods of undisturbed weather, the fair weather electric field is directed downward toward the earth's surface with a negatively charged surface and a positively charged upper atmosphere. For a lightning stroke to occur, a buildup of intense regions containing opposite electrical charges must exist within the storm. Breakdown potential must be reached and electrical charge is exchanged within the cloud or to the ground by means of the lightning stroke. Exactly how this charge separation occurs is still not totally understood and several competing theories exist, even after many years of scientific examination.

2.2.1 Electrification Theories

The theories of thunderstorm charge separation can be classified into two broad categories: (1) convective charging hypothesis and (2) charge separation associated with precipitation processes (non-inductive and inductive). Since these theories are still somewhat speculative, their popularity has fluctuated over time. There may be no unique mechanism for charging under all conditions and several mechanisms may possibly operate simultaneously within the cloud.

The convective theory is originated in the positive space charge of the fair-weather electric field. This positive charge is transported upward with the developing updraft and initially results in a positively charged convective cloud (Vonnegut, 1963). The cloud then attracts negative ions that become trapped on cloud particles around the edges of the cloud forming a negative screening layer. Instead of neutralizing the positive space charge within the cloud, the downdrafts strip off the screening layer and transport negative charge to lower parts of the cloud as the updraft continues to carry positive ions higher in the cloud. The lower negative charge results in liberation of positive ions by corona from the Earth's surface. These positive ions move under the influence of the electric field and are also transported into the updraft core resulting in a positive feedback cycle. Upon investigation, Williams (1989) found that this theory does not adequately account for a typical thunderstorm's charge structure nor can it produce lightning on time scales similar to those of a developing thunderstorm. This theory also does not explain the pronounced electrical activity associated with mixed-phase precipitation.

Precipitation theories exchange charge between particles in various states by non-inductive (Takahashi, 1978; Saunders et al., 1991) and inductive processes (Illingworth and Latham, 1977). To date, the non-induction charging mechanism appears to be the most promising method of thunderstorm electrification (Williams, 1989). Laboratory studies of Takahashi (1978) found that the magnitude and sign of charging during the riming process was dependent on both temperature and liquid water content (LWC) at temperatures below -10°C. At temperatures between 0° and -10°C, positive charging occurred regardless of the LWC. Figure 2.2 shows the dependence of the charge transferred to the rimer on temperature and LWC. Smoothed contours connect points of equal magnitude with the

shaded area representing the LWC and temperature which produced a negative charge on the rimer. This figure illustrates that at temperatures colder than -10°C, the rimer is positively charged at either low or very high LWCs.

In the mixed-phase region of the thunderstorm, collisions between graupel and small ice crystals place negative charge on the graupel and positive charge on the ice crystals which are transported into the upper portions of the storm by convective updrafts. This results in the normal tendency for the main positive charge to be located above the main negative charge region as depicted in Fig. 2.3. Below the charge reversal temperature, which is some threshold between -10° and -20°C, positive charge is placed on the descending graupel and negative charge on the rising ice crystals which may then contribute to the main negative charge region. The descending graupel produce a small positive charge region below the main negative charge center as they fall below the height associated with the charge reversal temperature. The resulting charge distribution of a main positive charge over a negative charge and a lower positive region is in good agreement with the observed tripole structure of thunderstorms (Williams, 1989).

Takahashi (1978) calculated that an electric field of 300 kV m^{-1} (breakdown potential) could be generated within 5 minutes which is consistent with the time of the first observed lightning discharge after the first echo is detected on radar. When the LWC is small, the electrification will also be small due to a modest number of ice crystals. When the LWC is large, the graupel will not be highly electrified consistent with the observations that lightning is a rarity in clouds dominated by warm rain processes (Williams, 1989). Williams concluded that among the current electrification theories, the non-inductive mechanism should be considered the most feasible charge separation mechanism for deep convection.

Through both laboratory and field observations, Williams stressed the importance of the mixed-phase region for charge separation.

According to the induction theory, cloud and precipitation particles become polarized in the presence of a fair-weather electric field with the lower part positively charged and the upper part negatively charged. When these particles and cloud droplets or small ice crystals collide and rebound, the smaller particles become positively charged and the larger ones become negatively charged. The larger negatively charged particles settle in the lower portion of the cloud while the smaller positively charged particles are transported into the upper portion creating a positive dipole structure within the cloud. Illingworth and Latham (1977) concluded that liquid-liquid induction charging is not capable of producing charge separation of the magnitude observed in thunderstorms. They noted that since the induction mechanism needs a high frequency of collisions and rebound, ice-ice induction is a more powerful charging mechanism. Gaskell (1979) demonstrated that the relaxation times to conduct charge through ice is perhaps too long to produce a significant charge transfer. Possibly the induction process becomes more applicable after the non-inductive process has worked to develop a strong enough electric field to polarize the hydrometeors.

2.2.2 Association Between Positive Cloud-to-Ground Lightning and Severe Storms

Lightning can be classified as intracloud lightning (in-cloud, cloud-to-air, and cloud-to-cloud) and cloud-to-ground (CG) lightning in which at least one stroke of the lightning spans from the cloud to the ground. CG lightning can be further separated into lightning which lowers positive charge to the ground (positive CG lightning) and that which lowers negative charge (negative CG lightning).

Although the majority (over 90%) of CG flashes are negative, positive CG lighting was observed to sometimes dominate the lightning activity in severe tornado-producing or large hail-producing thunderstorms (Rust et al., 1985). In a study by MacGorman and Burgess (1994), positive ground flashes dominated during either the pre-tornadic or tornadic phases of the storms they studied. Reap and MacGorman (1989) also noted a high correlation between large densities of positive CG lightning and severe weather, especially large hail. High fractions of positive CG lightning have also been observed in the stratiform cloud regions of mesoscale convective systems (Rutledge and MacGorman, 1988; Rutledge et al., 1990; Engholm et al., 1990) and in winter thunderstorms (Takeuti et al., 1978) (although flash rates are much less than in summer storms).

MacGorman and Nielsen (1991) suggested two reasons why positive CG lightning might occur in severe storms. First, the observed charge distribution in thunderstorms (positive charge situated above negative charge in a dipole-like fashion) might be tilted by storm or environmental shear such that the upper positive charge (contained on the ice crystals) is effectively exposed to the ground. Using detailed, polarimetric radar data, Carey and Rutledge (1996b) concluded that the cause of high-percentage positive CG lightning in severe storms they studied is the positively charged ice crystals at the top of tilted precipitation cores (tilted dipole). Strong electric fields aloft were identified by patterns in the differential phase data, and were argued to be consistent with the advection of positive charge from the storm's upper levels. A second mechanism proposed by MacGorman and Nielsen (1991) was a possible region of positive charge in the lowest part of the thunderstorm, beneath the main negative charge, produced through the charge reversal conditions of the non-inductive charging mechanism (Williams, 1989). MacGorman and

Burgess (1994) propose that a significant positive region can be formed in a region between 0° and -15°C by an increased number of recirculated graupel collisions through the advection of graupel from the same or nearby cells. Rutledge and MacGorman (1988) and Engholm et al. (1990) also presented substantial evidence in favor of the tilted dipole hypothesis in explaining positive CG lightning in both summer and winter convective storms.

Stolzenburg (1994) suggested that the production of dominant positive CG lightning is associated with exceptionally tall storms during a period of rapid vertical increase in storm radar echo height which is coincident with large hail production. A storm that produced an F5 tornado in Plainfield, Illinois, on 28 August 1990 had a 91% dominance of positive CG lightning during its development (Seimon, 1993). During this period, large hail and four smaller tornadoes (F0 to F2) were produced. Coincident with the F5 tornado touchdown, the dominant CG flash polarity reversed from positive to negative after a 20-minute-span of reduced CG lightning activity. MacGorman and Burgess (1994) emphasized that the correlation between positive CG lightning and severe storms is valid only in the forward direction, noting that severe weather frequently occurs in storms dominated by negative flashes as well.

2.3 Lightning Data Collection

Observations of CG lightning used in this thesis were obtained from the National Lightning Detection Network (NLDN). The lightning detection system senses CG lightning through a network of wideband magnetic direction-finders (DF) located throughout the contiguous United States. Each DF system consists of two orthogonal magnetic-loop antennas, a flat-plate electric field antenna, and associated electronics to process the incoming signals. One loop antenna is oriented north-south and the other east-west. The

ratio of the voltage induced in the east-west loop from the lightning's magnetic field to the voltage induced in the north-south loop is proportional to the tangent of the azimuth to the flash. The flat-plate antenna is used to determine the polarity of the flash and so resolve the 180° ambiguity in direction inherent in the system when the current direction is unknown. The electronics of the system accepts only those field waveforms (rise time, width, and peak structure) that are characteristic of CG return strokes and rejects intracloud flashes. When two or more DFs detect a flash, the network's central processor (position analyzer) uses all of the incoming information to plot the optimum ground-strike location

The archived NLDN data contain information about polarity, location, time, peak current, and number of return strokes (multiplicity). Krider et al. (1980) propose that peak current and multiplicity are good indicators of the severity of the discharge under most conditions. Flash times are reliable to within 6 ms and ground-strike locations accurate to within 1 to 2 km. The network has a detection efficiency of 70 to 90% (Orville, 1991). Evaluations by MacGorman and Taylor (1989) have shown that the DFs correctly discriminate between positive CG and intracloud flashes when the lightning occurs within 600 km of a direction finding site. All CG lightning data used in this thesis easily satisfy this spatial requirement and therefore provide high confidence in the polarity and location measurements. Detailed information on the DFs and network configuration can be found in Orville (1991) and Orville et al. (1983).

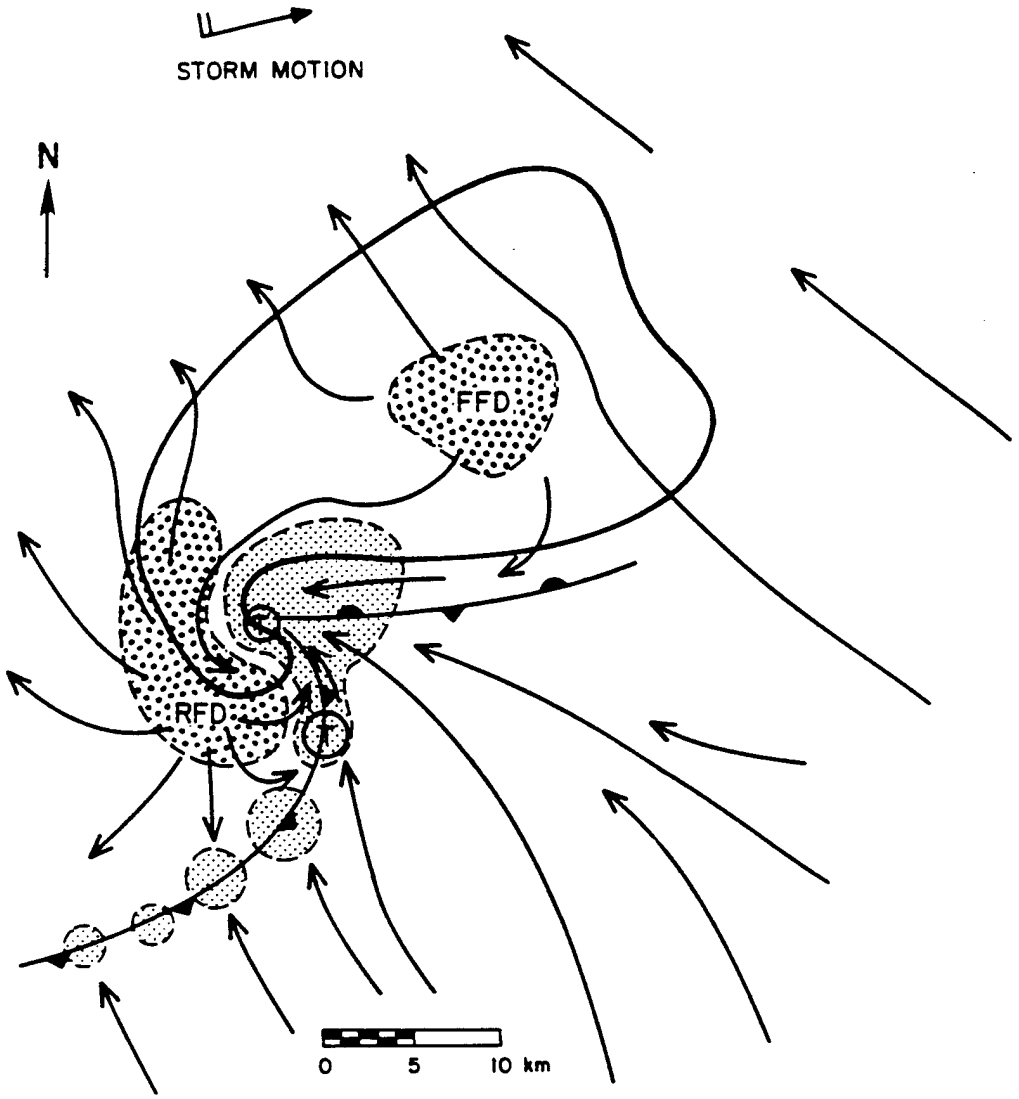

Fig. 2.1 Schematic of a supercell thunderstorm at the surface (Davies-Jones, 1986). The solid contour encompasses the radar echo. The gust front is depicted using conventional frontal symbols. Lightly shaded regions show surface updraft positions. FFD is the forward-flank downdraft and RFD is the rear-flank downdraft. Streamlines are ground-relative. Encircled T's depict likely tornado locations.

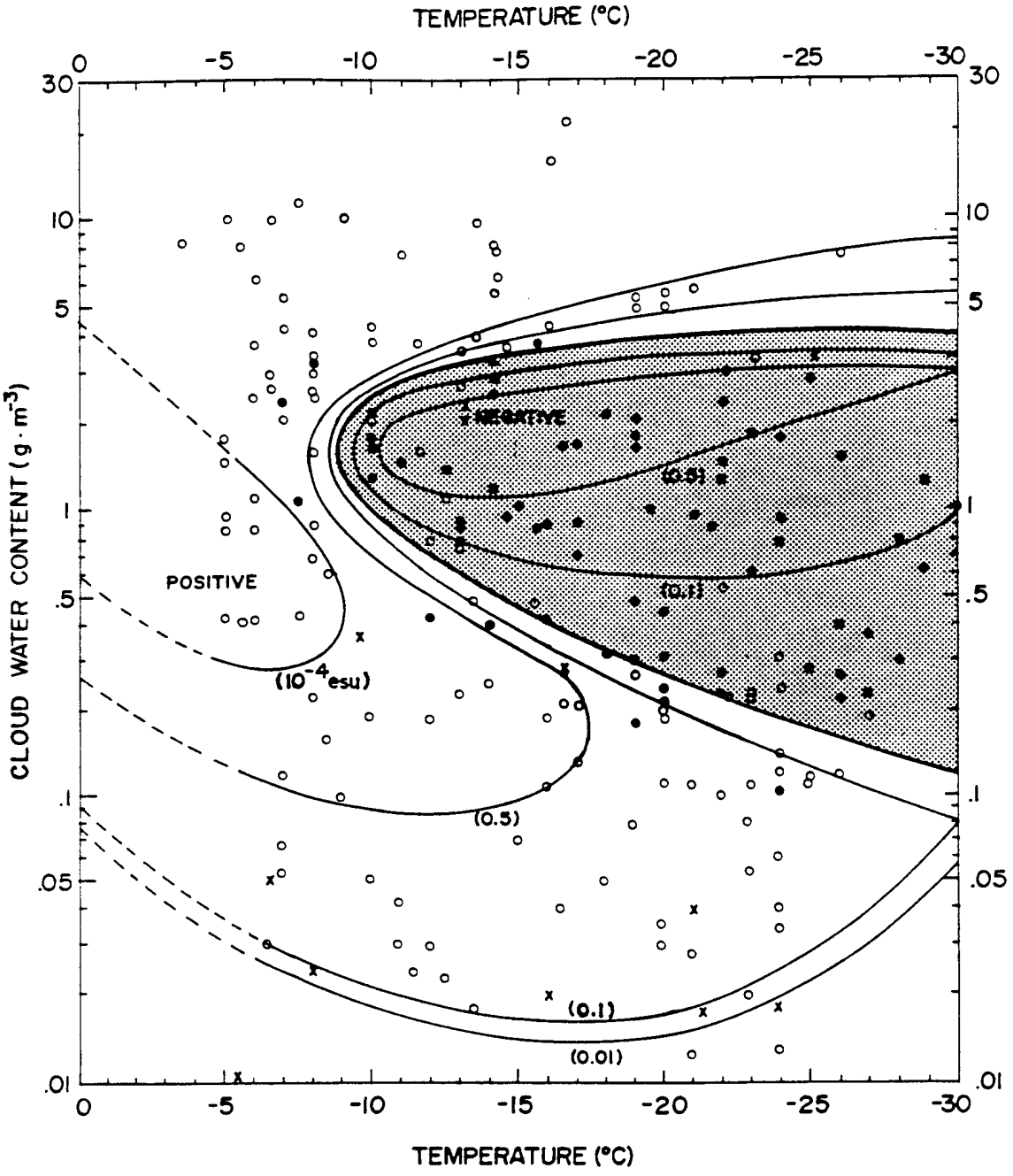

Fig. 2.2 Electrification of rime as a function of temperature (°C) and cloud water content (g m^{-3}) for the laboratory experiments of Takahashi (1978). Solid circles depict negative charge, open circles positive charge, and crosses uncharged cases. The shaded area represents negative rime charging. The amount of electric charge of rime, on a single collision with an ice crystal, is shown in units of 10^{-4} esu.

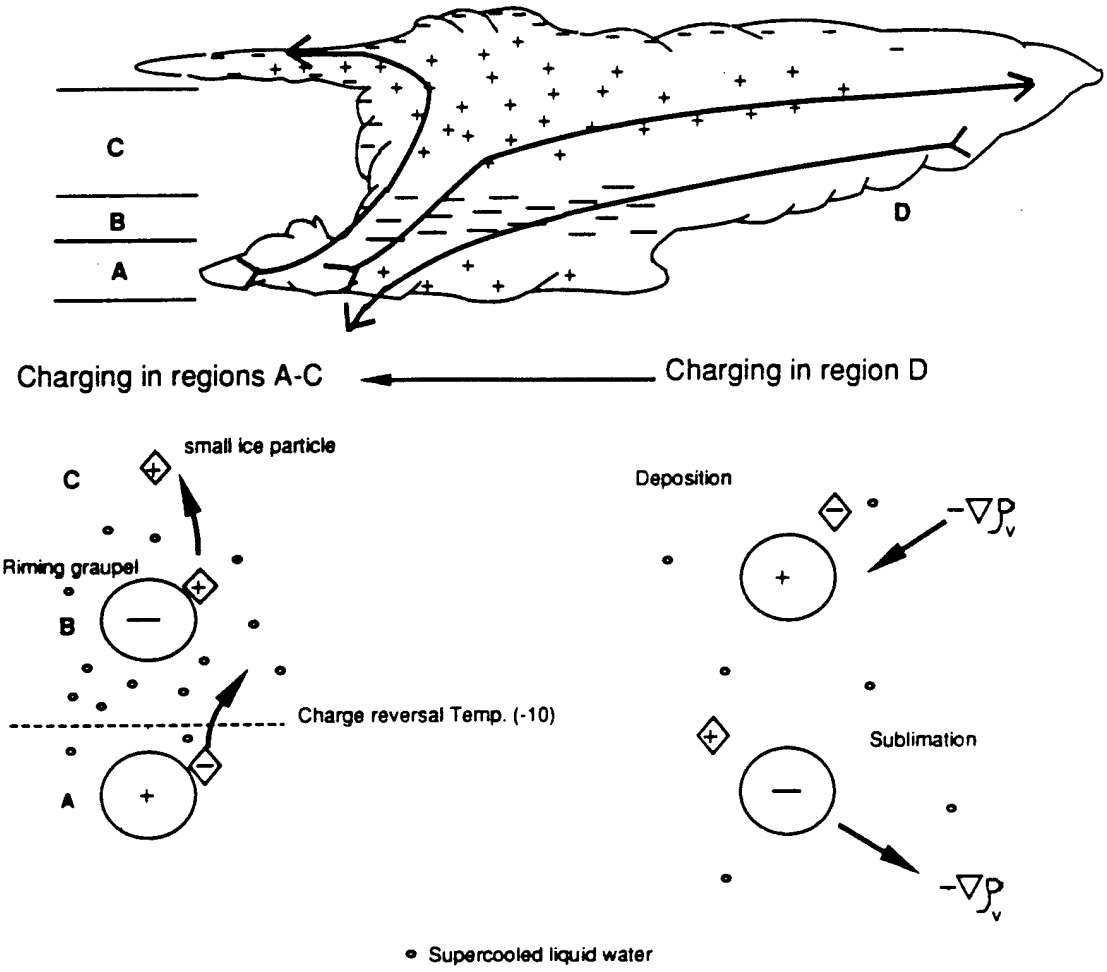

Fig. 2.3 Model of non-inductive charging processes for graupel-ice particle collisions in the presence of supercooled liquid water (Peterson, 1992). The lower boundary of region B represents the charge reversal level (T_R = -10° to -20°C). Negatively charged graupel remains in region B at a level where the updraft velocity equals the graupel's terminal velocity (particle balance level). Updrafts carry positively charged ice crystals into the upper levels of the storm (region C). In region A, graupel and/or small hail have grown large enough to fall below the charge reversal temperature and are charged positively during collisions.

CHAPTER 3

RADAR OBSERVATIONS AND ANALYSIS

3.1 Data Collection and Processing

All radar data used in this thesis was stored using the radar Universal Format (UF) (Barnes, 1980) and retrieved from 8 mm Exabyte magnetic tape cartridges. Processing of the data was accomplished on a Sun SPARC workstation. S-band (10-11 cm wavelength) radar data was obtained primarily from the Colorado State University (CSU) CHILL dual-polarization Doppler radar. The National Center for Atmospheric Research (NCAR) Mile High Radar (MHR), a previous test bed for the Next-generation Radar (NEXRAD), was used to produce a dual-Doppler three-dimensional wind field analysis of the first case study on 23 July 1993. Data from the National Weather Service's WSR-88D in Denver (KFTG) was used to look at a broad overview of the storm in the second case study of 7 June 1995, while the CSU-CHILL was operating primarily in a sector scan mode. MHR and KFTG data tapes were obtained from NCAR. A synthesis of the two-dimensional low-level wind field was also produced using data from the CSU-CHILL and KFTG.

All radar data were viewed and interactively edited in polar coordinates using the Research Data Support System (RDSS) software developed by NCAR. The reflectivity field was edited to remove any contamination from ground clutter, second-trip echoes, and three-body scattering signatures (Doviak and Zrnić, 1993). Doppler radial velocities were first thresholded on mean received power and then edited to remove aliased velocities and any

of the aforementioned contaminations. The power threshold used ranged from -112 to -114 dBm depending on how "clean" the data appeared. Special care was taken to avoid eliminating data and to ensure that both temporal and spatial continuity were maintained.

The edited radar data fields were then interpolated to a common three-dimensional Cartesian grid using the REORDER software developed by Dick Oye and Michele Case at NCAR. The interpolated grid resolution was different for each case study and for each set of radar data. For the 23 July 1993 case, both the horizontal and vertical grid resolution was 0.5 km. With the CHILL radar's data, a radius of influence for the Cressman interpolation scheme (Cressman, 1959) was fixed at 0.9 km in all dimensions while the MHR's radius of influence was fixed at 0.9 km in the horizontal and increased to 1.45 km in the vertical. This increase was necessary to slightly smooth the vertical interpolation because the MHR scanning strategy (13 unique elevation tilts from 0.5° to near 20°) produced a lower vertical data resolution than did the CHILL. For the 7 June 1995 case, the grid resolution for the CHILL data was 0.25 km in the horizontal and 0.5 km in the vertical since the storm in question was less than 40 km from the radar. The radius of influence in the horizontal and vertical was fixed at 0.4 km and 0.6 km respectively. The KFTG data for this case was more coarse since the WSR-88D was operated in a precipitation scanning mode (nine unique elevation tilts) versus the severe weather mode. This called for a grid resolution of 1.0 km in all dimensions and the use of a radius of influence which varied with range. This variable radius of influence is multiplied by the range causing the number of gates used in the interpolation of a grid point to increase with range. The variable radius values used in this case were 1.0 for the azimuthal component and 1.5 for the vertical. From the interpolated Cartesian grids, various constant altitude plan position indicator (CAPPI) plots, vertical

cross-section plots, and dual-Doppler syntheses were generated to aid in the analysis of the storms.

3.2 Analysis Methods

Both single- and dual-Doppler methods were used in this study. A dual-Doppler analysis was accomplished where possible. The criteria for using dual-Doppler methods will be discussed in Section 3.2.2.

3.2.1 Single-Doppler Observations

Single-Doppler analysis methods were employed to make quantitative use of the radial velocity information when dual-Doppler solutions were not feasible. A FORTRAN program was developed to calculate the beam-to-beam azimuthal shear of the Doppler radial velocities prior to interpolation. Azimuthal derivatives were numerically calculated using a "three point" finite difference approximation. The application of the azimuthal shear calculations will be discussed in detail in Section 3.3.

Another single-Doppler analysis method used was the three-dimensional histogram plot (Yuter and Houze, 1995) of the interpolated radar reflectivity. These three-dimensional histogram plots or CFADs (contoured frequency altitude display) provide a statistical summary of the precipitation echo by showing the percent of frequency of occurrence of a reflectivity value at a given height. To produce the plot, a normalized histogram of the desired data was computed for each Cartesian grid level in the volume. These histograms were then stacked in a plot with height as the ordinate and the analyzed field as the abscissa. The data were then contoured in 5% increments starting with 5%. Additionally, a 1% contour is included to show the behavior of the outliers. Since the histogram is normalized at each level, some information about the shape and size of the storm is lost but the resulting

plots are easier to interpret. This plot method is useful for many radar measured variables and was also utilized to examine the dual-Doppler derived vertical wind field.

3.2.2 Dual-Doppler Analysis Procedures

The determination of the three components of the wind velocity from the mass continuity equation and precipitation particle radial velocity data from two Doppler radars was first extensively investigated by Armijo (1969). When using only two Doppler radars, it is necessary to assume that the particle terminal fall-speed (V_t) is known so that the two equations for the radial components of velocity supplemented with the mass continuity equation form a set of three equations and three unknowns (*u, v,* and, *w*):

$$V_1(x,y,z) = \frac{1}{R_1}[(xu + yv + z(w + V_T)] \tag{3.1}$$

$$V_2(x,y,z) = \frac{1}{R_2}[(x - x_2)u + yv + z(w + V_T)] \tag{3.2}$$

$$\frac{\partial u}{\partial x} + \frac{\partial v}{\partial y} + \frac{\partial w}{\partial z} = kw, \tag{3.3}$$

$$\text{where} \quad \left.\begin{aligned} R_1 &= \sqrt{x^2 + y^2 + z^2} \\ R_2 &= \sqrt{(x - x_2)^2 + y^2 + z^2} \\ k &\approx -\frac{\partial(\ln p)}{\partial z} \end{aligned}\right\}. \tag{3.4}$$

In practice, the derivation of the three-dimensional wind field was accomplished using the batch version of the Custom Editing and Display of Reduced Information in Cartesian Space (CEDRIC) program (Mohr and Miller, 1983). The process involved in determining the three-dimensional wind field consists of 1) initially synthesizing the horizontal winds using the two radial velocity measurements, 2) iteratively calculating the vertical motion by downward integration of the anelastic continuity equation accounting for particle fall speeds, and 3) adjusting the horizontal wind components with each successive iteration and computing a new divergence field. A more specific procedure is outlined below.

Once both radar volumes were edited and interpolated to a common Cartesian grid, CEDRIC was invoked in a batch processing mode using an appropriate input file. To account for differential storm motion between the lower and upper radar scans, the data was advected to a common time. Storm speed and direction were determined by examining the previous and subsequent CSU-CHILL radar volumes and noting the movement of the low- to mid-level reflectivity features. Radial velocities from both radars were then combined to compute a first estimate of the u and v component winds. At this stage the vertical velocity was assumed to be zero.

Next, the velocity data was thresholded for geometry considerations. All velocity data was removed from regions where the beam crossing angle, β, was less than about 30° according to the relation:

$$\frac{\sigma_u^2 + \sigma_v^2}{\sigma_1^2 + \sigma_2^2} = csc^2\beta \equiv b, \tag{3.5}$$

where σ_u^2 and σ_v^2 are the error variances of the u and v estimate, σ_1^2 and σ_2^2 are the single-Doppler mean velocity error variances of the two radars, and b is the input parameter accepted by CEDRIC (Davies-Jones, 1979). The value of b was set to 3.75 which corresponds to a minimum beam crossing angle of 31.1°. This value of β would correspond to an error variance in the dual-Doppler estimate that is nearly four times the combined velocity error variance from both radars. Assuming a typical error of 1 m s^{-1} in the velocity field of both radars (Doviak and Zrnić, 1993), a possible combined dual-Doppler error variance of $\sigma_u^2 + \sigma_v^2 = 7.5$ m s^{-1} would be expected.

A 2-step Leise filter (Leise, 1981) was performed on the derived horizontal wind field damping out all wavelengths shorter than four times the horizontal grid spacing. Fall speeds were then created to be used to correct the initial synthesized horizontal wind field. This was

accomplished using the following density weighted Z-V_T relationship:

$$V_T = -\exp(0.1z)^{0.4} aZ^b, \tag{3.6}$$

where a and b are constants set to 2.6 and 0.107 above the freezing level and 0.817 and 0.063 below the freezing level and the exponential term is a correction due to air density changes.

CEDRIC then uses the initial terminal fall-speed corrected u and v fields for a given level and calculates the w field by continually iterating and updating the horizontal wind to match the new vertical velocity until a numerical convergence threshold of 0.005 m s^{-1} is satisfied. The iteration is performed top down, one level at a time, using the w field from the level above as a boundary condition. The upper boundary condition is set to $w = 0$ m s^{-1} at the storm echo top. Bohne and Srivastava (1975) show that a downward integration is preferred because the errors associated with the wind estimates are decreased since the air density decreases exponentially with height. No lower boundary condition is specified since the low level convergence field cannot be accurately estimated due to a typical lack of data near the surface and all errors are assumed to be outside the analysis region.

Although an error analysis was not performed in this study, Nelson and Brown (1987) estimate that the updraft speed in strong updrafts (>20 m s^{-1}) is accurate to within about 10%. Four major sources of error were investigated by Nelson and Brown (1987): Storm advection and evolution, incomplete sampling of low-level divergence caused by upward refraction of the radar beam, top boundary errors, and the effect of uneven terrain on the low-level divergence. They concluded that none of these sources appeared to be a dominant error source. Doviak and Zrnić (1993) further discuss errors derived from dual-Doppler measurements to include the use of an incorrect Z-V_T relationship and contaminated signals from echoes received through sidelobes of the radar beam.

3.3 Tornado Detection by Doppler Radar

Atlas (1963) and Lhermitte (1964) speculated that a pulsed Doppler radar with a high pulse repetition frequency (PRF) and its beam centered on a tornado would display a velocity spectrum of great width spread equally across zero velocity. While that was likely to be true for a stationary beam wider than the vortex and centered on it, most contemporary Doppler radars rotate at a constant revolution and operate at a moderate PRF.

For a given wavelength (λ), the maximum unambiguous velocity (v_{max}) is proportional to the PRF (Battan, 1973):

$$v_{max} = \pm\lambda \cdot \text{PRF}/4 \tag{3.7}$$

However, a high PRF results in a limited round trip distance for a pulse before the next pulse is transmitted since the maximum range (r_{max}) is inversely proportional to PRF:

$$r_{max} = \tfrac{1}{2} \cdot c/\text{PRF} \tag{3.8}$$

where c is the speed of light.

A more typical Doppler radar is configured for longer ranges with a more moderate PRF. Therefore, one would expect tornadic wind speeds to be aliased, making it extremely difficult at times to decipher the maximum wind speed (Brown et al., 1978). Prior to the study of the Union City, Oklahoma, tornadic storm of 24 May 1973, it was thought that a tornado could not be detected without a detailed inspection of the Doppler velocity spectra (Brown et al., 1978). However, in a detailed study of that storm, a unique mean Doppler velocity signature, the tornado vortex signature (TVS), was discovered (Burgess et al., 1975). This unique and characteristic signature of extreme azimuthal shear (in excess of 50×10^{-3} s^{-1}) first appeared aloft 33 minutes before tornado damage was evident on the surface.

Tornado detection by Doppler radar is highly dependent on the distance of the vortex from the radar, the radar beam's pulse volume placement relative to the tornado center, and the aspect ratio between the core radius of the vortex and the beamwidth of the radar. The first dependence is easily explained since tornadoes are best defined in the lower portions of the storm. A radar will detect rotation from a nearby storm but will overshoot a signature from a more distant storm due to the Earth's curvature and the typical upward refraction of the radar beam (Burgess et al., 1993). To better understand the second two detection dependencies, Zrnić developed a model that simulated a Doppler radar looking at a Rankine combined vortex (Zrnić and Doviak, 1975). The Rankine combined vortex (Rankine, 1901) is characterized by essentially two flow regimes (Fig. 1). In the first regime, the tangential velocity increases linearly from the center outward to a velocity maximum at the vortex edge, under the assumption of solid body rotation. Outside the core, the second flow regime is that of a potential vortex where the velocity decreases by an amount inversely proportional to the distance from the core center. Figure 3.1 shows that the core region is easily identifiable by Doppler radar by azimuthally separated velocity peaks of opposite direction and that the outer potential flow regime is difficult to detect (Lemon et al., 1978). The Rankine vortex model seems appropriate for tornadoes based on in situ measurements in waterspouts and dust devils (Brown et al., 1978).

Brown et al. (1978) extensively looked at the relationship between the TVS, radar pulse volume placement, and the aspect ratio between the pulse volume and vortex. Their results are shown in Figs. 3.2 and 3.3 and represent mean Doppler velocities within sampling volumes as a function of azimuthal distance from the vortex center. They point out that the most striking feature is the extreme mean Doppler velocity values that occur near one-half

beamwidth on either side of the tornado when the pulse volume is centered on the vortex. Also evident is that as the azimuthal separation of the extreme values increase, their magnitudes decrease and become negligible at a range of a few pulse depths from the tornado. For a pulse volume centered on a tornado, Fig. 3.4 shows that the azimuthal separation of the extreme values is not significantly affected by the beamwidth-to-vortex core radius. However, the signature amplitude, which is more important in TVS detection, is greatly affected. Brown et al. (1978) point out that a TVS would not be detectable unless the peak-to-peak Doppler velocity shear is somewhat greater than any background cyclonic shear produced by a parent circulation or surrounding shear. They place a typical shear value threshold for detection at a magnitude of 10×10^{-3} s^{-1}.

Other practical limitations exist in the detection of a TVS. Since radar data is collected at discrete azimuthal increments, the extreme velocity values may be missed when the sampling interval is greater than the beamwidth. Zrnić and Doviak (1975) have also shown that the effective radar beamwidth can be broadened for an antenna rotating rapidly relative to the sampling time. Burgess et al. (1993) point out that not all tornadoes, even at close range, will have a TVS since detection is a function of tornado size and strength as well as radar pulse volume and spatial density. They estimate that the maximum detection range for large tornadoes (1-2 km diameter) is not much more than 100 km and narrow tornadoes (10-50 m diameter) may escape detection at a range of only 20 km. Wakimoto and Wilson (1989) suggest that many nonmesocyclone tornadoes may be undetectable by radar with the detectable ones limited to a maximum range of near 50 km and with marginal warning times. They point out that convergence boundaries, which often spawn nonmesocyclone tornadoes, are often detectable at ranges up to 100 km or beyond.

Although there is no objective criteria established for defining a TVS, Brown et al. (1978) developed five tentative guidelines that appear to work well. These guidelines are as follows:

1) an azimuthal shear of at least 10×10^{-3} s^{-1} over a distance of one beamwidth

2) a signature with opposing Doppler velocities (after removal of TVS translation)

3) a shear region of not more than about 1 km in length to distinguish a small-scale vortex from a shear line

4) a shear region of at least several kilometers in vertical depth

5) persistent detection for about 10 minutes or more at the same general height

Wakimoto and Wilson (1989) define a TVS as a beam-to-beam azimuthal shear (at the same range gate) of $\geq 25 \times 10^{-3}$ s^{-1} for beams with a 1° separation. They also specify that the opposing velocity values must be local maxima. It is important to realize that the TVS is only a qualitative signature and can only be used to crudely estimate tangential velocities when the tornado's core radius is accurately known (Brown et al., 1978). Without additional information about the tornado's size, the TVS alone cannot be used to determine either the maximum velocity of the vortex or its size.

Although detection through Doppler velocity measurements is more reliable, many valid tornado warnings have been issued with only radar reflectivity signatures such as "hook echoes" and bounded weak echo regions (BWER) (Burgess et al., 1993). Forbes (1981) found that although detection through the presence of a hook-shaped appendage of a convective echo had moderate false alarm ratios, there was a low probability of detecting a hook echo in a tornadic storm. He also discovered that many hook echoes were absent through about three quarters of the tornadic storm's lifetime and often appeared only after a

tornado had already been present. The BWER, when present for a substantial time interval, is a reliable indicator of supercell thunderstorms which are known to produce a majority of strong and violent tornadoes (Lemon, 1980). When observed in the horizontal, the BWER is identified by a region of diminished reflectivity surrounded by higher reflectivity. In the vertical, the highest echo top capping the BWER is known to be the location of the supercell's intense, sustained updraft (Browning and Ludlam, 1962). Criteria for identification of a BWER, established by Lemon (1980), based on a three-dimensional reflectivity structure, is considered to be the most reliable indicator of a tornado in environments supportive of supercell formation without the use of Doppler velocity measurements (Burgess et al., 1993).

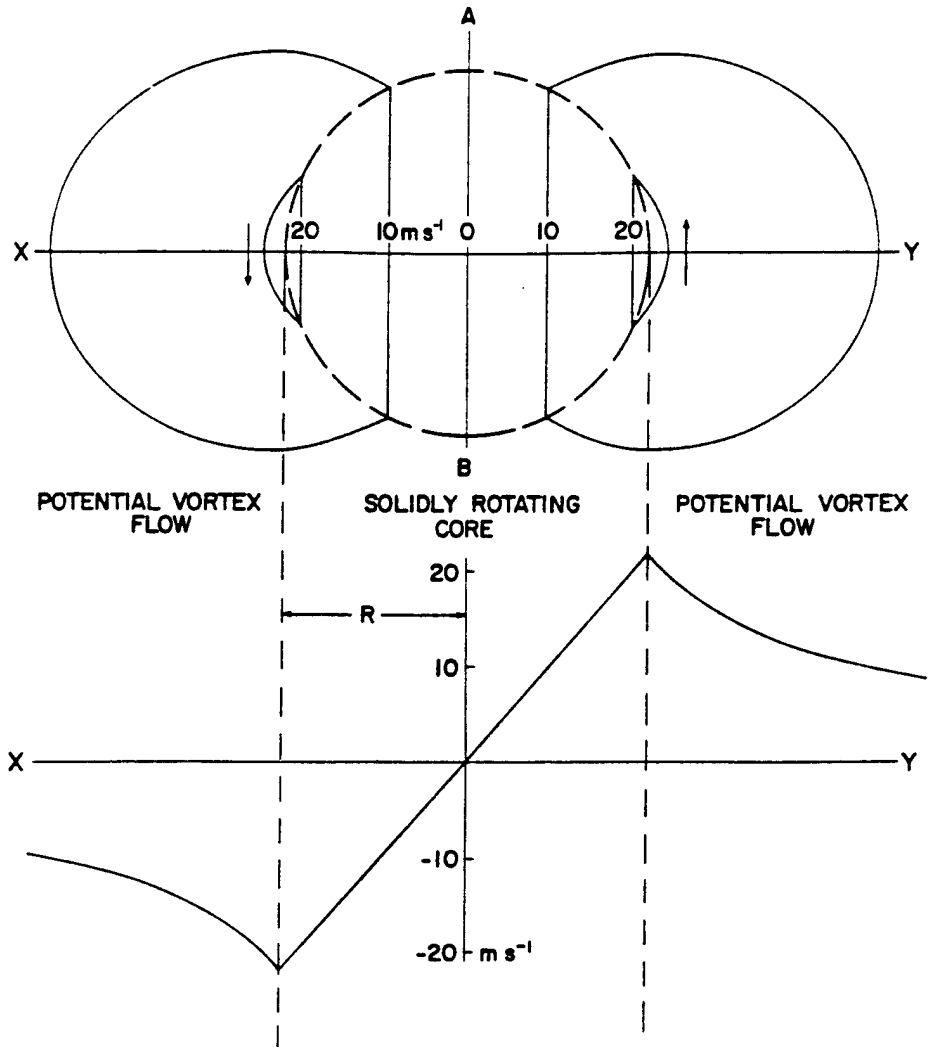

Fig. 3.1 Top: Doppler radar velocity signature of a stationary Rankine combined vortex, where line XY is at a constant range from the radar (Lemon et al., 1978). Bottom: Tangential velocity profile along the XY axis. Positive velocities are away from the radar and negative toward (assuming the position of the radar is below the bottom of the page).

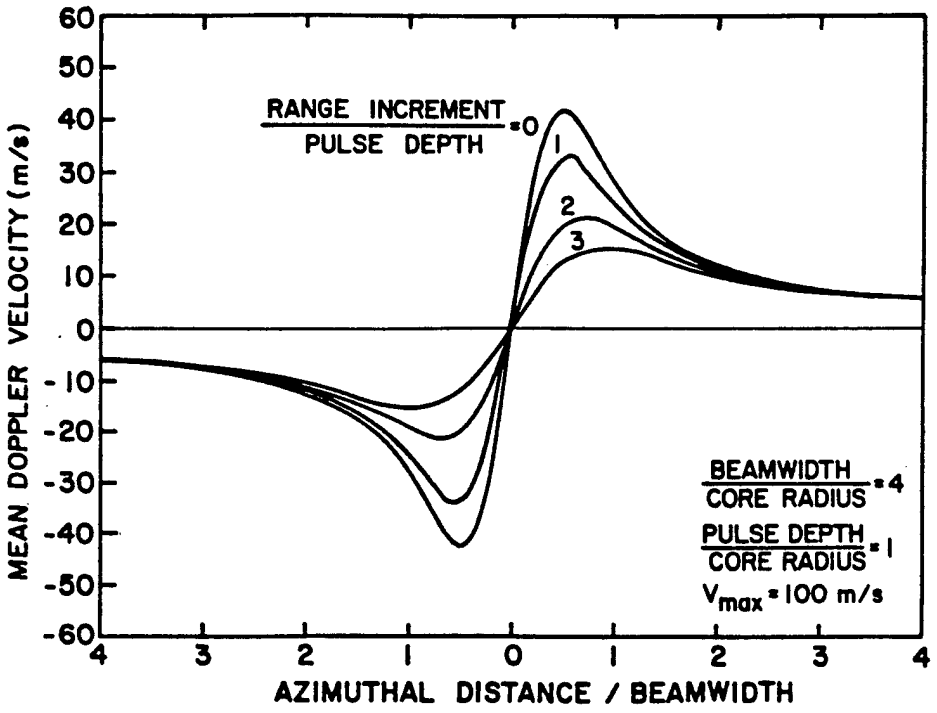

Fig. 3.2 Simulated azimuthal profile of a tornado vortex signature at various normalized ranges from the tornado center (Brown et al., 1978). Pulse depth to beamwidth ratio is 0.25. Maximum tangential velocity in the vortex is 100 m s^{-1}.

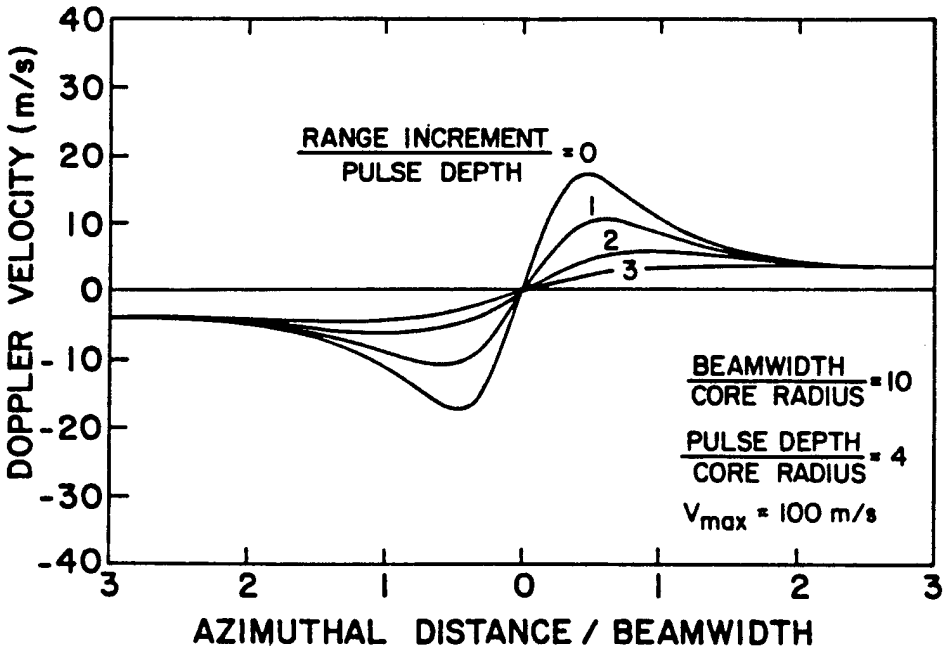

Fig. 3.3 As in Fig. 3.2 except for different radar sampling and tornado characteristics shown (Brown et al., 1978). Pulse depth to beamwidth ratio is 0.4.

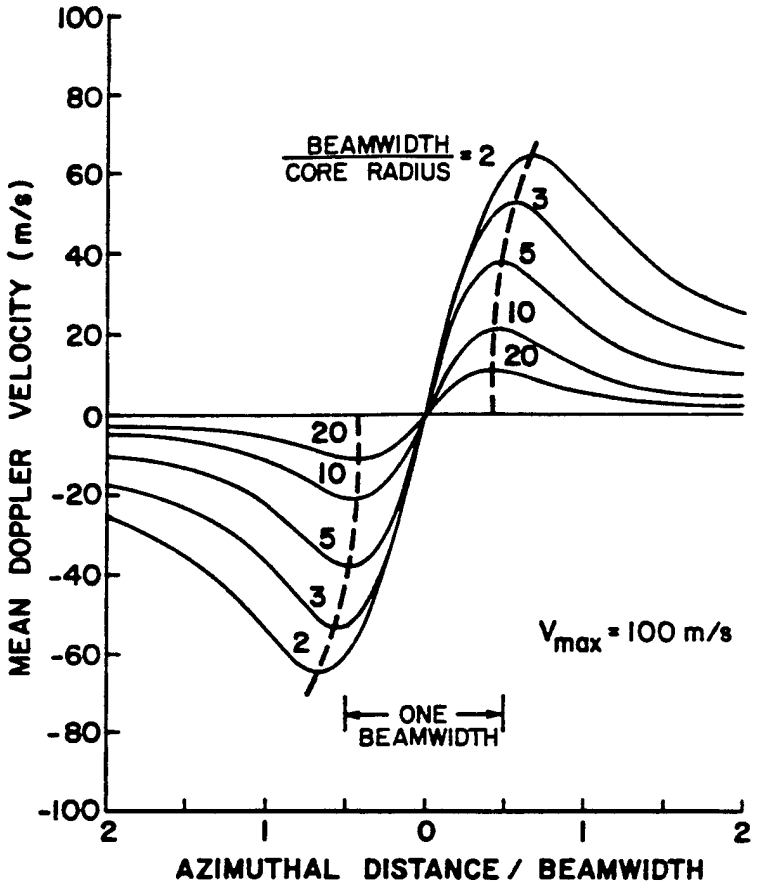

Fig. 3.4 Simulated azimuthal profiles through the center of a tornado vortex signature for various ratios of beamwidth to core radius (Brown et al., 1978). Maximum tangential velocity in the vortex is 100 m s^{-1}. Pulse depth to beamwidth ratio is 0.15.

CHAPTER 4

CASE STUDY 1: GUSTNADO

This chapter describes the kinematic and electrical characteristics of a severe multi-cell thunderstorm in northeastern Colorado, on 23 July 1993. This particular day in northeast Colorado and southeast Wyoming was characterized by thunderstorms with tops exceeding 50,000 ft, producing heavy rain, large hail (up to 7 cm diameter), and numerous short-lived weak tornadoes (Goodge, 1993). The particular thunderstorm under investigation produced some hail, anomalous CG lightning, and an observed weak (F0) tornado near Gilcrest, Colorado (see Fig. 4.1). The anomalous CG lightning in this case occurred during a period when the storm produced only three positive CG flashes and no negative CG flashes in the previous 24 minutes. Both single- and dual-Doppler radar techniques have been utilized to investigate this storm and its associated CG lightning (from NLDN data) as well as the evolution of the tornado. This tornado has been classified as a gustnado; a short-lived vortex occurring along a gust front (Bluestein, 1993).

4.1 Synoptic Conditions

The meteorological conditions of 23 July 1993 resembled closely those described by Doswell (1980) in explaining a typical High Plains severe thunderstorm episode. Doswell reported that severe weather on the High Plains tends to occur on several days in succession and under relatively moderate conditions as far as severe weather parameters are concerned. It is interesting to note that severe weather was widespread in northeastern Colorado on the

previous two days. Fig. 4.2 illustrates the meteorological conditions at the surface at 1200 UTC [local time (MDT) is UTC - 6] on 23 July 1993. A weak surface cold front passed through northern Colorado on 22 July and had become semi-stationary through southern Colorado. Surface wind prior to the onset of convection was light-to-moderate and generally out of the southeast along the Front Range providing weak upslope. Surface moisture was relatively high in the region with dewpoint temperatures around 10°C (50°F).

At the 500 mb level (Fig. 4.3), the main trough axis was located upstream near the Nevada-Utah border with a thermal trough in western Colorado providing slight cold air advection along with some moisture advection into the region. A short-wave ridge was just to the northeast of Colorado while a short-wave trough was west of the Four Corners region providing weak positive vorticity advection into Colorado. The 500 mb flow to the east over North Platte, Nebraska, was in excess of 30 m s^{-1} (60 kt.).

Strong convergence was present at the 200 mb level (Fig. 4.4) as northeast Colorado was under the left-rear entrance region of a jet streak. However, by 0000 UTC, Fig. 4.5 indicates that the flow aloft had become more divergent as another jet maximum propagated in from the west. Upper level divergence did not appear to have been a significant factor since weak convergence was present in several High Plains severe weather cases examined by Doswell (1980).

The Denver 1200 UTC rawindsonde observation (Fig. 4.6) showed a conditionally stable atmosphere with a weak surface inversion and a near-isothermal layer from 690 to 620 mb. The moisture content was moderate from the surface up to 300 mb with a mid-level drier layer corresponding to the near-isothermal layer. Directional shear was evident in the lowest layers with winds generally from the west above 600 mb with weak speed shear up

to 200 mb. Modifying the sounding to represent the maximum surface heating (28°C) produced only moderate values of convective available potential energy (CAPE) around 1600 J kg^{-1} and values of vertical shear (over the lowest 6 km) less than 6 m s^{-1}. The Denver 1200 UTC hodograph (Fig. 4.7) showed some veering of the winds in the lowest layer with backing in the mid-levels. Above 500 mb there was little directional shear with only a slight increase in speed.

The Platteville, Colorado wind profiler (Fig. 4.8) suggested a diurnal shift in the low-level winds to the southeast after 1600 UTC confirming the slight upslope flow along with weak shear in the lowest 1500 m. No other significant features are present with this profiler data.

By conventional parameters, this synoptic situation would not be conducive of severe thunderstorms. It does, however, exhibit many of the synoptic conditions noted by Doswell (1980) in his attempt to identify indicators associated with the occurrence of severe weather on the High Plains. Namely, there existed a surface frontal boundary to the south, surface dewpoint temperatures were greater than 7.2°C (45°F), 500 mb flow was greater than 10 m s^{-1}, and forcing from low-level upslope flow was present to compensate for the weak-to-modest instabilities.

4.2 Radar Analysis

The investigation of this storm incorporated both single- and dual-Doppler analyses. From the dual-Doppler data, three-dimensional histograms of reflectivity and vertical velocity were constructed. Azimuthal shear was examined near the time of the gustnado formation. This analysis focused on twelve edited CSU-CHILL radar volumes with a temporal resolution of 6 minutes. Corresponding radar volumes from the NCAR MHR were

used to compute dual-Doppler solutions of the three-dimensional wind field. For standardization, all distance measurements and directions will be referenced with the CSU-CHILL radar as the origin.

4.2.1 Storm Morphology

During the late afternoon hours of 23 July 1993, a severe multicellular thunderstorm developed and passed within 20 km south of the CSU-CHILL radar. This storm produced some hail (as reported by spotters), an anomalous CG lightning pattern, and a brief gustnado near Gilcrest, Colorado. Figures 4.9 through 4.14 present the low-level reflectivity pattern of the storm at 6-minute intervals from 2241 to 2347 UTC. These figures are in the form of a constant altitude plan position indicator (CAPPI) taken at 1.5 km above ground level (AGL). Plotted with the reflectivity is the detected CG lightning activity which occurred during the 6 minutes it took to complete one radar volume scan. The lightning observations will be addressed briefly and will be discussed in detail in a later section.

Figure 4.9a depicts the storm of interest at its early development stage. At 2241 UTC, the radar image showed two distinct cores of 45-50 dBZ reflectivity and each appeared to be equally electrified from the perspective of CG lightning production. The northern-most cell will be referred to as cell-1 (X= -37 km, Y= -21 km) while the core to its southeast (X= -34 km, Y= -25 km) will be referred to as cell-2. By 2247 UTC (Fig. 4.9b), the storm had moved to the east-northeast (propagation speed was approximately 11 m s^{-1}) and had slightly intensified with the core reflectivity above 50 dBZ. Again, both cores appeared to be equally electrified.

The area of >50 dBZ low-level reflectivity at 2253 UTC (Fig. 4.10a) had expanded as both cells continued to intensify. Most of the CG lightning was coincident with cell-1

while each continued to become more distinct. Figure 4.10b shows that cell-2 had undergone explosive growth by 2259 UTC with reflectivities above 60 dBZ. At this time it is evident that all of the CG lightning was associated with cell-1. Both cells continued to split with cell-2 moving to the right of the wind in the lowest 4 km keeping its original speed of near 11 m s^{-1}.

Reflectivities in cell-2 exceeded 65 dBZ by 2305 UTC (Fig. 4.11a) as it continued its eastward trajectory. A weak echo region (WER) was now discernible in the region of the mesocyclone (X= -19 km, Y= -23 km) detected from the radial velocity field (not shown). A flanking line associated with a gust front can be partially seen at the southern edge of the storm (X= -22 km, Y= -28 km). Again, all the CG lightning is associated with cell-1 which has only slightly intensified and did not increase in areal extent. Figure 4.11b shows that cell-2 continued its eastward trajectory, had intensified with a core reflectivity over 68 dBZ, and increased in areal coverage. This reflectivity may have been even higher but possibly experienced some smoothing in the interpolation and contouring process. The flanking line is not evident in this figure or subsequent figures at this height. The absence of the flanking line was also partially due to some masking by a strong flare echo associated with the three-body scattering from large hail (Doviak and Zrnić, 1993) and ground clutter. The flare echo and ground clutter was removed from the reflectivity and radial velocity fields during the editing process. The CG lightning activity was mainly located to the northeast of cell-1 which was moving to the northeast at a slower speed of 8 m s^{-1}. Two negative CG lightning strokes were detected with the development of a cell to the southeast (X= 7 km, Y= -28 km). Up to this point, all CG lightning detected by the NLDN within a 40 km radius of CSU-CHILL has had a negative polarity.

By 2317 UTC, the first indication of any positive CG activity was located in the northern region of cell-2 which did not appear to have intensified, although the areal extent of >45 dBZ reflectivity contour had increased (Fig. 4.12a). This was the first CG lightning of any polarity that could be uniquely associated with cell-2 during the previous 24 minutes. The negative CG lightning cluster which was located to the north became more widespread and less identifiable with a single reflectivity core. For the purposes of comparing lightning signatures between the three main areas of the storm, any cell more closely associated with the negative CG lightning cluster in the northern region of the storm is referred to as cell-1. Tracking the individual reflectivity cores in this region of the storm was more difficult due to the pulsating nature of these cells. During the next 6 minutes, cell-2 produced another (and final) positive CG lightning flash upstream (downshear) of its main core as its intensity reached a maximum for this level (Fig. 4.12b). This cell now became more elongated, the WER (weak echo region) became less conspicuous, and it obtained a slight northward component of travel. A new cell began to develop along the right flank of cell-2 with a reflectivity core just over 50 dBZ, and is referred to as cell-3 (X= 0 km, Y= -25 km). Cell-3 did not produce any detected CG lightning for the next 20 minutes. The negative CG lightning cluster associated with cell-1 became more concentrated and obtained its highest flash rate during the observational period. The cells in this part of the storm continued to fluctuate in intensity.

The next volume scan (Fig. 4.13a) depicts the time and location of the reported gustnado. Cell-2 began its dissipation stage while cell-3 intensified. Neither cell produced any detectable CG lightning flashes during this period. The negative lightning cluster remained fairly steady as the northern region of the storm further evolved. By 2335 UTC

(Fig. 4.13b), cell-3 became more intense than cell-2 as it cut off the low-level inflow into cell-2. Cell-3 produced its first CG lightning stroke and began a northeast path as the CG cluster to the north remained at near steady-state.

In Fig. 4.14a, cell-3 began to produce the majority of the CG lightning as it merged with another cell to its east-northeast. Finally, by 2347 UTC (Fig. 4.14b), cell-1 and associated echo had essentially dissipated and ceased producing CG lightning while cell-3 produced a strong cluster of negative CG lightning with an average of one flash every 10 seconds. Cell-2 continued to weaken and its size diminished. This cell produced only three positive and no negative CG flashes throughout a 60-minute time span.

4.2.2 Single-Doppler Analysis

Selected volumes and elevation scans of "raw" reflectivity and radial velocity were examined near the time of gustnado formation to extract finer detail from the storm that was subdued during the editing and interpolating process. This analysis also gives a flavor of the presentation that would be available to a real-time observer and allows for a more natural display of radial velocity information. Radial velocity data was also used to calculate a beam-to-beam azimuthal shear of the mesocyclone and gustnado.

4.2.2.1 Gust Front and Tornado Vortex Signatures

In this section, unedited radar displays will be examined using the RDSS software to examine the gust front detected in both the low-level reflectivity and radial velocity fields and its temporal and spatial relation to the tornado vortex signature (TVS). Five volumes were scrutinized from 2312 to 2336 UTC. The gustnado occurred at approximately 2330 UTC.

Figure 4.15 depicts the radar display beginning at 2312 UTC and at an elevation angle of 1.1°. The main cell in this scan is cell-2 which was referred to in description of the storm morphology. The gust front is evident, approaching the 210° radial and near the 35 km range ring, depicted as a line of approximately 10 dBZ reflectivity and as a shear zone in the radial velocity field with outbound and inbound velocities of roughly 10 m s^{-1}. There is no concrete evidence of a TVS along the shear zone at this stage. The mesocyclone is not easily pinpointed in this low elevation scan although it is more evident above the 2.4° elevation scan located at 210° and 25 km with the storm tilting eastward with height. Noteworthy is the flare echo from the three-body scattering of large hail visible along the 220° radial at distances greater than 33 km and a "hook echo" extending southward from the main core. Apparent in this and subsequent figures is a second-trip echo identifiable in both the reflectivity and radial velocity fields along the 90° radial. Figure 4.16 shows that the gust front was propagating away from the main cell and into an area of low reflectivity at 2318 UTC. Along the gust front's shear zone, an area of stronger rotation can be inferred from the radial velocity couplet (possible TVS) located at 202° and 26 km. This feature sustained continuity in the next higher elevation scans. Again, the mesocyclone is not readily apparent at this low elevation scan but becomes more distinct at higher elevation tilts. Although not directly investigated in this study, Fig. 4.17 raises the question of the possibility of an unreported tornado along the 205° radial at 27 km given the obvious hook echo reflectivity feature and apparent TVS (small couplet of local maximum inbound and outbound radial velocities). This area has a very low population density so it is quite possible that a tornado could go unreported. This feature may have also represented a strong vortex aloft with no funnel cloud extending to the surface. By 2424 UTC (Fig. 4.18), the

gust front continued to progress farther eastward with a noticeable increase in outbound radial velocities. The hook echo appendage mentioned above had mostly dissipated from the main cell. At a higher elevation scan of 2.4° (Fig. 4.19), the first unquestionable sign of a TVS located along the leading edge of the gust front (190° radial and 23.5 km) became apparent. This signature also clearly existed in the next lower (1.7°) and higher (3.1°) elevation scans (not shown) at precisely the same location showing vertical continuity and meeting the criteria of a vortex defined by Wakimoto and Wilson (1989).

The intersection of the gust front with a developing cell (previously referred to as cell-3) to the east of the main cell is shown in Fig. 4.20 (2330 UTC). This cell appeared to undergo rapid growth probably from enhanced lifting provided by the gust front. Although this is the reported time of the gustnado, it is difficult to distinguish the TVS along the gust front shear zone. The beginning of the dissipative stage of the main cell can also be presumed from the decrease in reflectivity and the decline of the flare echo. Investigating a slightly higher elevation angle of 1.7° (Fig. 4.21) allowed slightly better detection of rotation along the gust front and a possible TVS located at 183° and 25 km. This signature was also visible at the next higher elevation angle. During the next radar volume (2336 UTC), the gust front weakened and became more shallow and coincident with cell-3 (not shown). An explicit TVS was no longer distinguishable from the convergence zone of the gust front and the previous flare echo is completely absent from cell-2.

4.2.2.2 Azimuthal Shear

Azimuthal shear was calculated for three radar volumes prior to and including the time of the gustnado. CAPPI plots were constructed at 0.5 and 1.5 km AGL and vertical cross-sections were taken through the shear feature most likely associated with the gustnado.

Due to software limitations, vertical slices can only be viewed along lines of constant X or Y Cartesian coordinates. Azimuthal shear is contoured in increments of 2 x 10^{-3} s^{-1} with the value of first contour being 4 x 10^{-3} s^{-1} (defined by Wakimoto and Wilson, 1989 as a shear feature). Assuming cylindrical symmetry and solid-body rotation, the vorticity is equal to twice the value of azimuthal shear. Extreme shear values are reduced somewhat after undergoing interpolation. Also, the azimuthal shear field can be quite noisy especially near the edges of valid radial velocity data. Because of the smoothing from interpolation, requirements by other authors that a TVS have values of azimuthal shear exceeding 25 x 10^{-3} s^{-1} (Wakimoto and Wilson, 1989; JDOP Staff, 1979) are not strictly adhered to in this study.

Figure 4.22a and 4.22b show CAPPIs at 2318 UTC. A broad area of greater than 8 x 10^{-3} s^{-1} azimuthal shear existed in the vicinity of the hook echo and WER and are associated with the mesocyclone. Several regions of weaker shear can be seen along a northeast-southwest line, to the southeast of the main cell. Of these, the small shear feature located at X= -9.5 km and Y= -24.0 km is most likely associated with the development of the gustnado 12 minutes after this time (see Figs. 4.23a and 4.23b). This particular feature along the gust front was chosen for its spatial and temporal continuity. The shallow depth of the gust front is evident in these plots with the azimuthal shear located on its leading edge.

At 2324 UTC (Figs. 4.24a and 4.24b), the main area of azimuthal shear had split into two areas. The strongest feature was coincident with the hook echo and had increased in magnitude to over 14 x 10^{-3} s^{-1}. Upon further investigation, although not a direct part of this study, there existed a vertical connection between this vortex and the mid-level mesocyclone above 3 km. Looking back to Fig. 4.22a, one can see that two distinct maxima did exist in

this prominent shear feature. The shear associated with formation of the gustnado is located at X= -5 km and Y= -24 km. Vertical cross-sections plotted in Figs. 4.25a and 4.25b show that this azimuthal shear had propagated slightly ahead of the 15 dBZ reflectivity contour and was approaching the developing cell to the east. Shear values had increased to 8 x 10^{-3} s^{-1} near the surface.

By 2330 UTC (Figs. 4.26a and 4.26b), the azimuthal shear previously identified with the mesocyclone and hook echo began to weaken. The azimuthal shear associated with the gustnado is was located at X= -1 km and Y= -26 km at this time. Figures 4.27a and 4.27b show that this feature was at its highest value of over 14 x 10^{-3} s^{-1} and extended well above 2 km (the contours tilt out of the two-dimensional plane of these figures above 2 km and are not shown). The NCAR chase team that photographed the gustnado was looking to the west and had a Global Positioning System (GPS) location of X= 2.9 km and Y= -24.2 km. This would place the NCAR team at 4.3 km to the east-northeast of the gustnado. Since the image in Fig. 4.1 was cropped and enlarged from the original transparency, there is a high confidence that this azimuthal shear feature was coincident with the actual sighted gustnado.

Although no dual-Doppler vertical motion could be analyzed in this vicinity, the evidence of the vertical growth and strengthening of the implied vorticity suggests stretching in the updraft of the developing thunderstorm as the primary mechanism for the formation of the gustnado. This stretching mechanism is in strong agreement with Wakimoto and Wilson (1989) and Brady and Szoke (1988) who studied tornadoes which originated at low levels as small vortices produced by shearing instabilities along a convergence boundary. Figure 4.28 presents a schematic model of the life cycle of a nonmesocyclone tornado proposed by Wakimoto and Wilson and is consistent with this study.

4.2.3 Dual-Doppler Analysis

Figure 4.29 presents an overview of the region of usable dual-Doppler data between the CSU-CHILL and NCAR Mile High Radar. The two lobes depict the regions where the beam crossing angles are ≥30°. The spatial resolution of the dual-Doppler analysis can be estimated from an expression derived by Davis-Jones (1979): $S=(R\pi\Delta)/180$, where R is the maximum range of the echo from the furthest of the two radars and Δ is the radar half-power beamwidth. Using R=40 km and $\Delta=1°$, the spatial resolution of this analysis is estimated to be approximately S=0.7 km. The data was interpolated to a 0.5 km grid but plotted with a 1.0 km interval. Although this resolution was too large to resolve the small scale rotations, it was able to depict the horizontal and vertical motions on scales relevant to storm electrification. Unfortunately, the gustnado and cessation of CG lightning in cell-2 coincided with the dual-Doppler baseline, hence little or no three-dimensional wind information could be obtained at this time. A further complication remained since there was no MHR volume available for 2336 UTC. Overall, 12 radar volumes were analyzed with dual-Doppler solutions computed for 11 of these volumes. Many horizontal and vertical slices were examined throughout the entire data set although only a select few are included in this thesis. Vector lengths in the dual-Doppler analyses are proportional to the wind speed and are consistent between each figure. Later in this section, three-dimensional histograms are viewed to contrast the evolution of the reflectivity and numerical values of vertical velocity between the three individual cells. Since small scale convective features are not resolvable, the dual-Doppler vertical cross-sections will concentrate on the reflectivity core and mesocyclone region of cell-2 since this cell exhibited an anomalous CG lightning pattern of no negative and three positive CG flashes.

4.2.3.1 The Three-Dimensional Wind Field

Figures 4.30 through 4.35 present some of the key results of the dual-Doppler analyses. The reflectivities indicated on these figures are the maximum value between the CSU-CHILL and NCAR MHR. These reflectivity values were used to derive the first-guess vertical motion field based on the appropriate reflectivity-particle fall speed relationship (3.2) given in Section 3.2.2.

The first detectable sign of any rotation occurred at 2247 UTC (Fig. 4.30). This developing stage of the mesocyclone is most obvious at 1.0 km (X= -28 km, Y= -24 km) although it is also noticeable at 1.5 km AGL. Vertical cross-sections (Figs. 4.31a and 4.31b) show that this area can be characterized by the beginning formation of a WER and strong mid-level updrafts as a possible consequence of the low- to mid-level convergence. By 2253 (Fig. 4.32), the mesocyclone had matured to form a closed circulation (X= -25 km, Y= -23 km) from 0.5 km to 2.5 km AGL. Figures 4.33a and 4.33b show that the echo core was almost entirely composed of strong updrafts. A prominent feature in Fig. 4.33a is the strong upper-level divergence located above the updraft region. These figures show that cell-2 had a high reflectivity core suspended aloft and was tilted with height to the southwest.

The final volume able to depict a complete mesocyclone in the western dual-Doppler lobe occurred at 2311 UTC and is shown in Fig. 4.34. The deformation zone formed by the convergence of the outflow boundary or gust front with the low-level inflow is apparent along the southeast edge of the storm. The mesocyclone in this volume scan is only visible up to 2.0 km AGL. Figures 4.35a and 4.35b show the vertical structure through the core of the mesocyclone. Upward vertical velocity is still dominant through the core albeit somewhat weaker (Y= -22 km). Most noticeable is the formation of strong downdrafts along

the southern edge of the echo core (Y= -25 km) in Fig. 4.35a along with the diverging cold-air outflow region (Y= -27 km). Also recognizable is the shear induced rotation (Y= -26.5 km) along the outflow's leading edge hinting toward the generation of horizontal vorticity which may be tilted along the convergence zone.

4.2.3.2 Three-Dimensional Histogram Analysis

The three-dimensional wind field derived in this study proved more useful toward describing the general kinematics of the storm to better understand the storm's electrification process rather than to detect the origin of rotation of the gustnado. To better manage the three-dimensional nature of the storm, three-dimensional histograms or CFADs (Yuter and Houze, 1995) of reflectivity and vertical velocity were constructed. Each histogram was produced from a rectangular box encompassing most of the low-level (1 km AGL) 30 dBZ contour of each cell. These histograms were normalized at each vertical level to the number of valid data points included at that level. Some shape information is lost through normalization but it makes the plots easier to interpret. This was especially critical for the vertical velocity field as the data became more sparse as the storm approached the dual-Doppler baseline. Reflectivity was binned in 5 dBZ increments from -10 dBZ to 70 dBZ. Again, the maximum reflectivity between to two radars was used in this analysis. Vertical velocity was binned in 2 m s^{-1} increments from -20 m s^{-1} to 40 m s^{-1}. The sign convention used was that positive values refer to upward motion. The percent of occurrence of each field is contoured in 5% increments. A 1% contour is also included to show the behavior of the outliers of the distribution. The 0°C, -20°C, and -40°C levels taken from the 0000 UTC Denver sounding are annotated on each histogram. A bulge in the higher percentage reflectivity contours can usually be detected near the freezing level (radar bright-band) from

the more stratiform regions of the storm. This enhanced reflectivity is due to the transition from ice-phase hydrometeors to water-coated ice to a smaller water droplet as the ice structures melt and collapse.

Figures 4.36 through 4.48 show the three-dimensional histograms of reflectivity and vertical velocity for each of the three cells described in Section 4.2.1 for each radar volume. Vertical velocity histograms for cell-2 are less reliable from 2317 UTC to 2347 UTC due to the proximity of the dual-Doppler baseline. Cell-1 vertical velocity histograms are unreliable after 2330 UTC and cell-3 is not analyzed until 2323 UTC with reliable vertical velocity data available beginning at 2329 UTC.

At 2241 UTC (Fig. 4.36), both cell-1 and cell-2 demonstrated very similar characteristics in reflectivity, vertical velocity, and CG lightning activity. The highest percentage of reflectivity centered around 38 dBZ and was concentrated in the hydrometeor mixed-phase region between 0°C and -20°C. Maximum vertical velocities in both cells were near 25 m s^{-1}, and were in the upper-levels of the storm. In contrast, cell-2 contained mostly updrafts throughout the entire echo core while the reflectivity and vertical velocity distributions implied that strong precipitation-loaded downdrafts were present in the low-levels of cell-1.

Figure 4.37 (2247 UTC) indicates that both cells' maximum reflectivity had increased while the bulk of the higher reflectivities had descended in cell-1 and ascended in cell-2. This was a manifestation of the vertical velocity distributions in which cell-1's maximum vertical velocity decreased while cell-2's vertical velocity increased. Correspondingly, cell-1 maintained an approximate balance of upward and downward motion but cell-2 became dominated by strong updrafts.

By 2353 UTC (Fig. 4.38), cell-1 and cell-2 began to exhibit more distinct kinematic, microphysical, and electrical characteristics. At this time, most of the CG lightning activity was coincident with cell-1. The wider spectrum of reflectivities associated with cell-2 (Fig. 4.38b) could represent a more heterogeneous mixture of hydrometeors, as consistent with strong convective activity. Maximum updrafts in cell-2 had exceeded 40 m s^{-1} at a time just prior to a noted rapid intensification of the echo core. Conversely, the narrower reflectivity spectrum seen in cell-1 began to take on a diagonal characteristic with a rather uniform reflectivity at a given height and an increase of reflectivity downward. This diagonal signature represents a transitional phase of the storm, which is on the way to becoming more stratiform and thus more homogenous in content (Yuter and Houze, 1995). Also consistent with this implication is the domination of upward motion in the upper levels of the cell and downward motion in the lower portion as observed in stratiform-type precipitation (Rutledge et al., 1988)

The next set of histograms (Fig. 4.39) presents a similar situation. Cell-2 had ceased all CG lightning activity and its reflectivity distribution had broadened with maximum reflectivity approaching 70 dBZ through and above the mixed-phase region. It is assumed that concurrent with the reduction of CG flashes and the presence of high reflectivity aloft is the increase of intracloud flash rates. The maximum updraft had subsided slightly in cell-2 but the overall distribution of vertical velocity remained much the same. Cell-1 continued its transition toward a diagonal signature in the reflectivity histogram. A higher frequency of near zero vertical velocity was now evident in cell-1.

Figures 4.40 and 4.41 (2305 and 2311 UTC) present very much the same characteristics as previously noted. Cell-1 continued progressing toward a more stratiform

nature with a narrower spectrum of both reflectivity and vertical velocity. Although maximum reflectivities near the surface have increased in these two time periods, it is evident by the structure of these histograms that cell-2 was beginning its mature stage of development. For the first time, low-level downdrafts became more prevalent (Fig. 4.41d).

Although extreme values of reflectivity still existed at 2317 UTC (Fig. 4.42), cell-2 began exhibiting a trend towards a diagonal signature with a sharp decline in high reflectivities above the mixed-phase region. The mode of vertical velocities had shifted toward negative and had become more narrow as the gust front propagated away from the cell. This period was coincident in time with the first positive CG lightning strikes associated with cell-2. The distributions associated with cell-1 are strikingly similar with the previous two histograms.

Figure 4.43 is very similar to the previous figure. Although cell-1 and cell-2 display similar modal values in reflectivity, cell-2 maintained higher extreme values throughout its vertical extent. Even though cell-2 had exhibited a dissipative trend, it is noteworthy that reflectivities were greater than 50 dBZ, even above the -40°C level in the storm where glaciated conditions must exist. This may be the key to the positive CG lightning detected during this time period as discussed later.

Cell-1 continued to maintain its previous distribution at 2329 UTC (Fig. 4.44) as it continued to produce negative CG lightning. Cell-2's maximum reflectivity uniformly decreased by nearly 10 dB at all levels above 2 km. Figure 4.45 shows the first analysis of cell-3 at both 2323 and 2329 UTC. The initial reflectivity distribution of cell-3 appears to have very similar qualities to the initial analysis of both cell-1 and cell-2. Although the maximum updrafts were not as strong as those produced in cell-1 and cell-2 throughout the

height of the storm, cell-3 did appear to have equally strong updrafts in the boundary layer. These low-level updrafts were proposed in Section 4.2.2.2 as a stretching mechanism in the formation of the gustnado.

An interesting bimodal reflectivity distribution had developed aloft in cell-1 by 2341 UTC (Fig. 4.46). This feature may have been caused by contamination from adjacent cells tilted with height into the analysis region or perhaps the pulsating nature of this region of the storm. The intensity of cell-2 had dramatically decreased although high reflectivities were still present near the surface at this time indicating the presence of moderate to heavy rain.

Figure 4.47 presents the final evolution of cells 1 and 2 at 2347 UTC. Cell-1 still exhibited the bimodal reflectivity distribution at the mid- to high-levels while the maximum reflectivities declined above the freezing level in cell-2. Cell-2 was now located in the eastern dual-Doppler lobe and the vertical velocity distribution shows that the cell was strongly dominated by downdrafts at all levels. At 2341 and 2347 UTC (Fig. 4.48), cell-3 maintained a similar evolution to cell-1 and even displayed the bimodal structure aloft (a similar explanation can be offered for this feature as was given for cell-1). The vertical velocity distribution at 2347 UTC once again implies weak descending motions in the low-levels with ascending air in the mid- to upper-levels.

4.3 Cloud-to-Ground Lightning Observations

An overview of the detected CG lightning was presented along with the storm morphology discussed in Section 4.2.1. This morphology, along with the dual-Doppler analyses and three-dimensional histograms of the previous sections, will be used to propose several explanations for the observed CG lightning characteristics. The main focus in this study is on the anomalous CG activity displayed by cell-2 in which negative CG lightning

ceased followed by a brief production of three positive CG lightning flashes. No intracloud (IC) lightning information was available for this study although some inferences about its frequency of occurrence will be made. Figure 4.49 demonstrates the nature of the storm track CG lightning activity throughout the evolution investigated in this chapter. This figure clearly shows that there was a major difference in the storm electrification between the three thunderstorm cells.

The percent of total CG flashes that lower positive charge has been estimated at 4% for warm season thunderstorms in the United States (Reap and MacGorman, 1989) and only 3% in the northern Rocky Mountain region (Fuquay, 1982). Although most CG lightning lowers negative charge to ground, MacGorman and Burgess (1994) propose two situations where positive CG lightning activity is pronounced: 1) a few positive CG flashes tend to occur as a thunderstorm, which produced predominantly negative CG lightning, begins to dissipate, 2) positive CG flashes may dominate the anvils of severe storms and the trailing stratiform regions of convection as in a mesoscale convective system (MCS) (Rutledge and MacGorman, 1988), while the regions of deep convection in the same storm produce a predominance of negative CG lightning. In a study of 15 severe storms dominated by positive CG flashes, MacGorman and Burgess (1994) found that all storms had some rotation with the majority of them producing tornadoes (this correlation is only valid in one direction). Rust et al. (1981) and Carey and Rutledge (1995 and 1996b) found that positive CG lightning associated with the storm core originated from high on the back side of storm towers, through wall clouds, and from downshear anvils. Price and Rind (1993) suggest that as the distance increases between the negative charge region and the earth, so does the breakdown potential needed for a CG discharge, resulting in a decrease in CG lightning

activity. Conversely, they propose that as the mixed-phase region increases in volume and mass through intense updrafts, so does the electric field within the upper portions of the cloud, resulting in the increase of IC flashes. Stolzenburg (1994) found that in 24 storms studied, the production of a high density of positive CG flashes was associated with a period of rapid increase in radar echo top height.

Observations of the 23 July 1993 case are very similar to previous studies. During the evolution of this storm, cell-2 was the only portion of the storm containing any mesoscale rotation detectable by Doppler radar. From the histograms, cell-2 produced negative CG flashes during the period it exhibited a similar structure to that of cell-1 and cell-3. However, coincident with its rapid intensification (increase in updraft speeds and upward displacement of higher reflectivity values) cell-2 ceased production of CG flashes. It is hypothesized that the cell was producing a higher percentage of IC flashes as the electric field in the negative charge region increased. Unfortunately this proposed increase in the IC flash rate could not be confirmed from observations. Once the updraft had lost it vigor and the histogram started obtaining a diagonal characteristic, the cell again produced CG flashes. This time the flashes lowered positive charge to the ground. The flashes were, as previous studies have found, located in the downshear anvil region of the storm. The histograms reveal that very high reflectivities (> 55 dBZ) were still detectable in the high-levels of the cell, well-above the mixed-phase region. Therefore, it is assumed that the flash originated from positively-charged ice crystals located in the downshear anvil. Similar conclusions were made by Carey and Rutledge (1996b) in their investigation of a dominant positive CG lightning producing storm. If the negatively charged mixed-phase region began to lower during this period as the updraft subsided, the IC flash rate would have decreased leaving the dense

positive charge aloft the opportunity to discharge to ground. Why were not negative CG flashes preferred as the negative charge moved closer to the ground? Perhaps the charge density of the negative region was lowered below breakdown potential by the increased vertical extent of this charge as this mass precipitated. The environmental vertical wind shear usually necessary to sustain the dynamics of a severe thunderstorm should also be considered. Large quantities of positively charged ice crystals could be horizontally displaced upshear of the main reflectivity core giving the upper positive region further opportunity to discharge to ground.

The relationship between the mesocyclone and flash characteristics is not totally obvious in this case. One could assume that the strong updrafts required to create large reflectivities in the upper-levels of the storm would also be conducive to the formation of a mesocyclone as the updraft intensifies the low-level rotation of the storm inflow. Similarly, the cold outflow created as this large ice mass precipitates and evaporatively cools the low-levels could easily be responsible for the shear instabilities produced along the gust front which may have contributed to the formation of the gustnado.

Regardless of the specific mechanisms involved, it is clear that this cell was strikingly different from the rest of the cells in its motion, intensity, development, and electrification. Lightning and radar observations could give forecasters a reason to be suspicious of a particular thunderstorm and generate closer scrutiny. To better investigate a similar scenario, one would need a three-dimensional lightning detection system along with high spatial and temporal resolution polarimetric dual-Doppler observations.

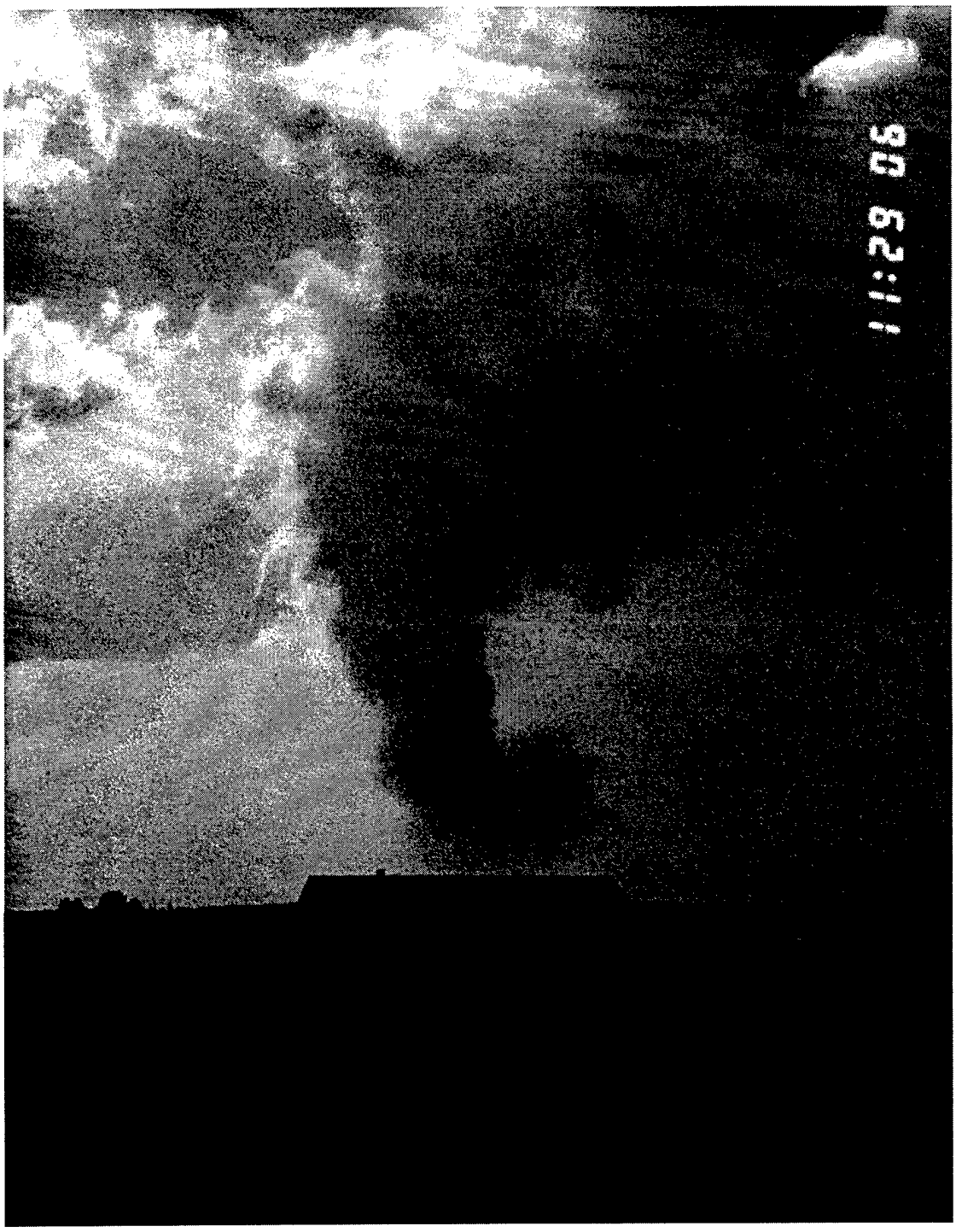

Fig. 4.1 Image of gustnado from 35mm transparency taken by NCAR chase team near Gilcrest, Colorado, on 23 July 1993. View is to the west. Actual GPS time was 23:30:37 UTC.

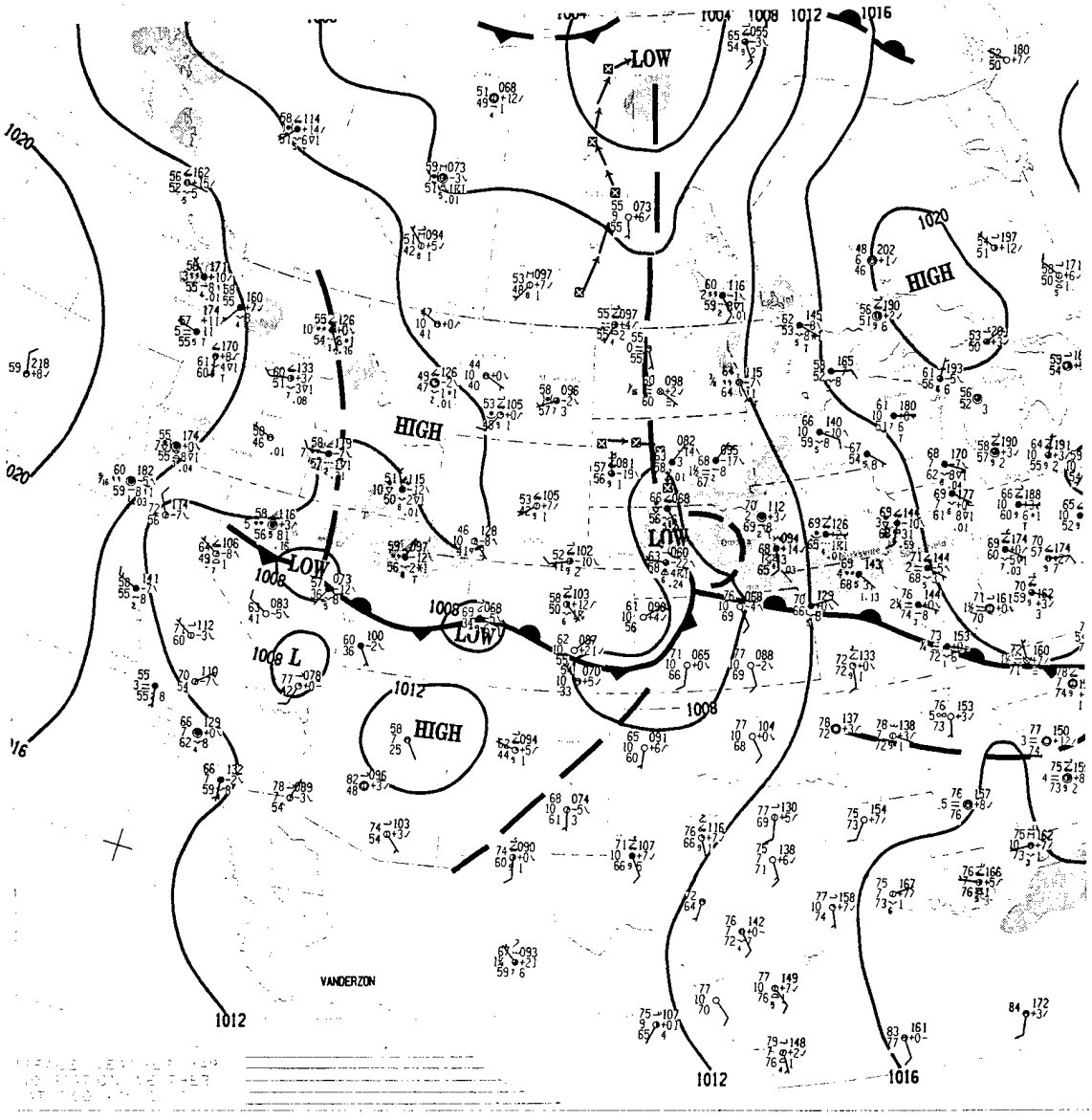

Fig. 4.2 Surface weather chart with frontal analysis of western United States on 23 July 1993 at 1200 UTC. Areas of precipitation are indicated by shading.

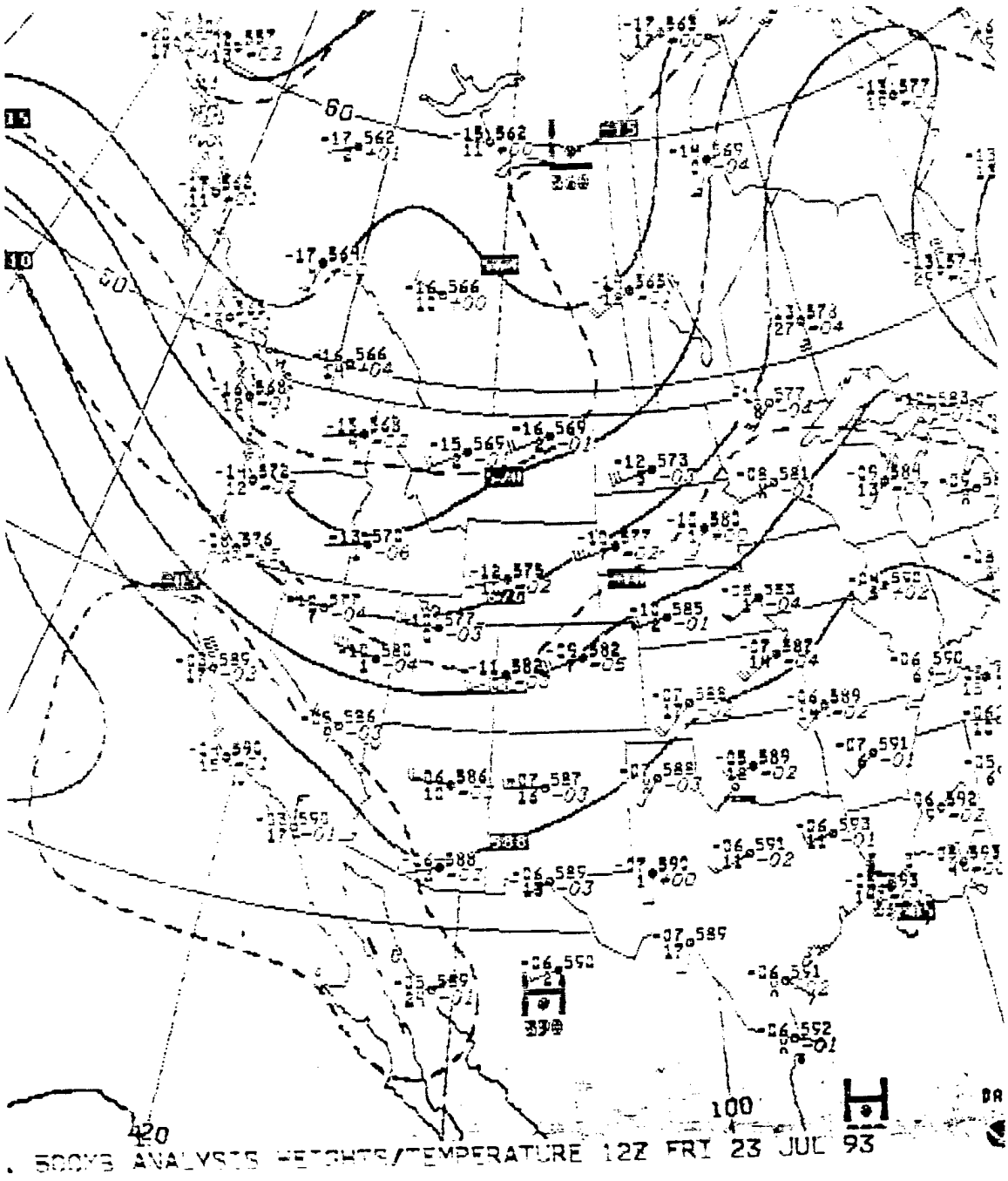

Fig. 4.3 500 mb height analysis of western United States on 23 July 1993 at 1200 UTC.

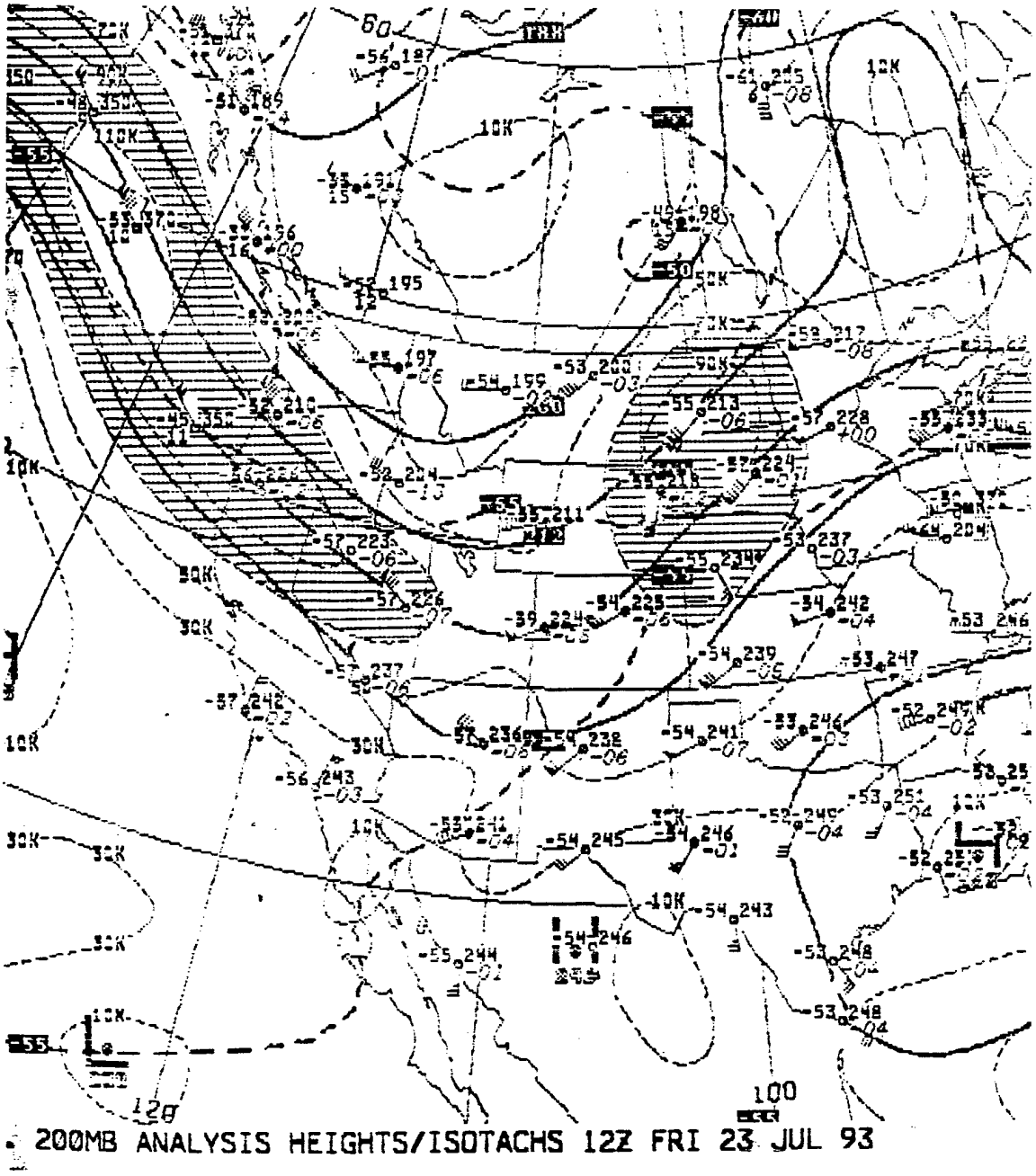

Fig. 4.4 200 mb height analysis of western United States on 23 July 1993 at 1200 UTC.

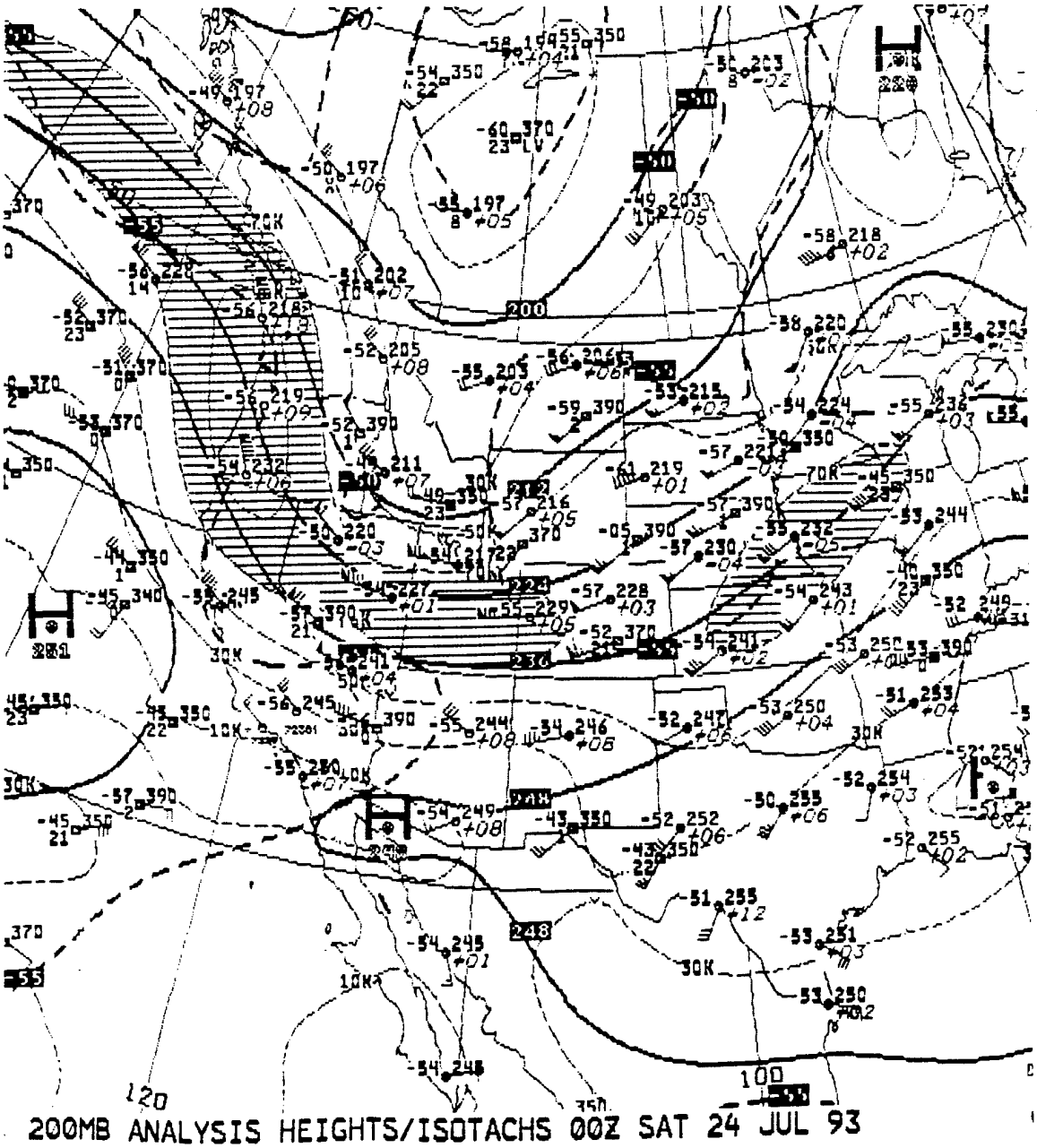

Fig. 4.5 As in Fig. 4.4 except on 24 July 1993 at 0000 UTC.

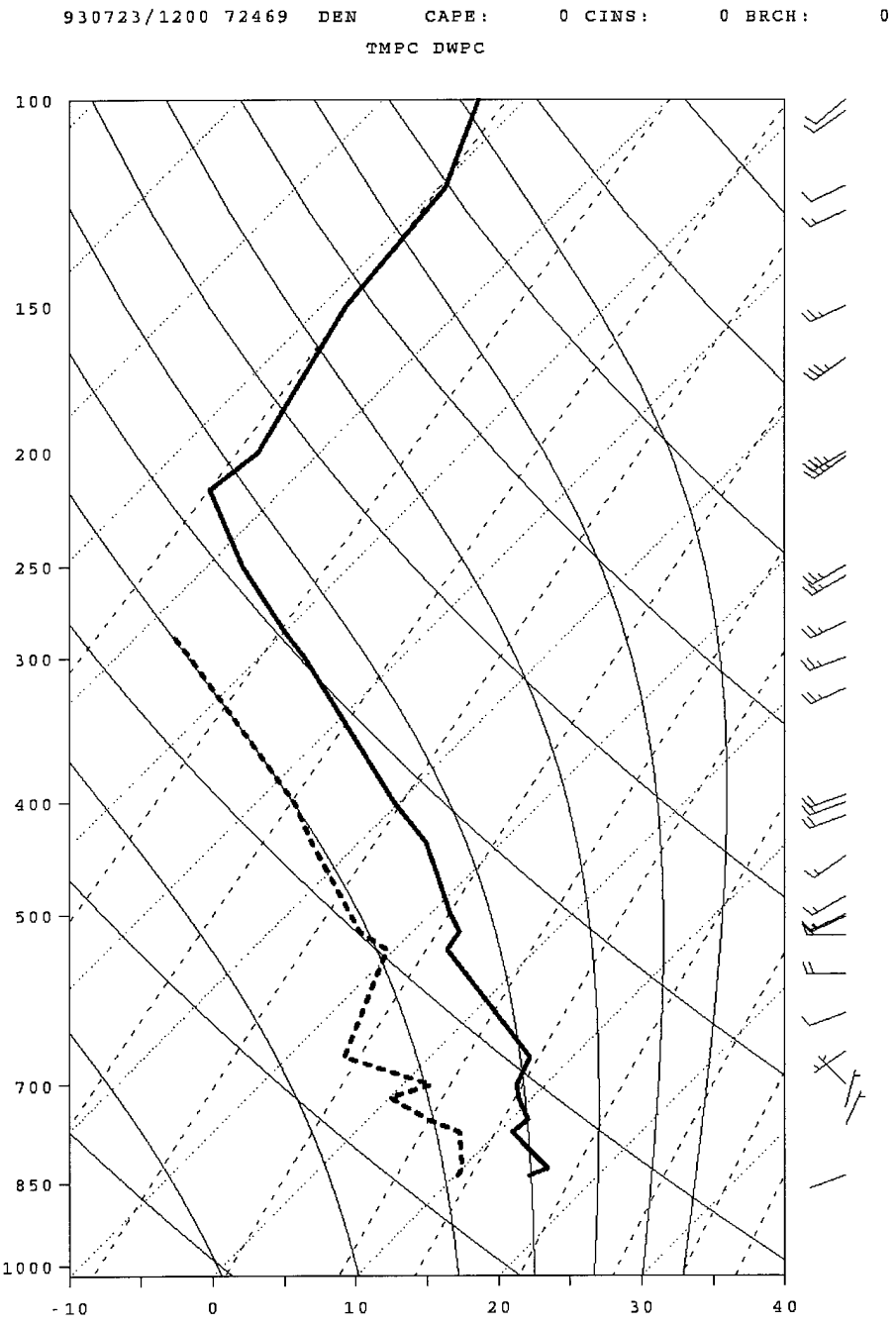

Fig. 4.6 Skew T - Log P plot of upper air sounding for Denver (DEN), Colorado, on 23 July 1993 at 1200 UTC. Profile of temperature (solid line) and dewpoint (dashed line) is given in °C. Winds are in m s^{-1}.

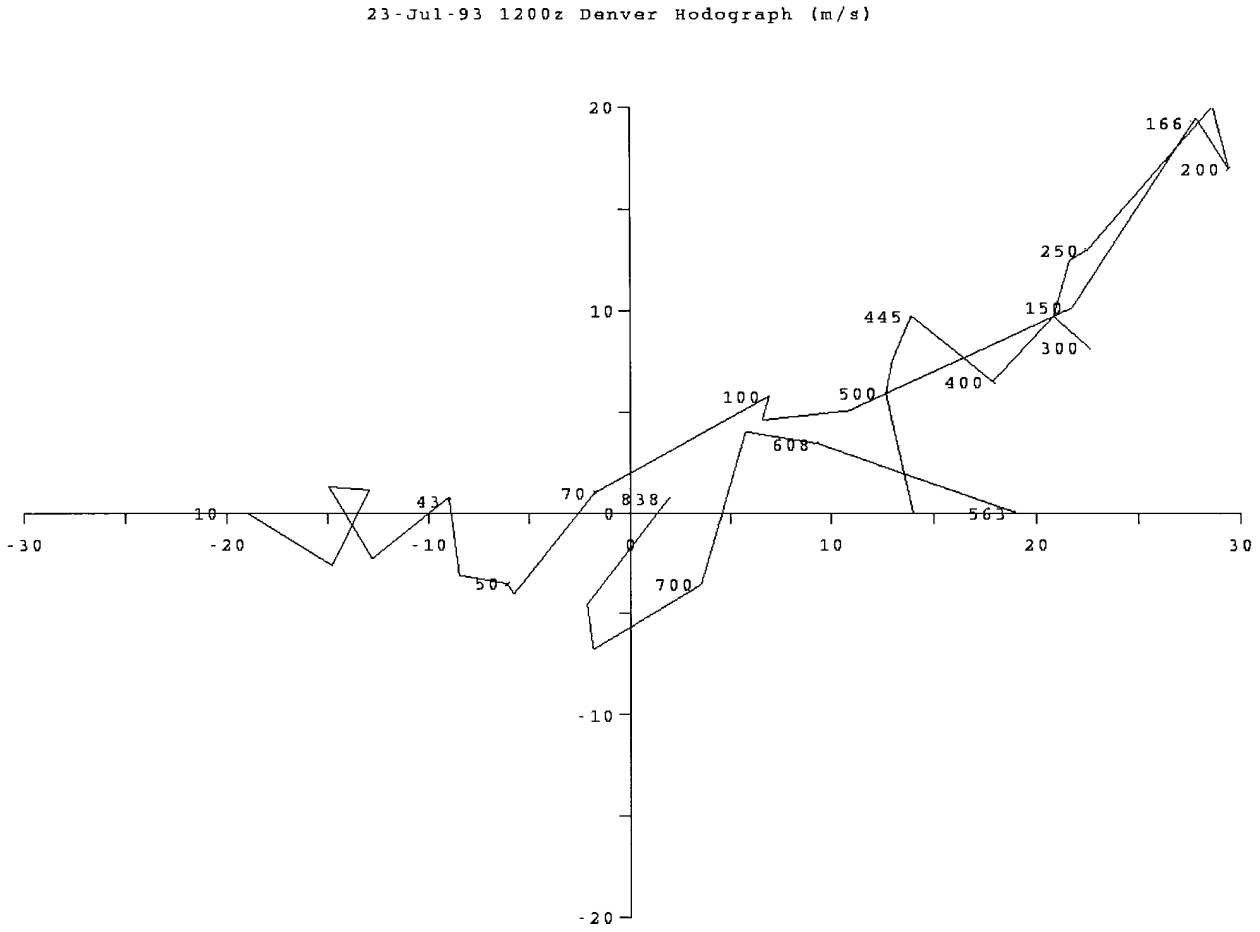

Fig. 4.7 Hodograph of Denver 1200 UTC sounding on 23 July 1993. Pressure at selected points is given in mb. Units are in m s^{-1}.

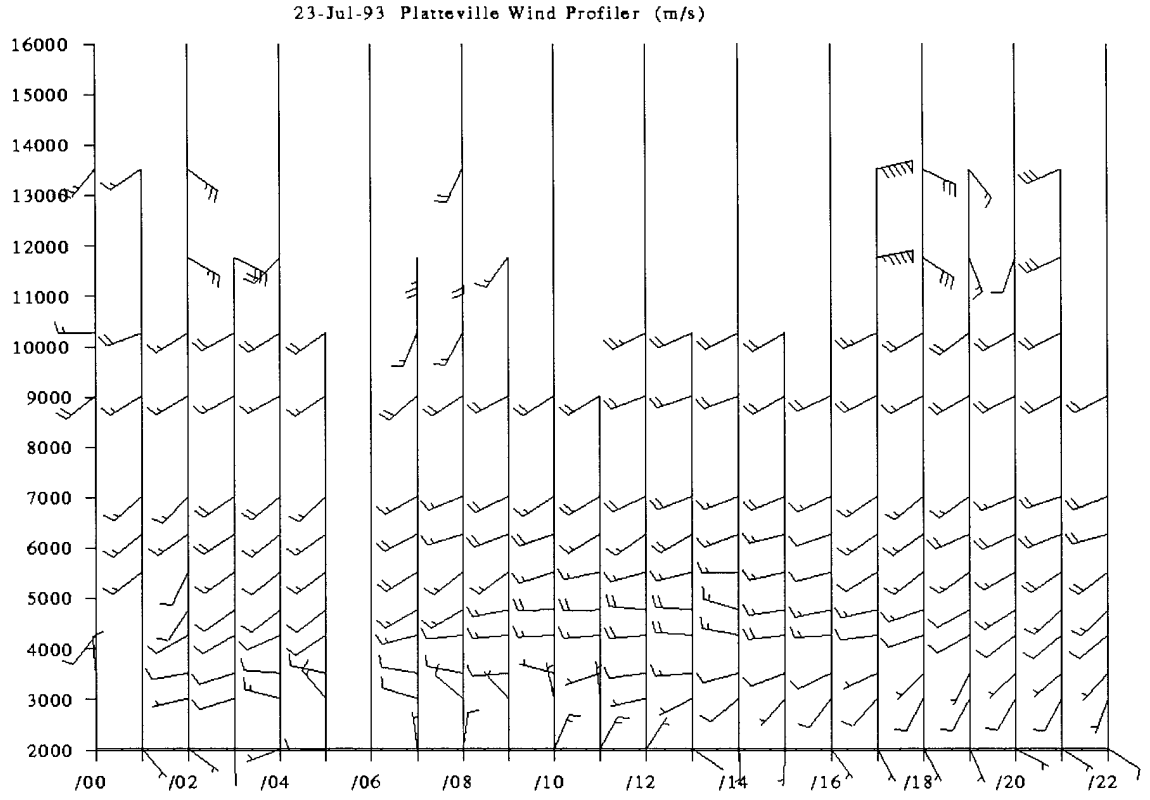

Fig. 4.8 Platteville, Colorado wind profiler horizontal winds on 23 July 1993 from 0000 to 2200 UTC.

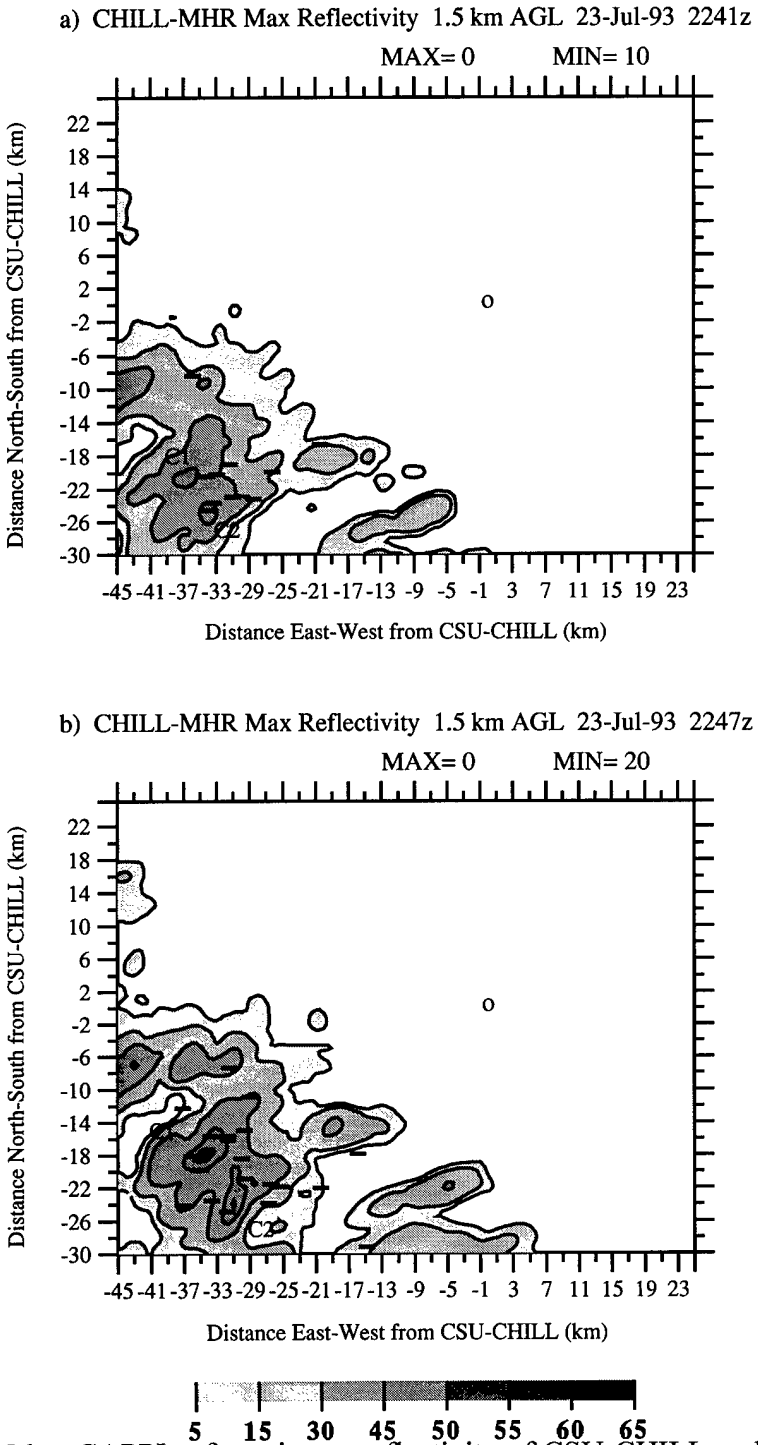

Fig. 4.9 1.5 km CAPPIs of maximum reflectivity of CSU-CHILL and MHR. CG flash locations with polarity are shown. MAX and MIN values correspond to the number of positive and negative flashes respectively. Cell numbers are shown next to their respective cells. (a) 2241 UTC, (b) 2247 UTC.

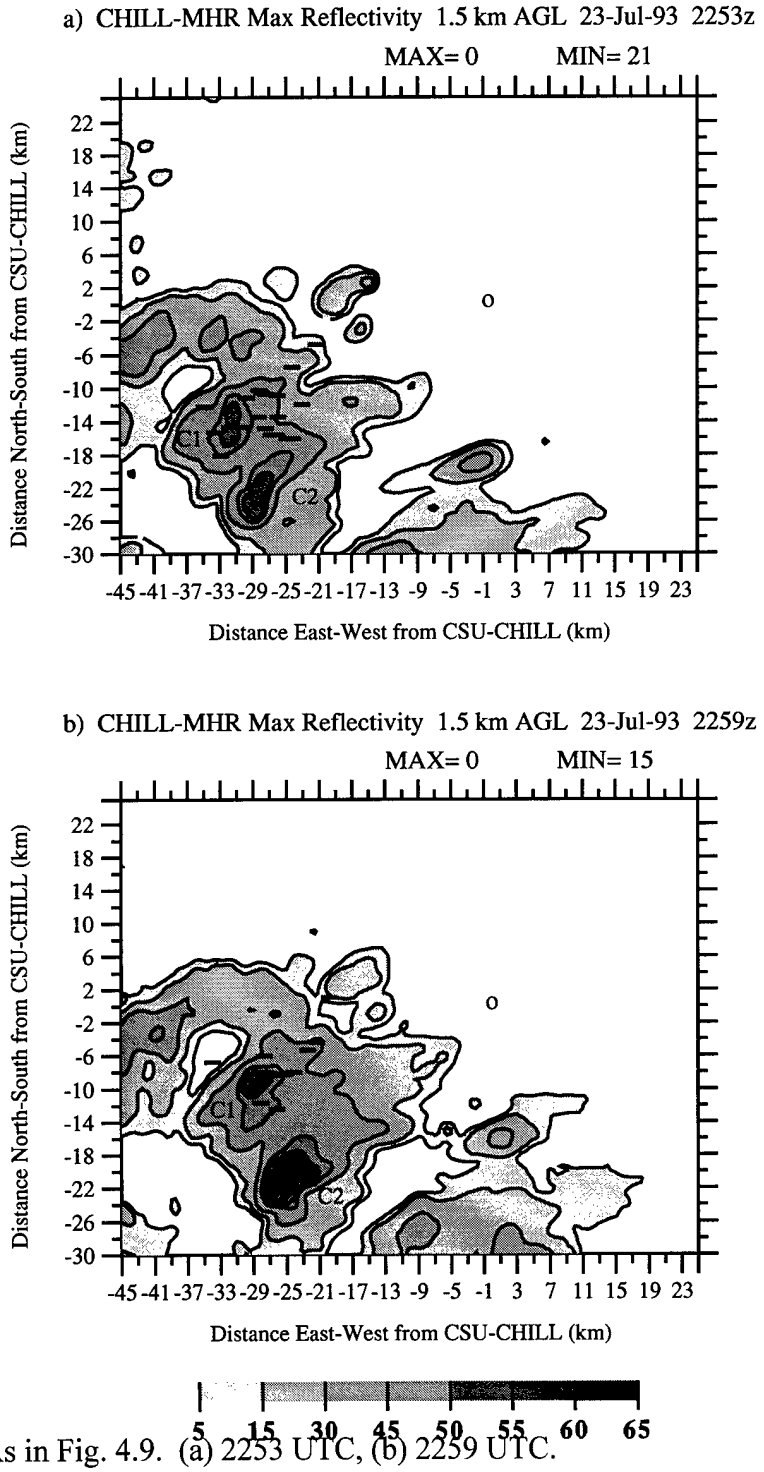

Fig. 4.10 As in Fig. 4.9. (a) 2253 UTC, (b) 2259 UTC.

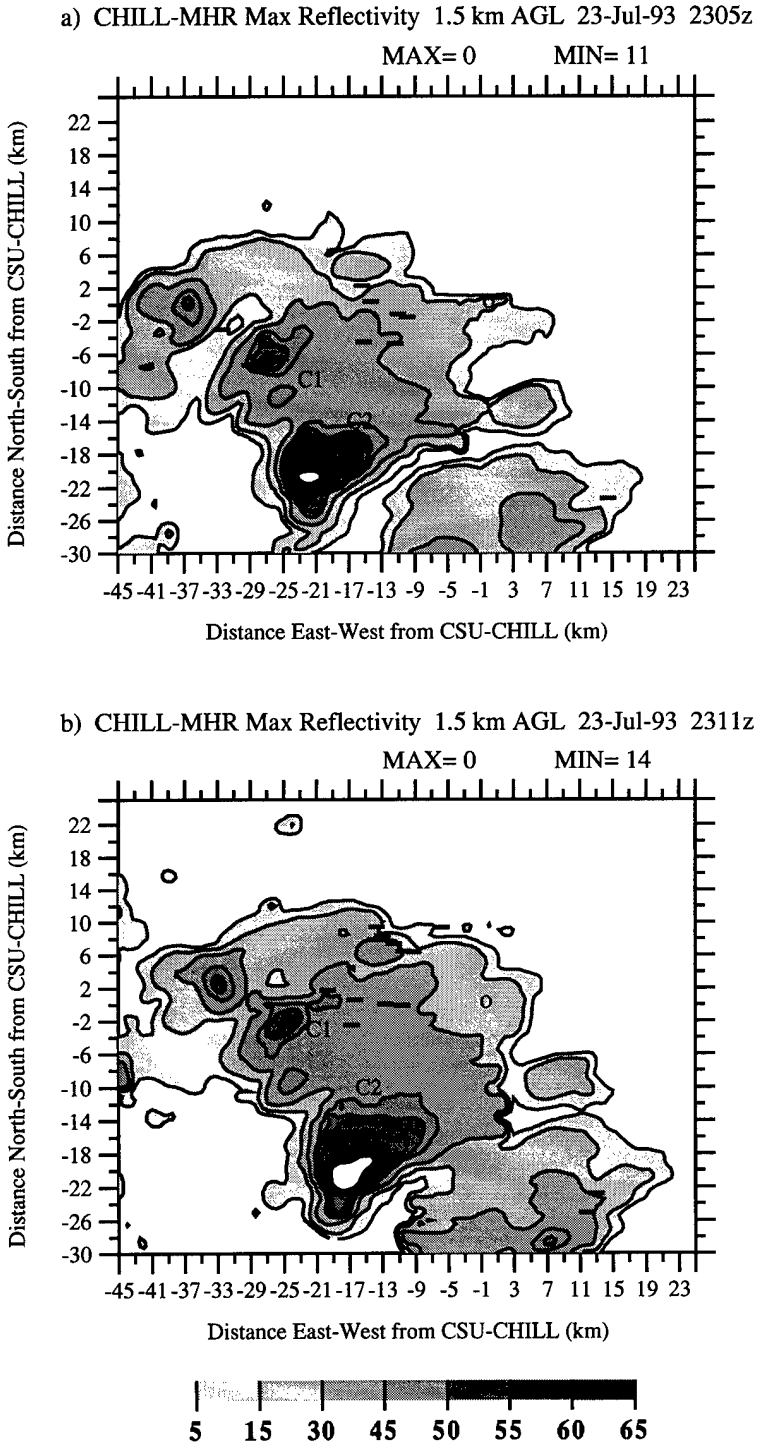

Fig. 4.11 As in Fig. 4.9. (a) 2305 UTC, (b) 2311 UTC.

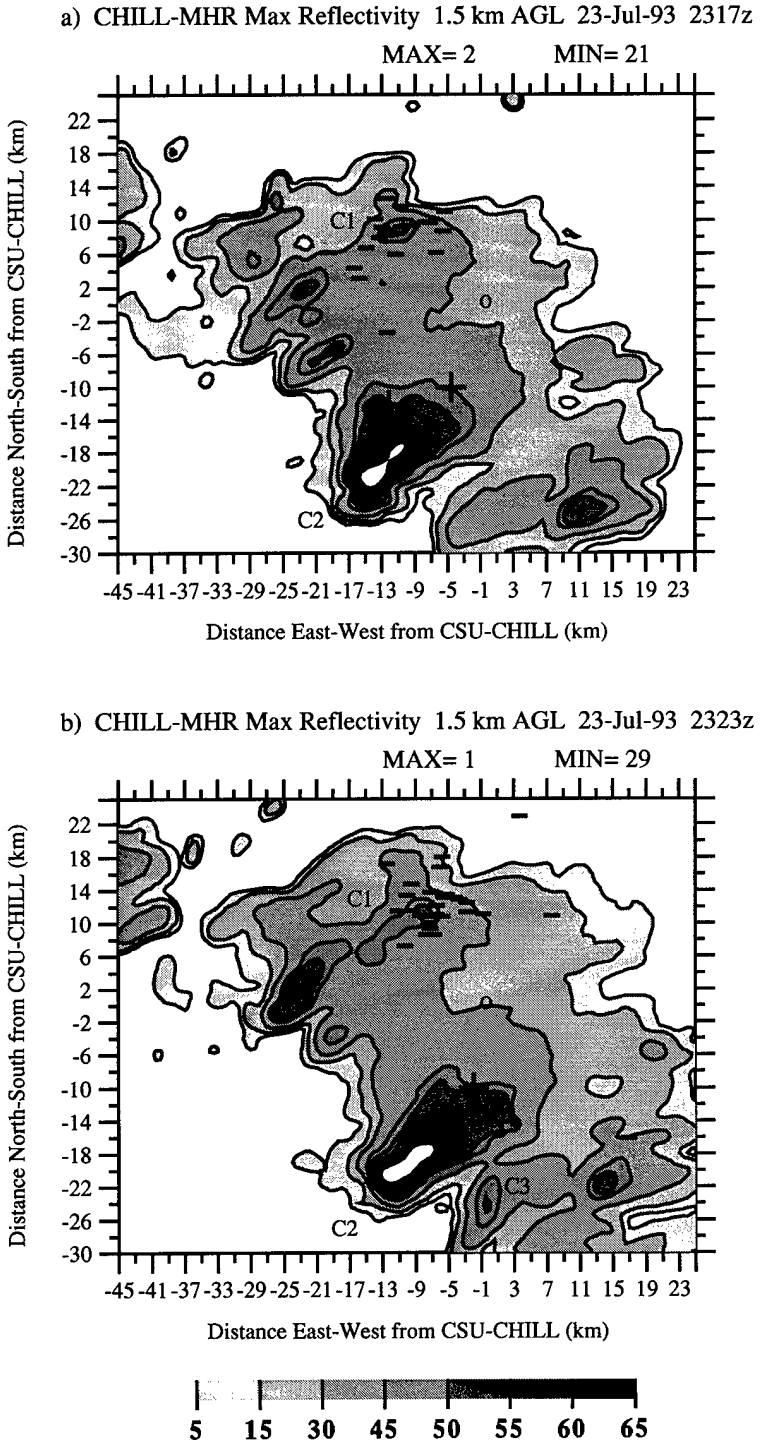

Fig. 4.12 As in Fig. 4.9. (a) 2317 UTC, (b) 2323 UTC.

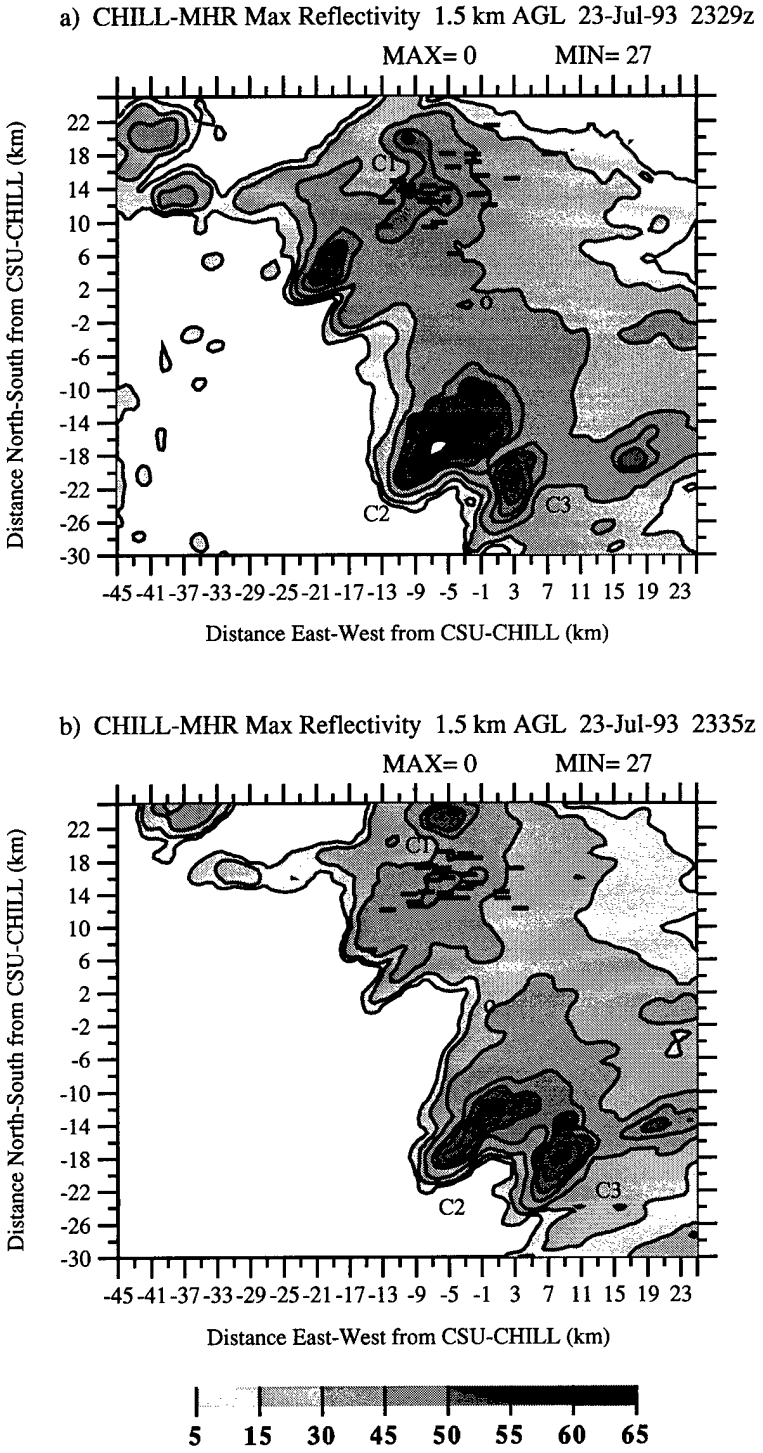

Fig. 4.13 As in Fig. 4.9. (a) 2329 UTC, (b) 2335 UTC.

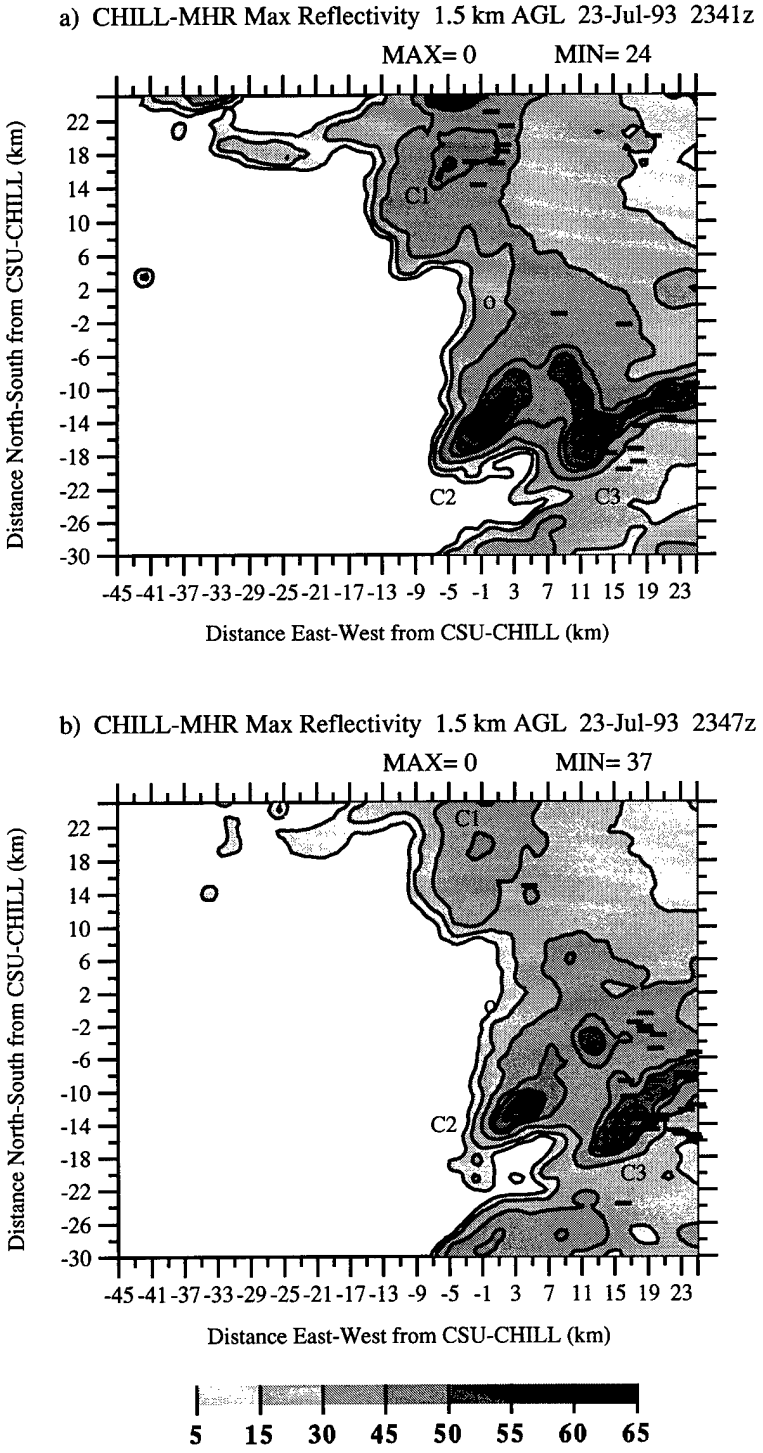

Fig. 4.14 As in Fig. 4.9. (a) 2341 UTC, (b) 2347 UTC.

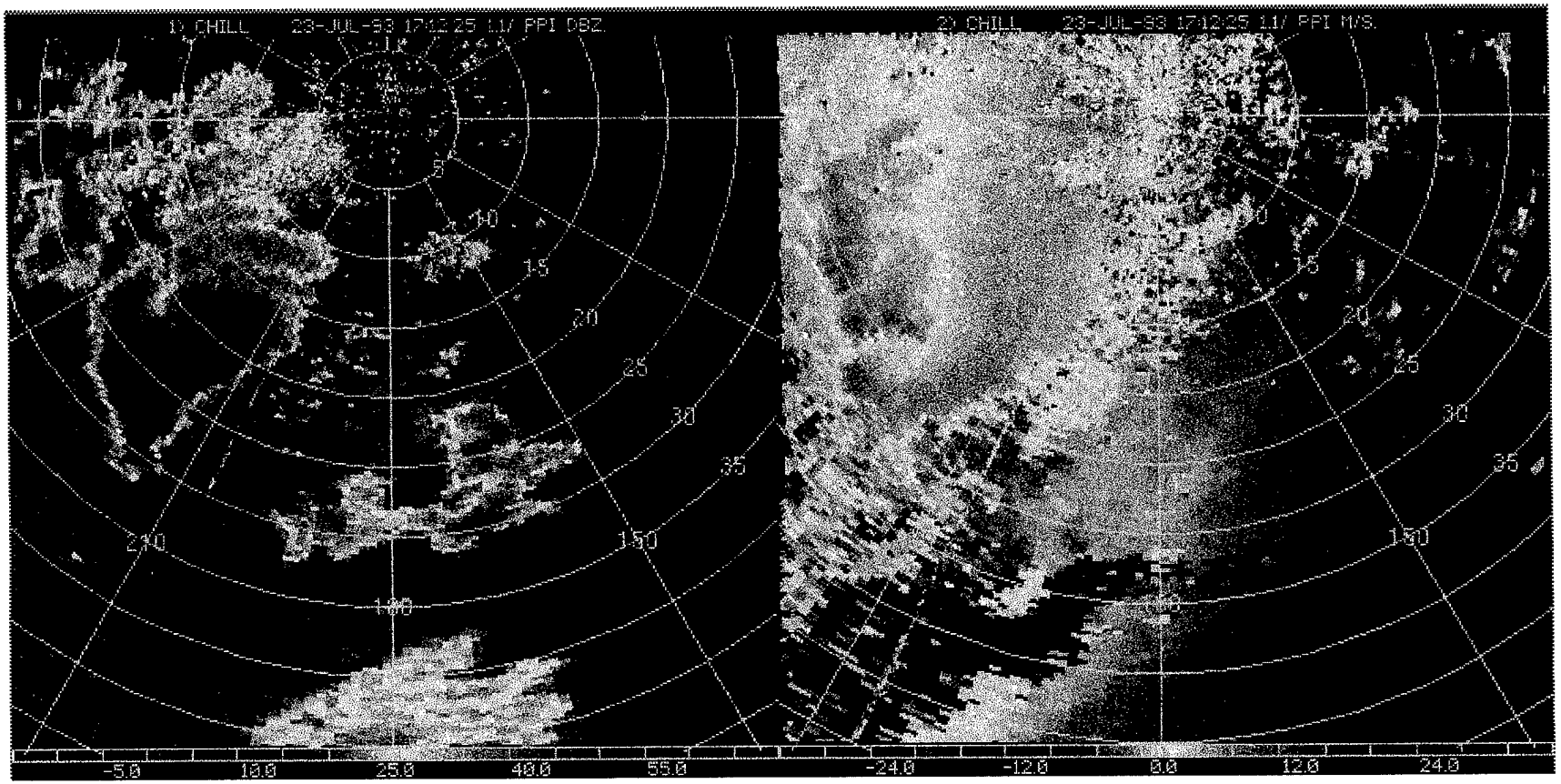

Fig. 4.15 Elevation scan of 1.1° from the CSU-CHILL radar on 23 July 1993 at 1712 MDT (2312 UTC). Left: reflectivity. Right: radial velocity. The color scale for the magnitudes is shown at the bottom. Standard convention is used for radial velocity where negative values (cool tones) indicate motion toward the radar and positive values (warm tones) indicate motion away. Range rings are every 5 km.

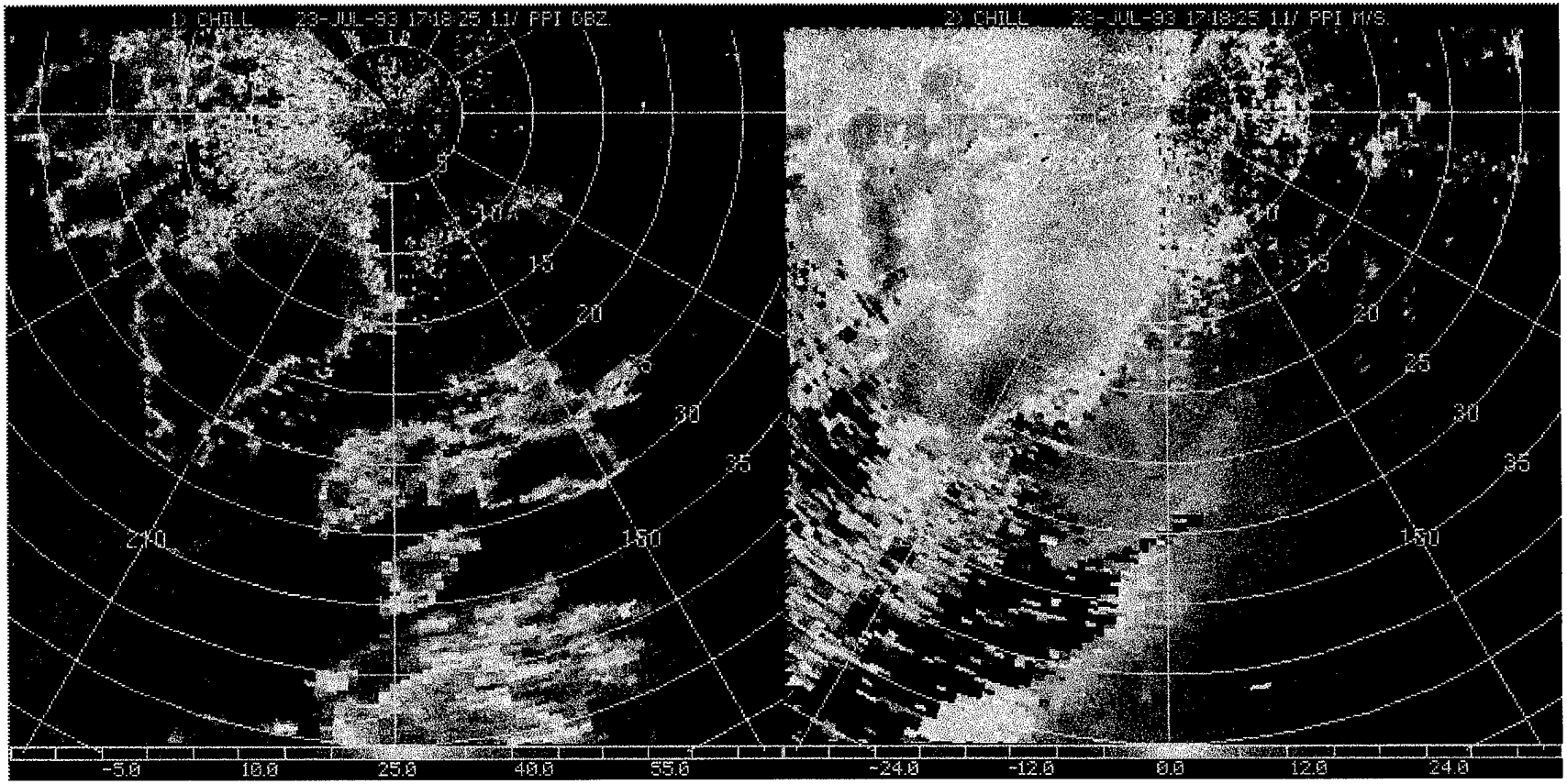

Fig. 4.16 As in Fig. 4.15 except at 1718 MDT (2318 UTC).

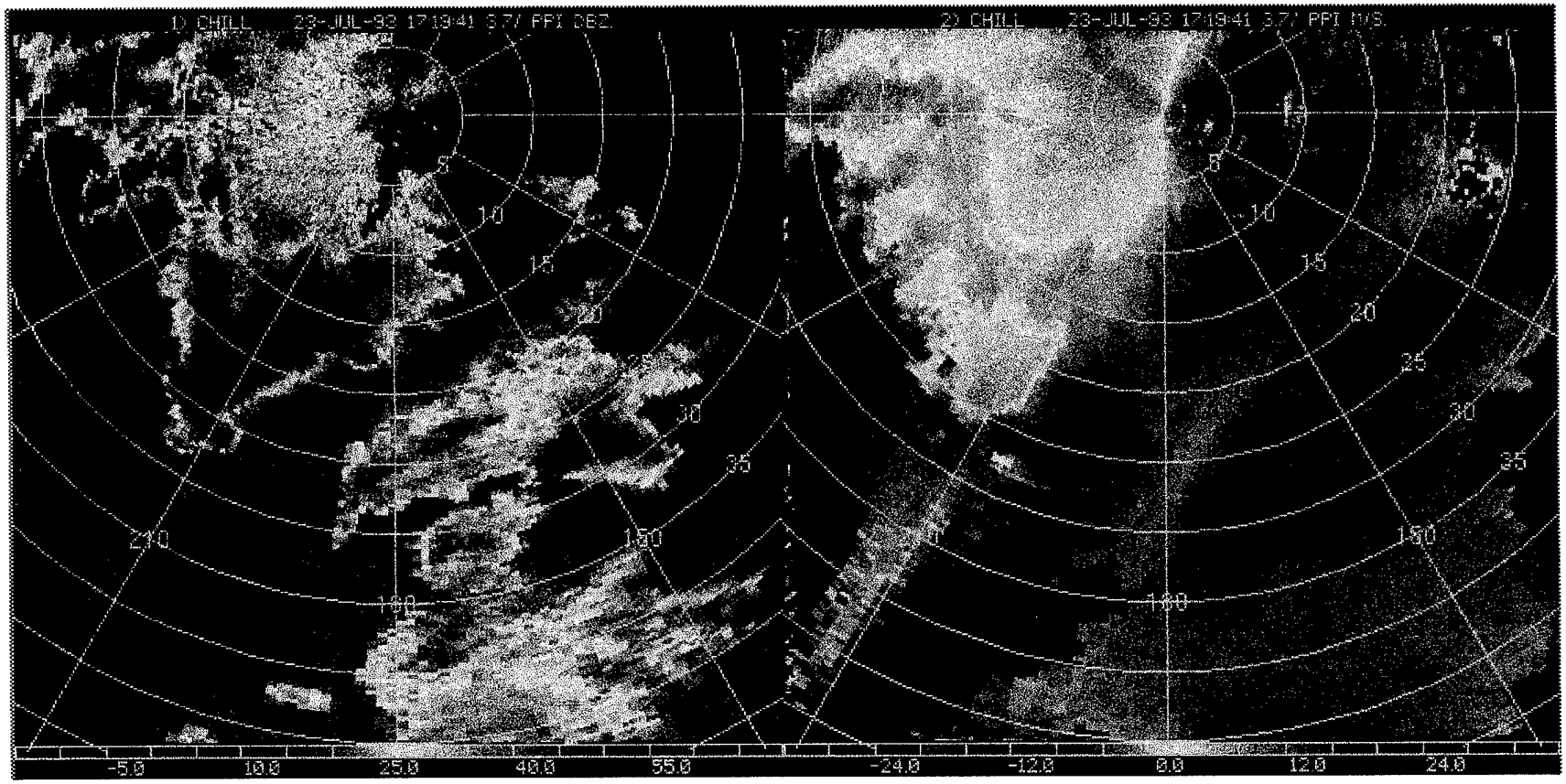

Fig. 4.17 As in Fig. 4.15 except for an elevation scan of 3.7° at 1719 MDT (2319 UTC).

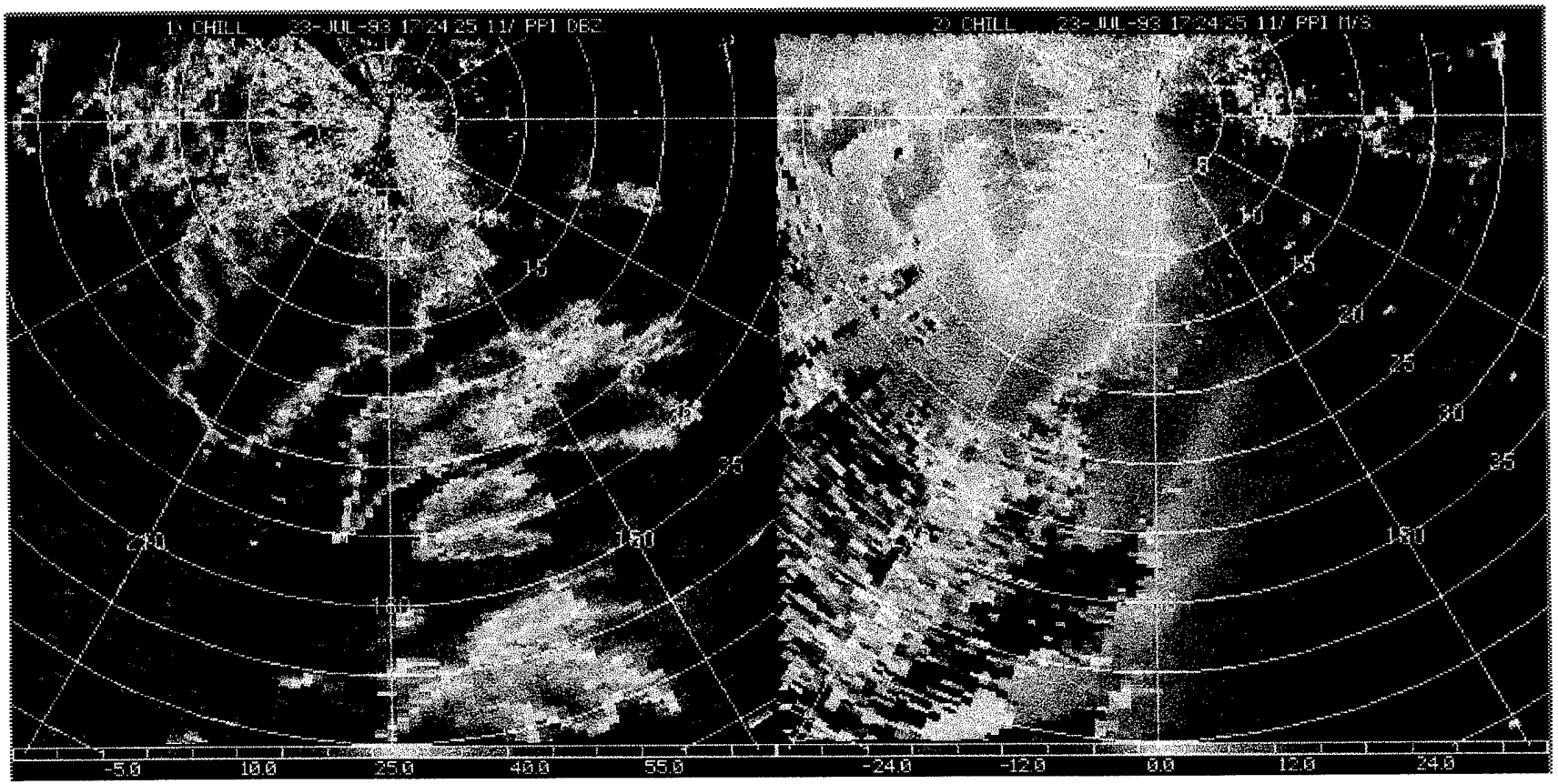

Fig. 4.18 As in Fig. 4.15 except for an elevation scan of 1.1° at 1724 MDT (2324 UTC).

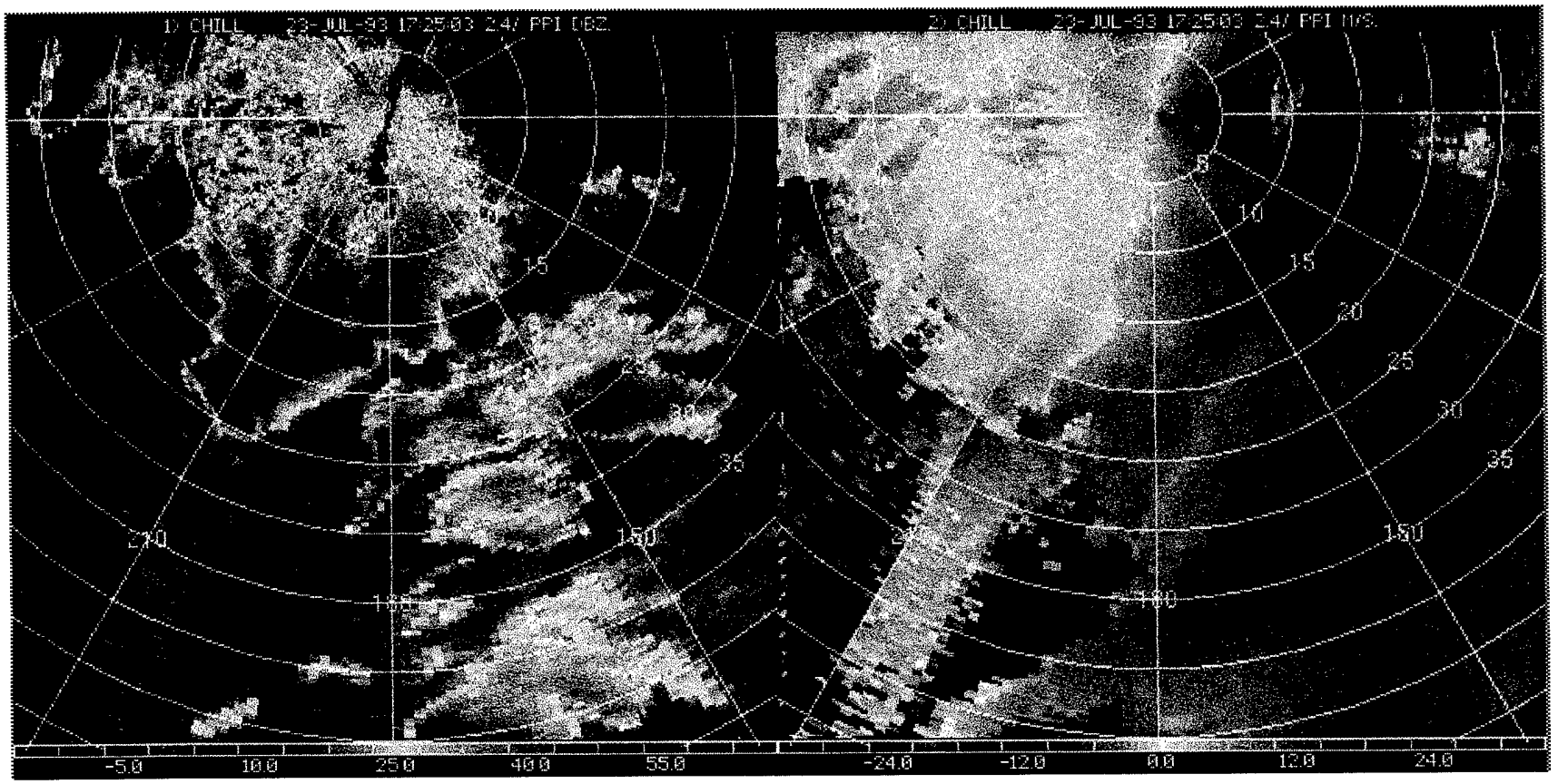

Fig. 4.19 As in Fig. 4.15 except for an elevation scan of 2.4° at 1725 MDT (2325 UTC).

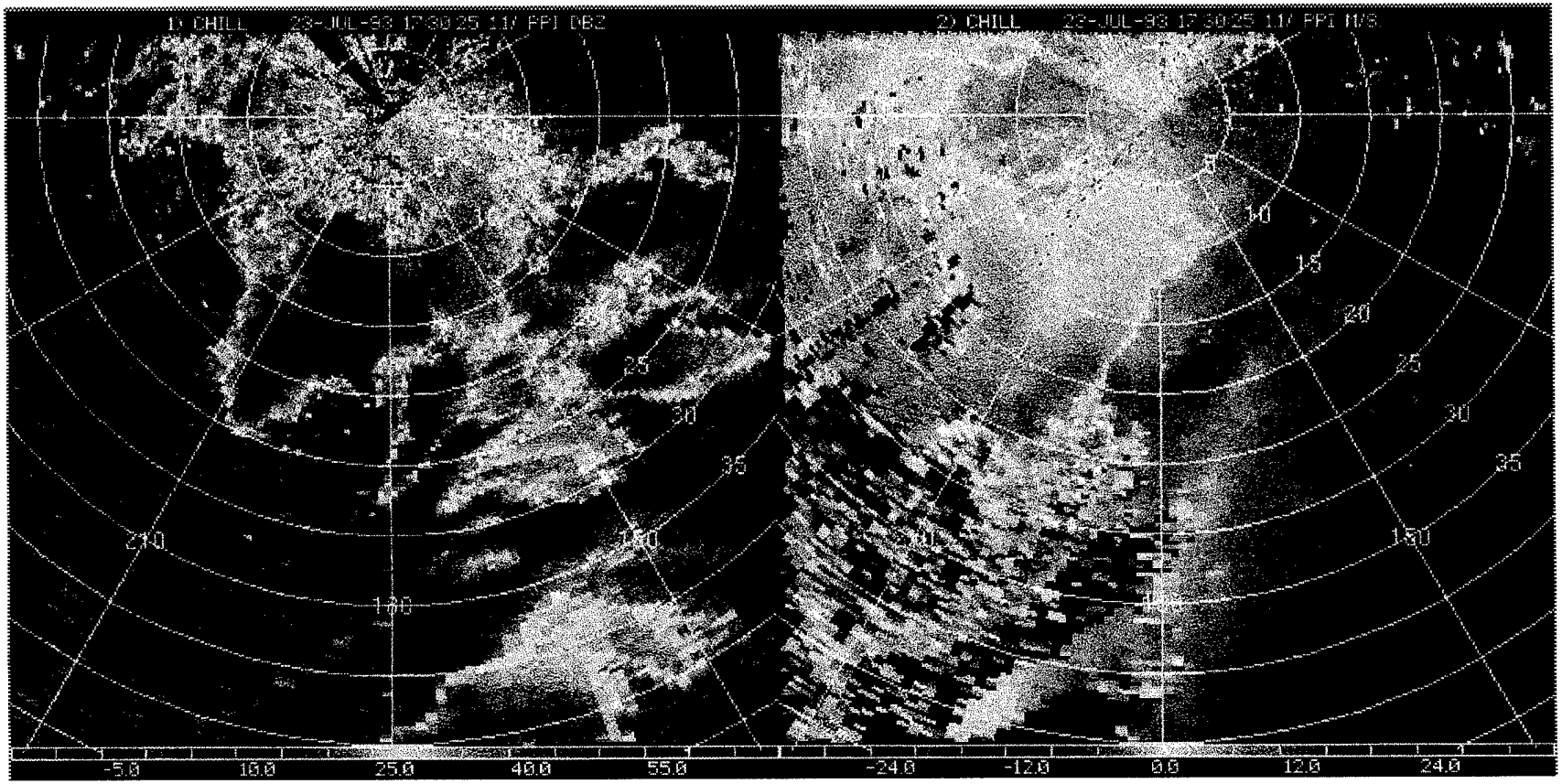

Fig. 4.20 As in Fig. 4.15 except for an elevation scan of 1.1° at 1730 MDT (2330 UTC).

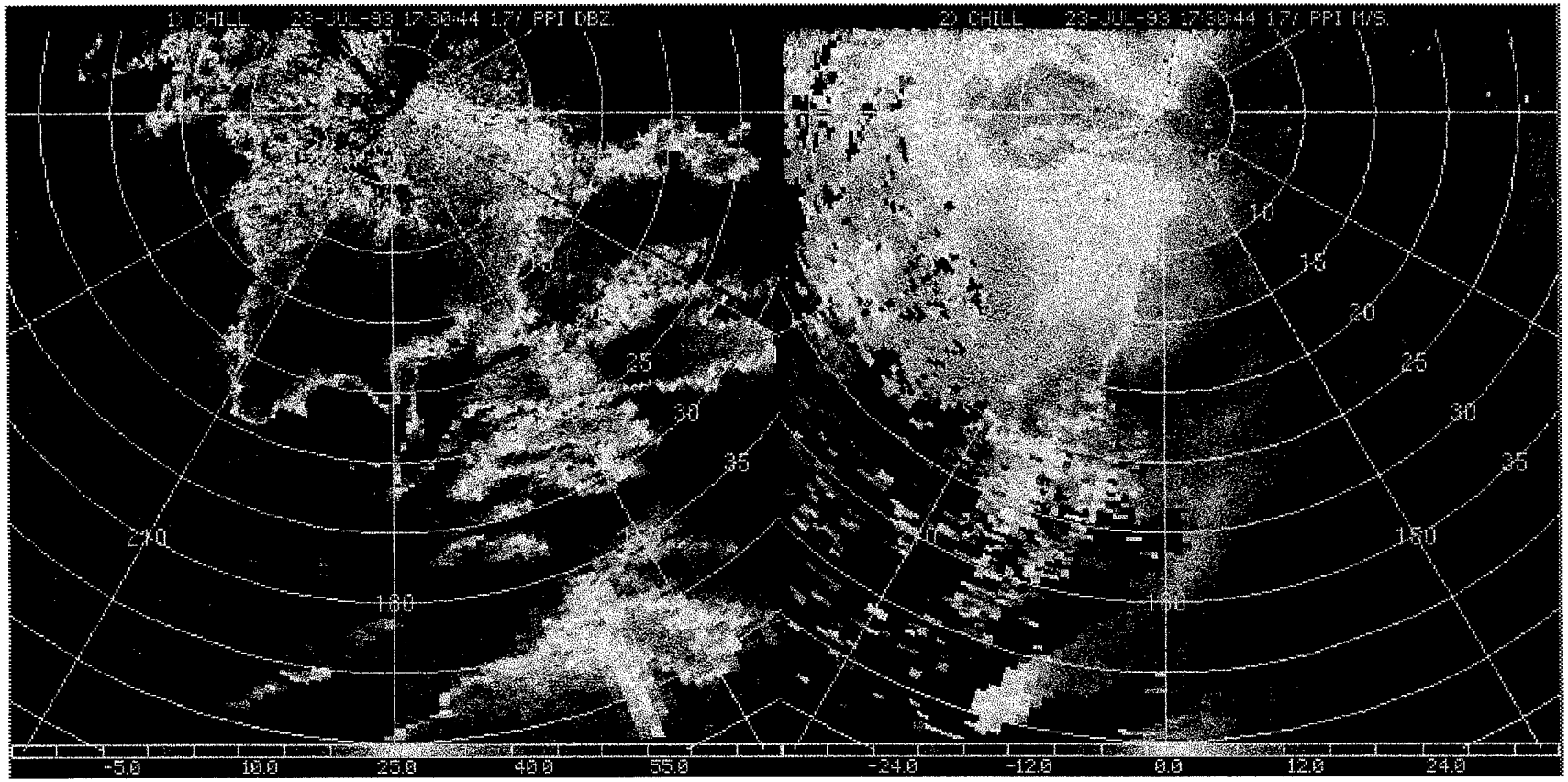

Fig. 4.21 As in Fig. 4.15 except for an elevation scan of 1.7° at 1730 MDT (2330 UTC).

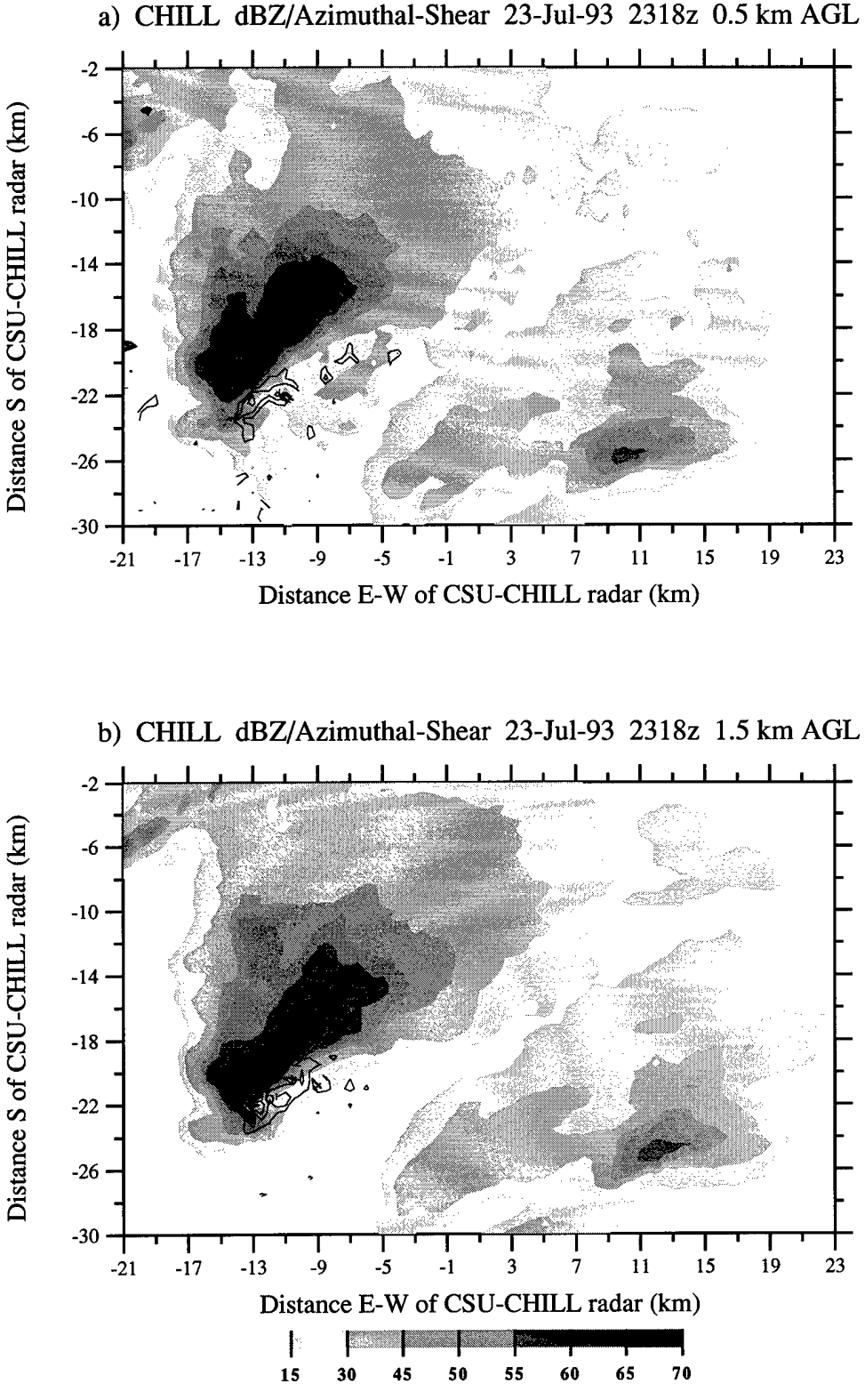

Fig. 4.22 2318 UTC CAPPIs of CSU-CHILL reflectivity (shaded) and azimuthal shear (solid contours). Azimuthal shear is contoured every 2 x 10^{-3} s^{-1} starting at 4 x 10^{-3} s^{-1}. (a) 0.5 km AGL, (b) 1.5 km AGL.

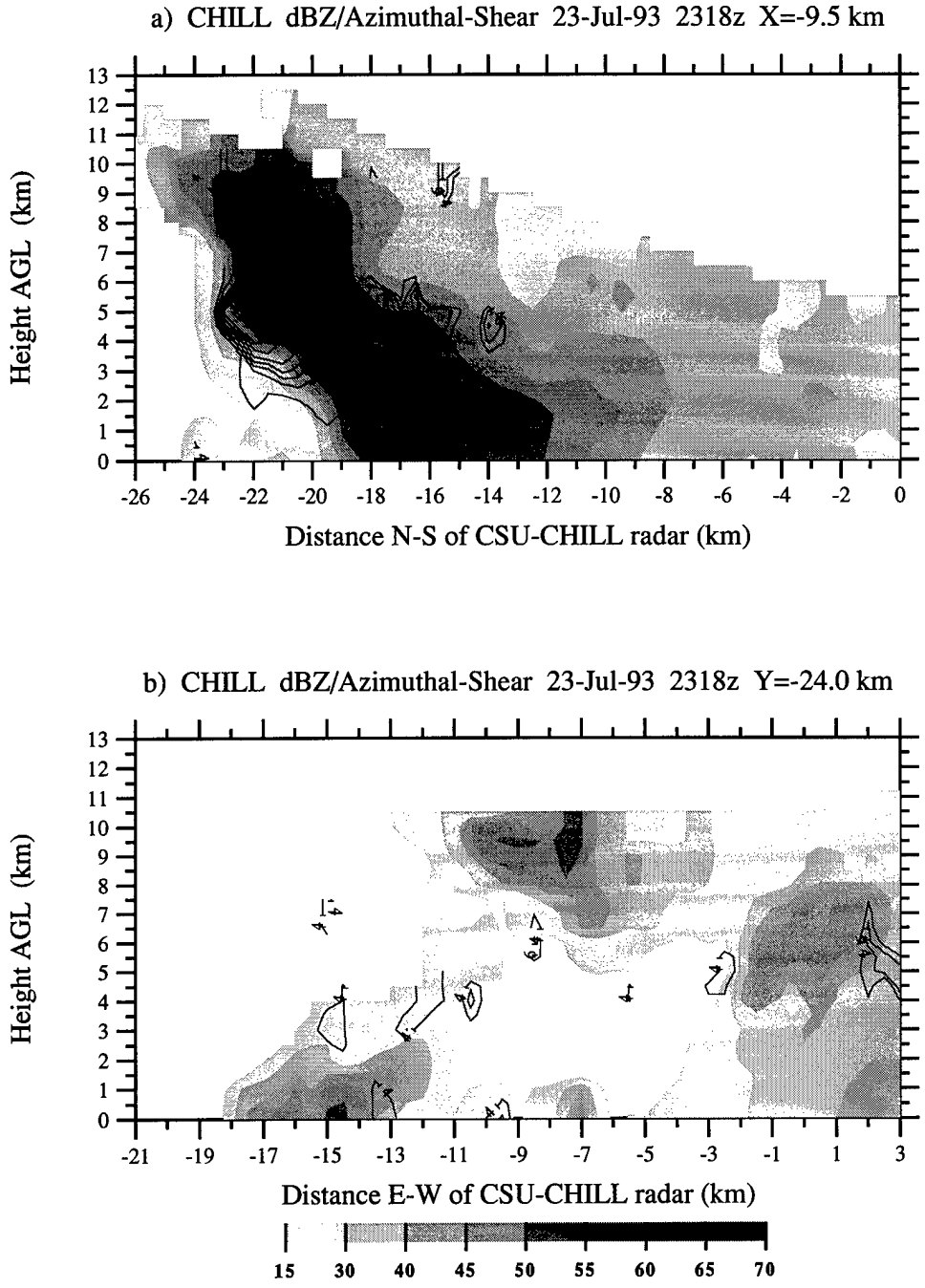

Fig. 4.23 As in Fig. 4.22 except 2318 UTC vertical cross-sections. (a) X= -9.5 km, (b) Y= -24.0 km.

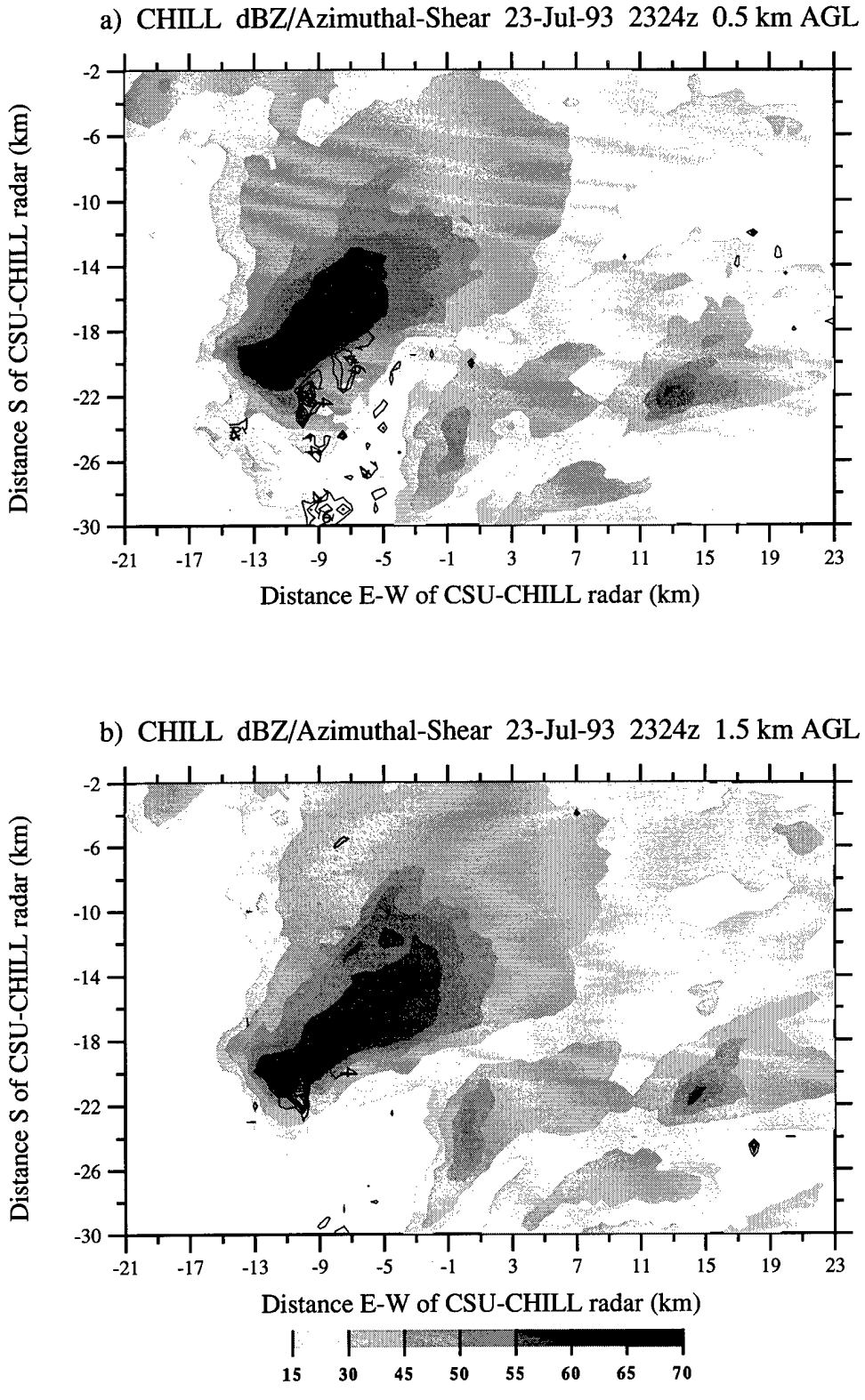

Fig. 4.24 As in Fig. 4.22 except 2324 UTC CAPPIs. (a) 0.5 km AGL, (b) 1.5 km AGL.

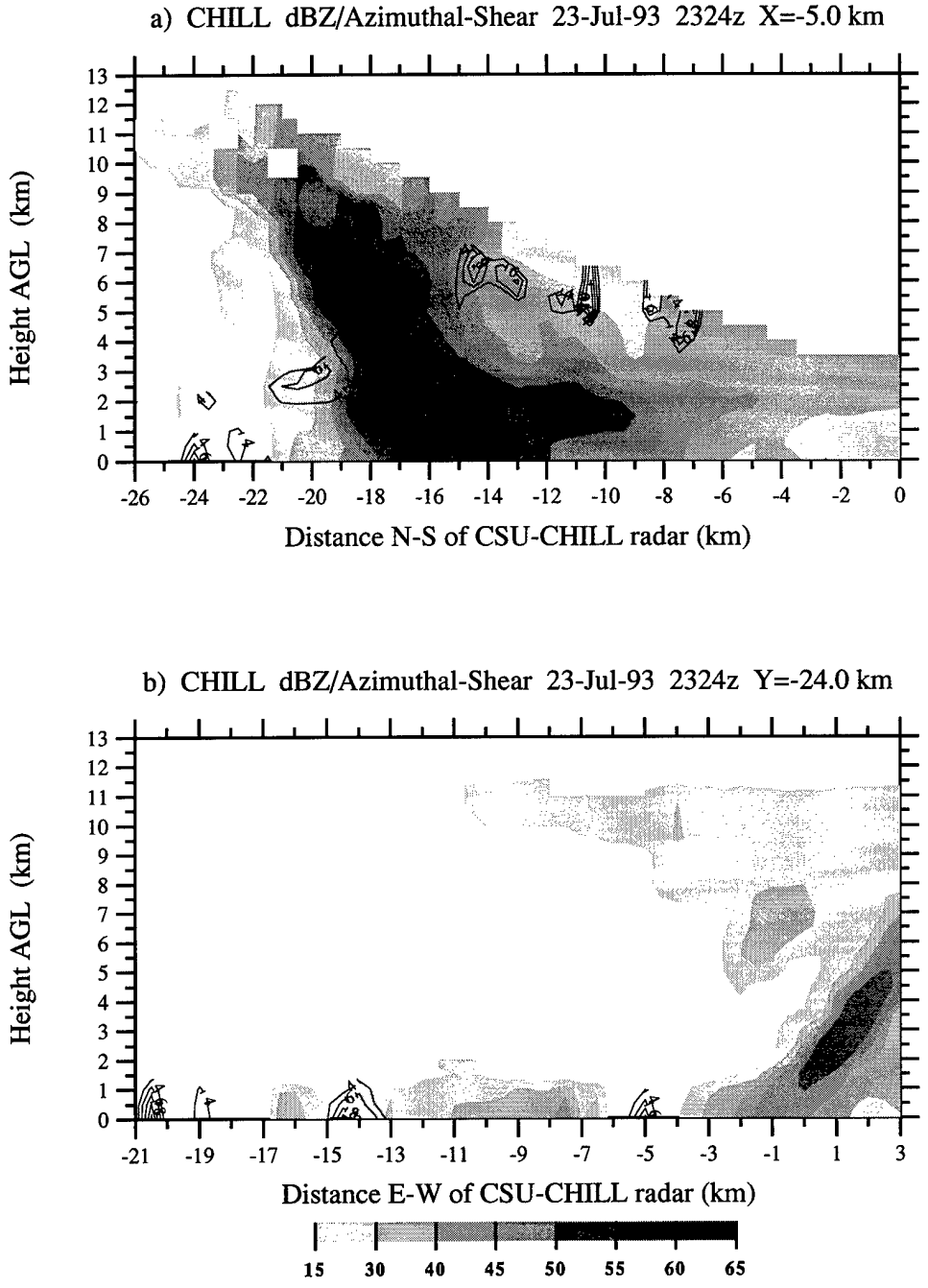

Fig. 4.25 As in Fig. 4.22 except 2324 UTC vertical cross-sections. (a) X= -5.0 km, (b) Y= -24.0 km.

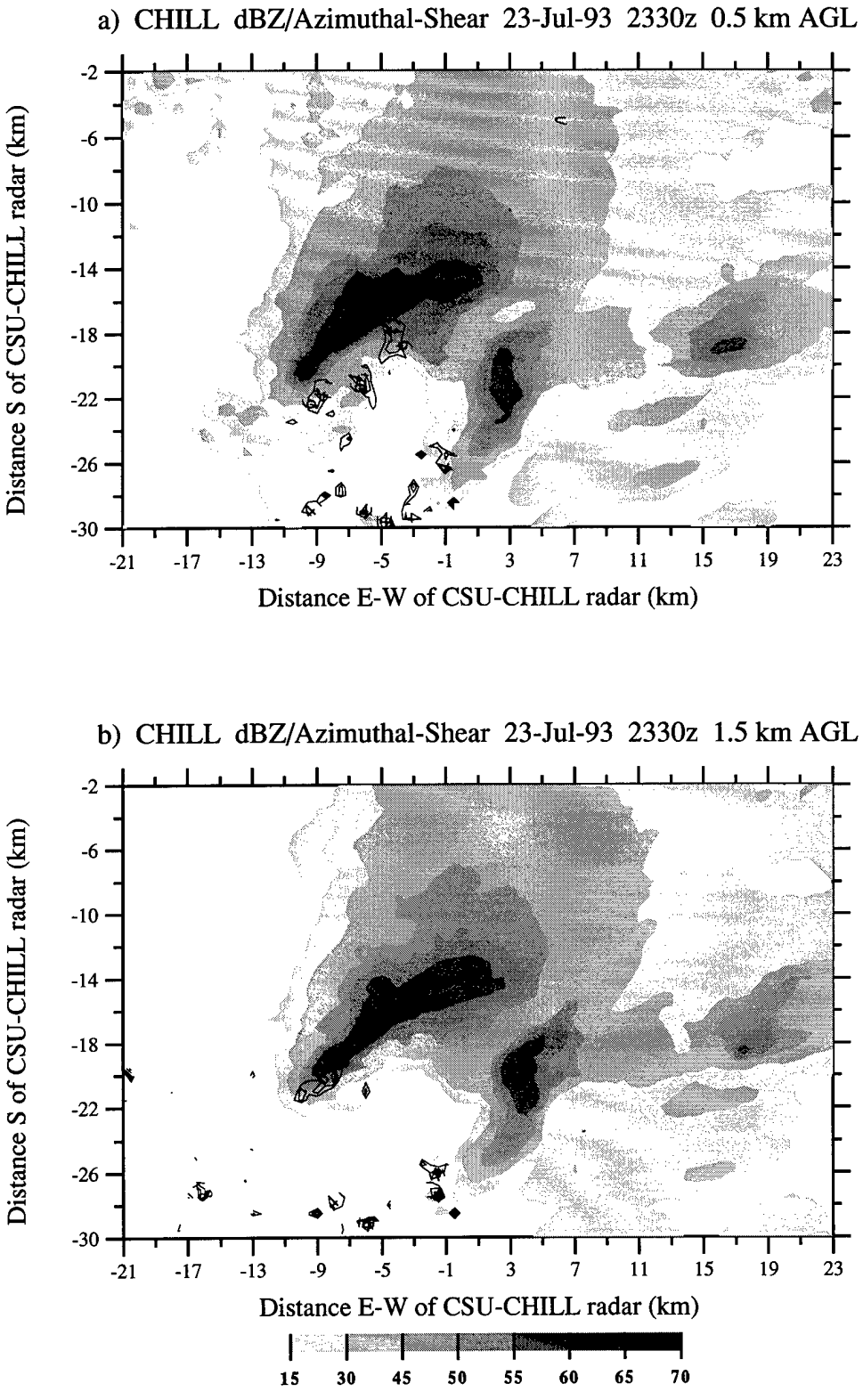

Fig. 4.26 As in Fig. 4.22 except 2330 UTC CAPPIs. (a) 0.5 km AGL, (b) 1.5 km AGL.

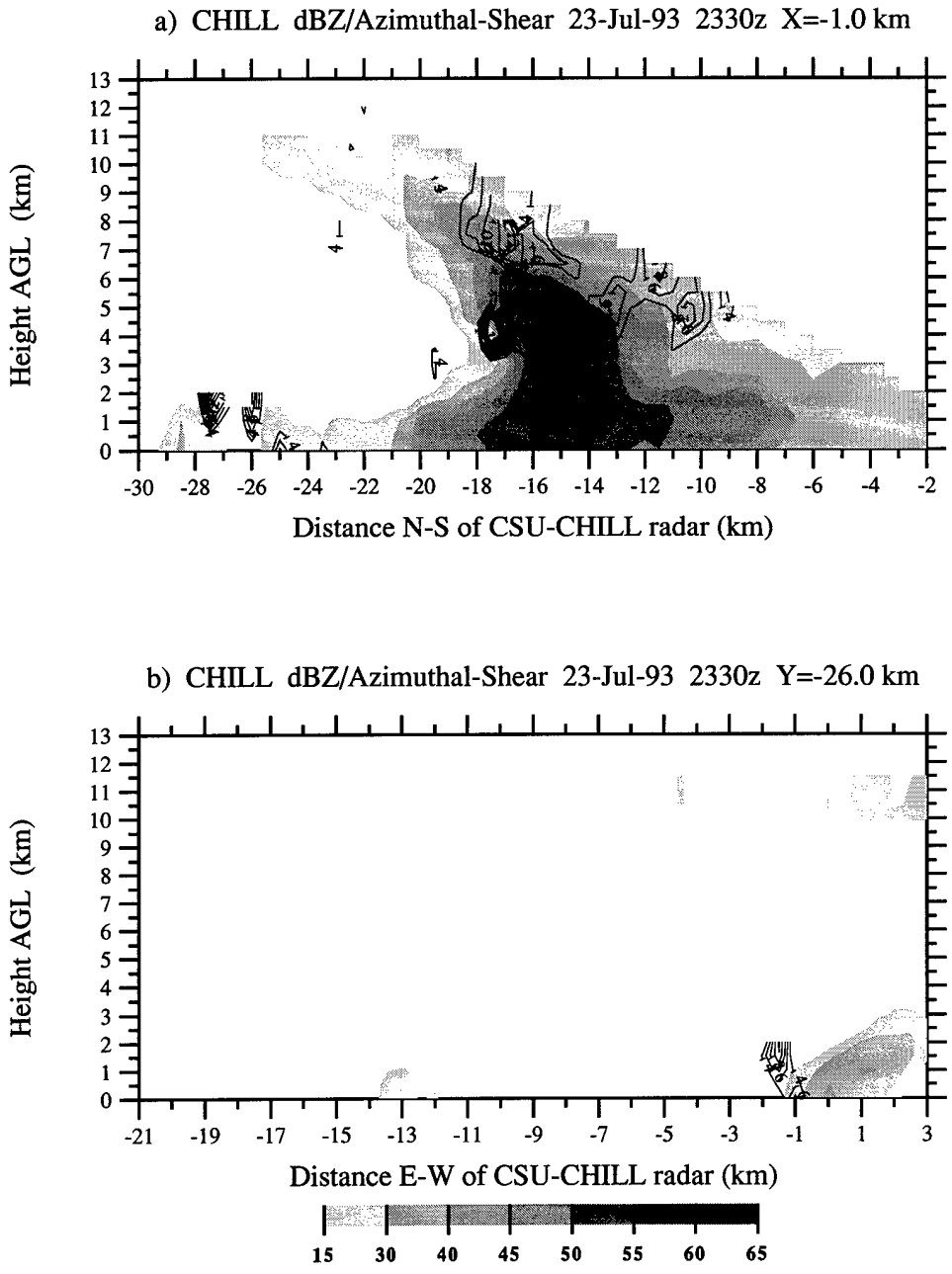

Fig. 4.27 As in Fig. 4.22 except 2330 UTC vertical cross-sections. (a) X= -1.0 km, (b) Y= -26.0 km.

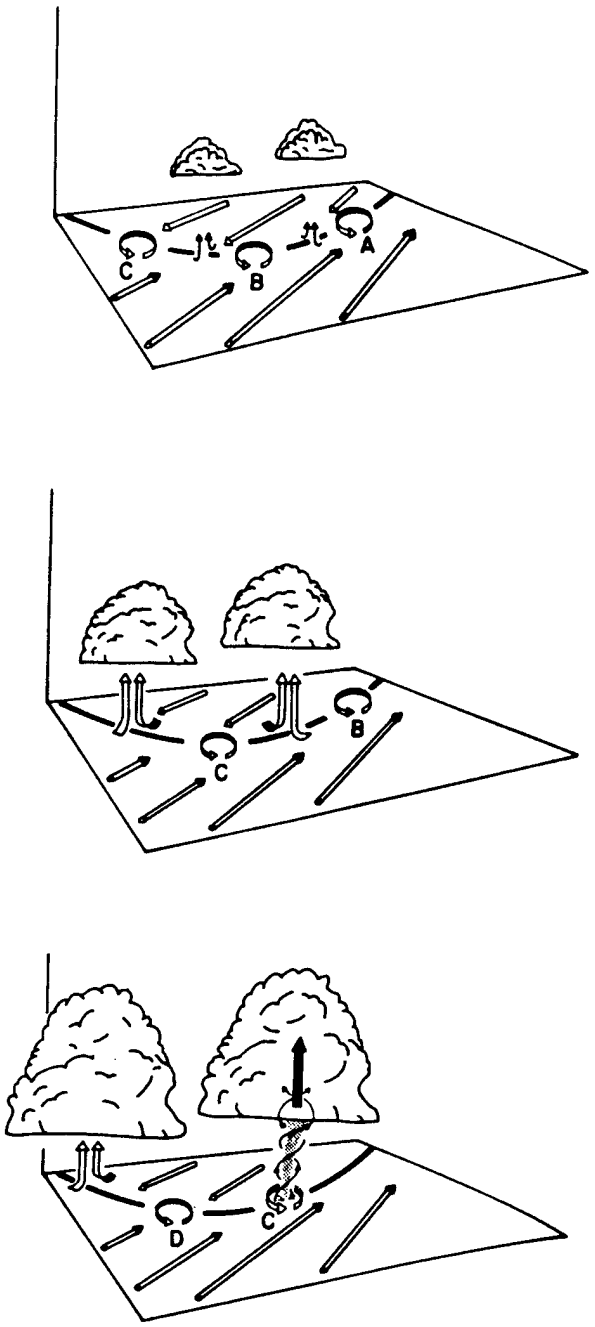

Fig. 4.28 Schematic model from Wakimoto and Wilson (1989) depicting the life cycle of the nonmesocyclone tornado. The thick black line is a radar detectable convergence boundary. Letters label the low-level vortices. Top: Clouds begin to form over the convergence zone. Middle: Strong updrafts develop beneath the growing cumulus clouds. Bottom: A strong updraft becomes superimposed on one of the preexisting vortices and a tornado forms.

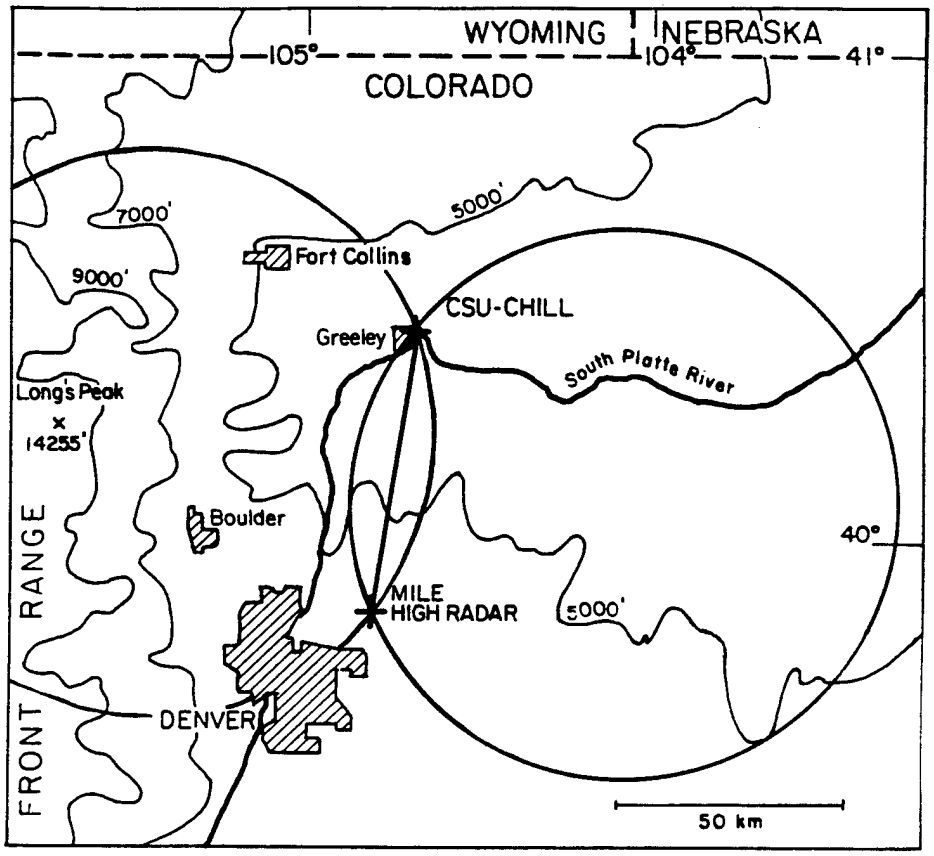

Fig. 4.29 Geographical reference map. The circles depict regions where the CSU-CHILL and MHR beams intersect at an angle of ≥30°. Contours are terrain heights in feet MSL.

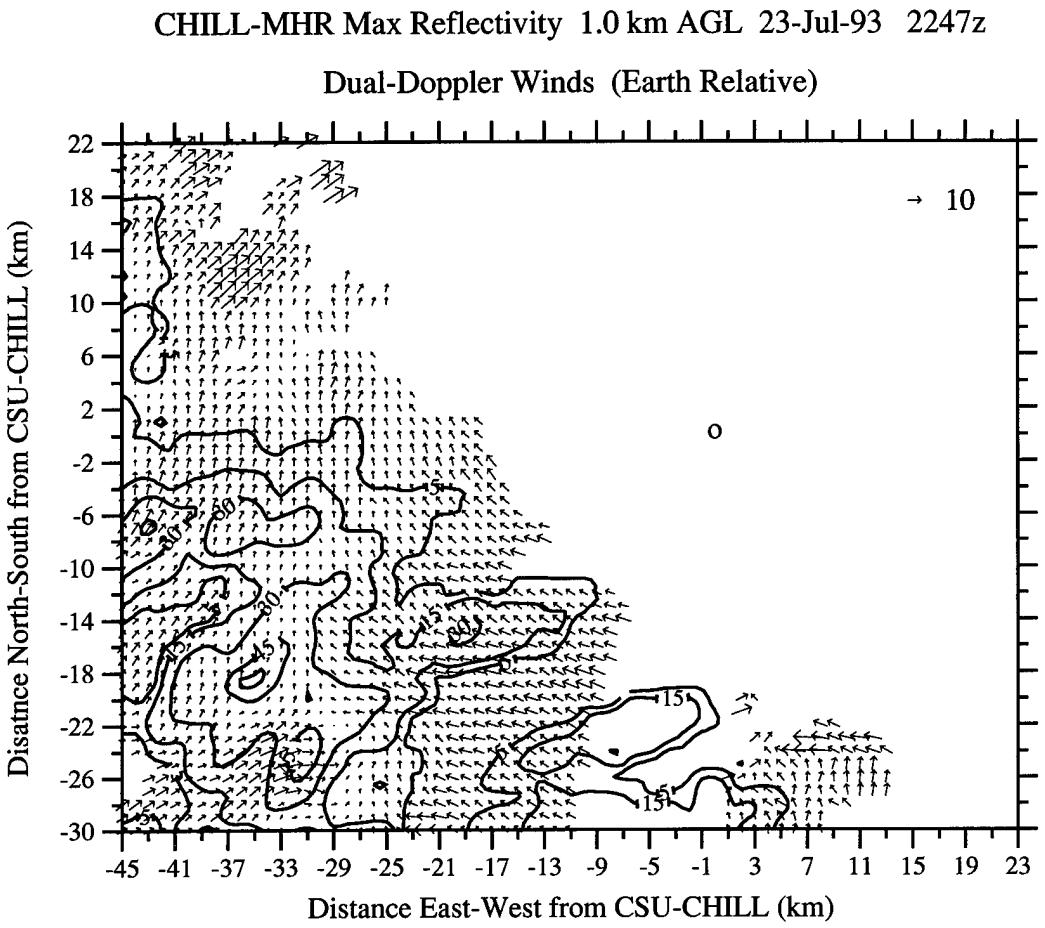

Fig. 4.30 Dual-Doppler analysis at 2247 UTC. Contours are the maximum reflectivity of CSU-CHILL and MHR starting at 5 dBZ. A vector whose length equals one horizontal grid interval represents 10 m s^{-1} (legend in top-right corner of chart).

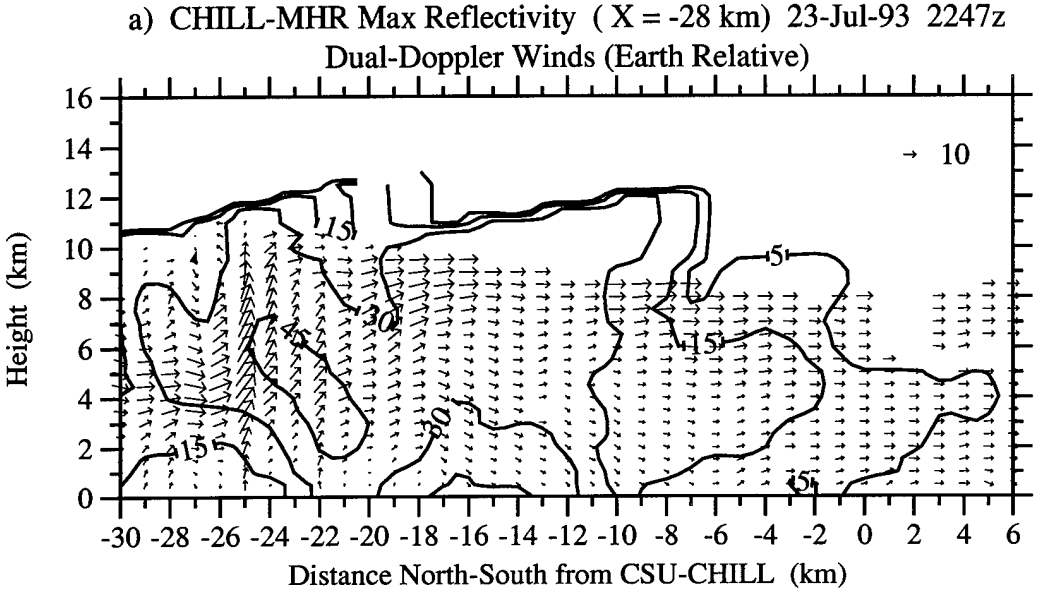

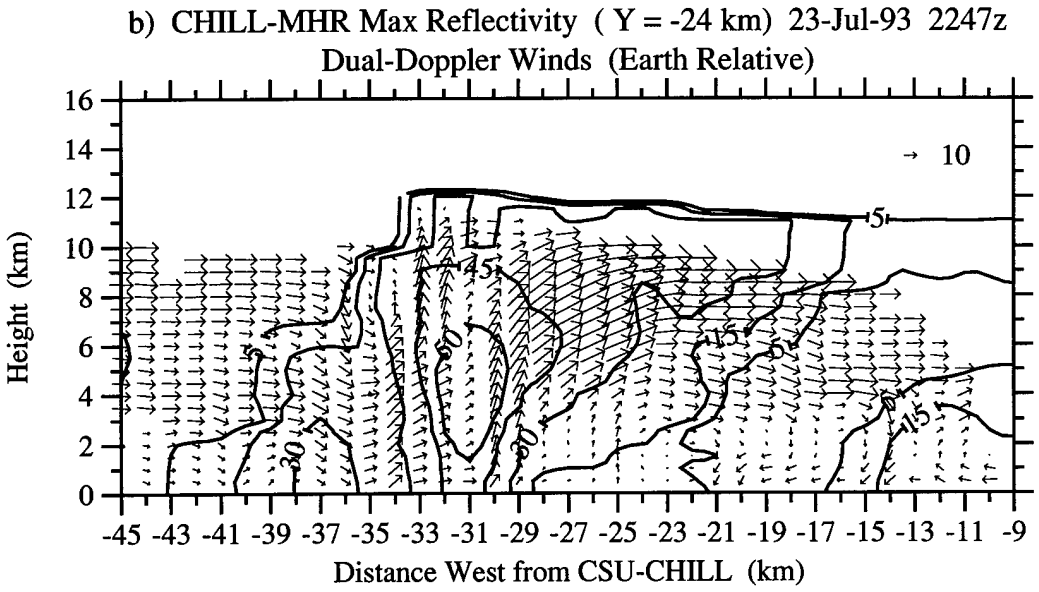

Fig. 4.31 As in Fig. 4.30 except vertical cross-sections at 2247 UTC. (a) X= -28 km, (b) Y= -24 km.

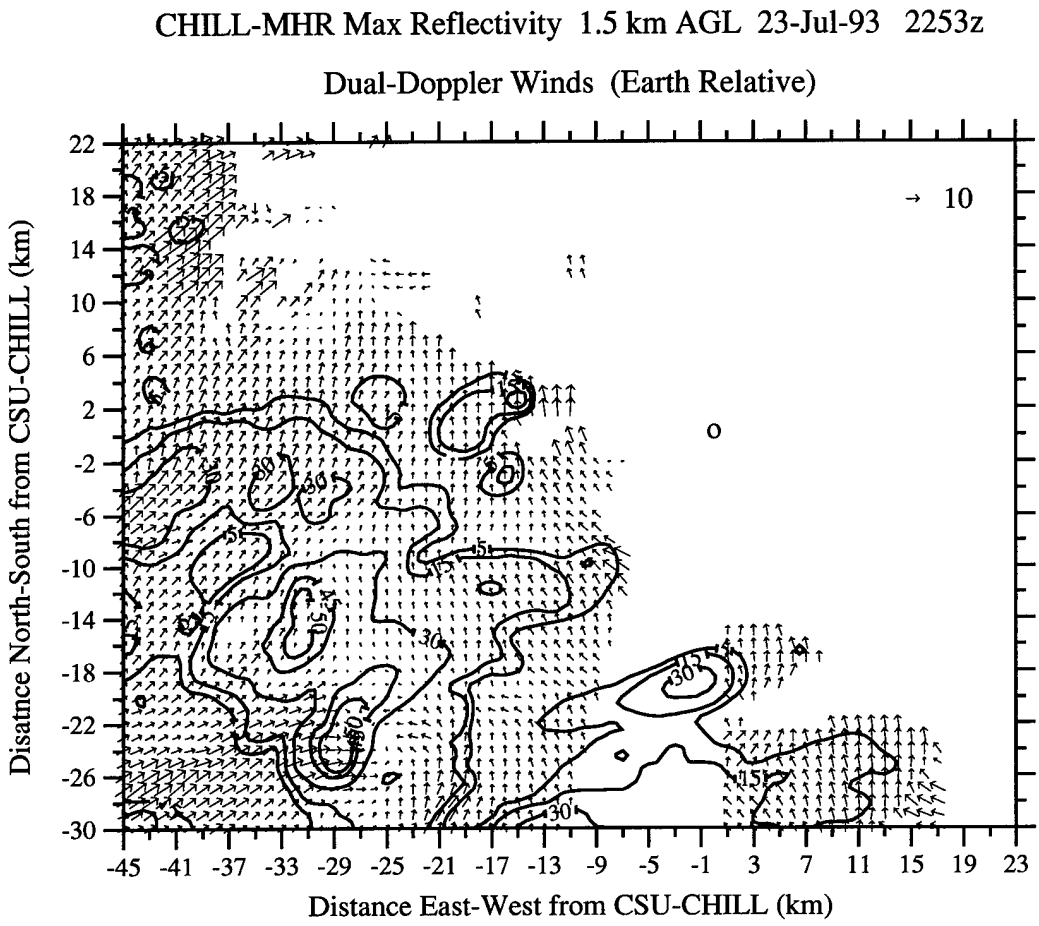

Fig. 4.32 As in Fig. 4.30 except analysis height of 1.5 km AGL at 2253 UTC.

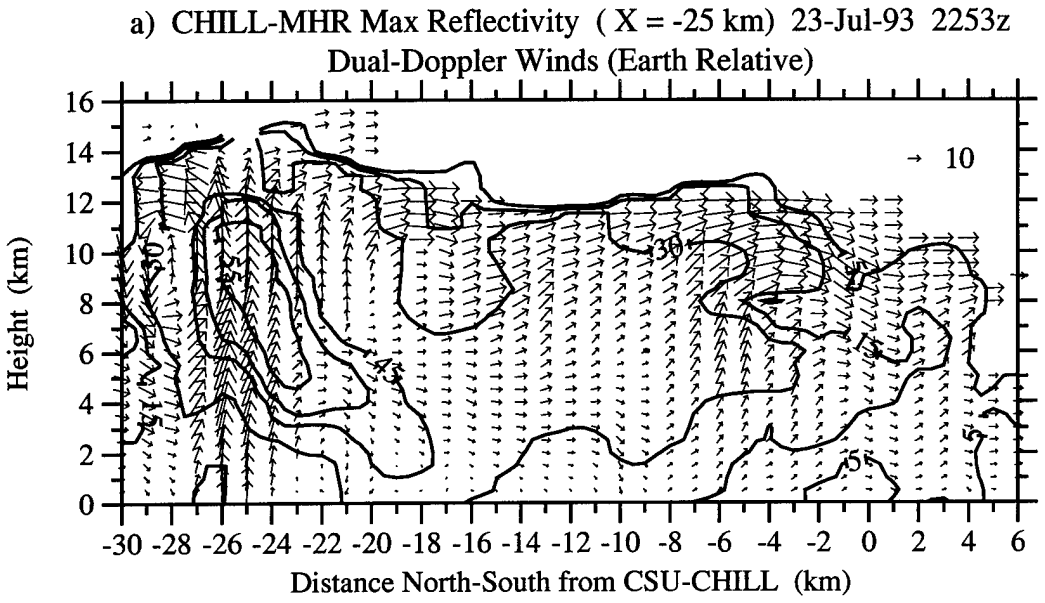

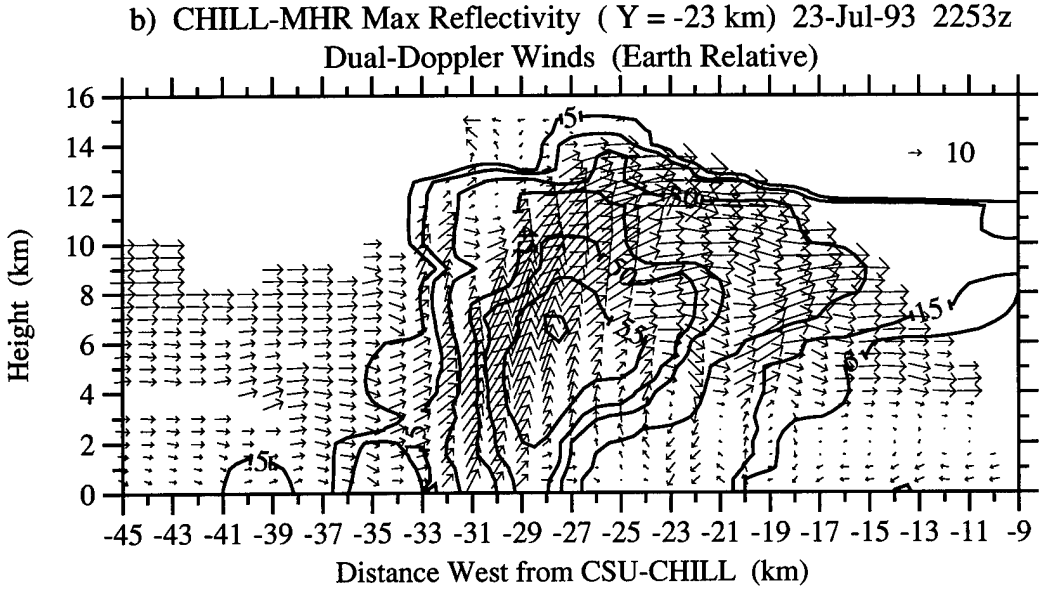

Fig. 4.33 As in Fig. 4.30 except vertical cross-sections at 2253 UTC. (a) X= -25 km, (b) Y= -23 km.

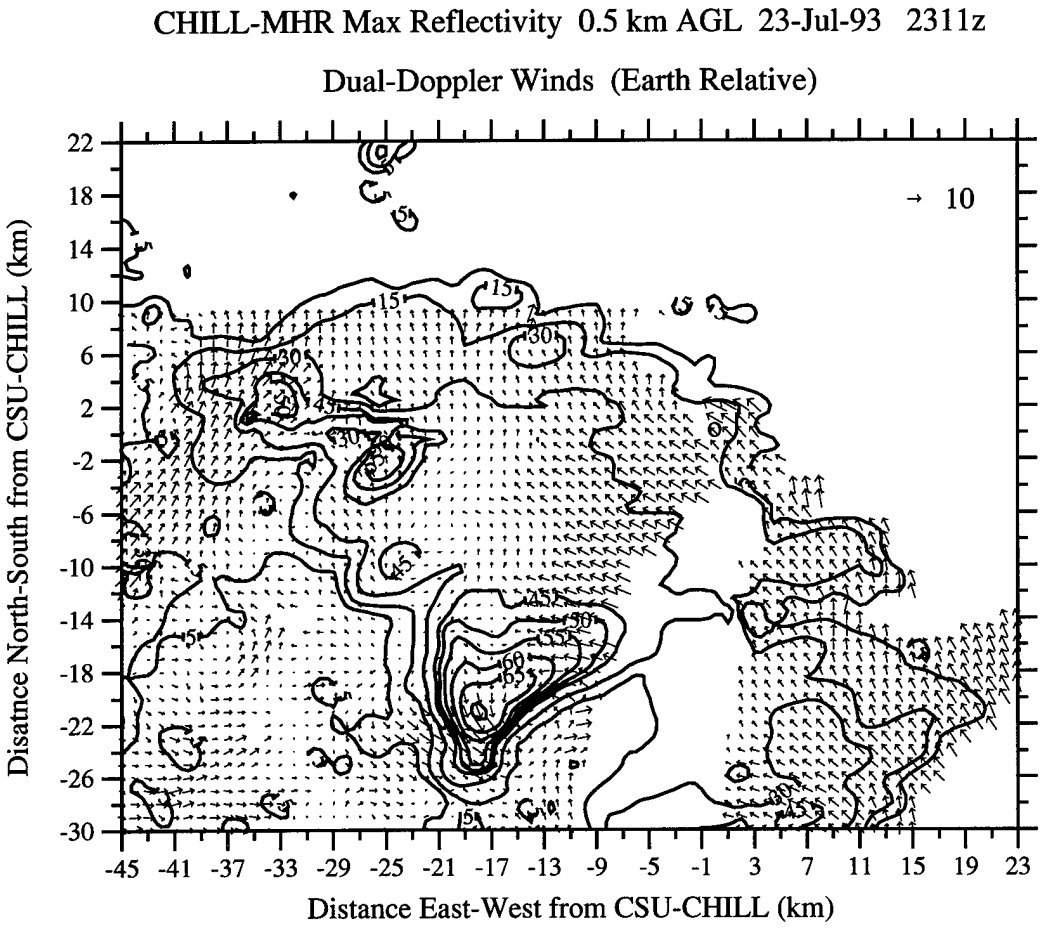

Fig. 4.34 As in Fig. 4.30 except analysis height of 0.5 km AGL at 2311 UTC.

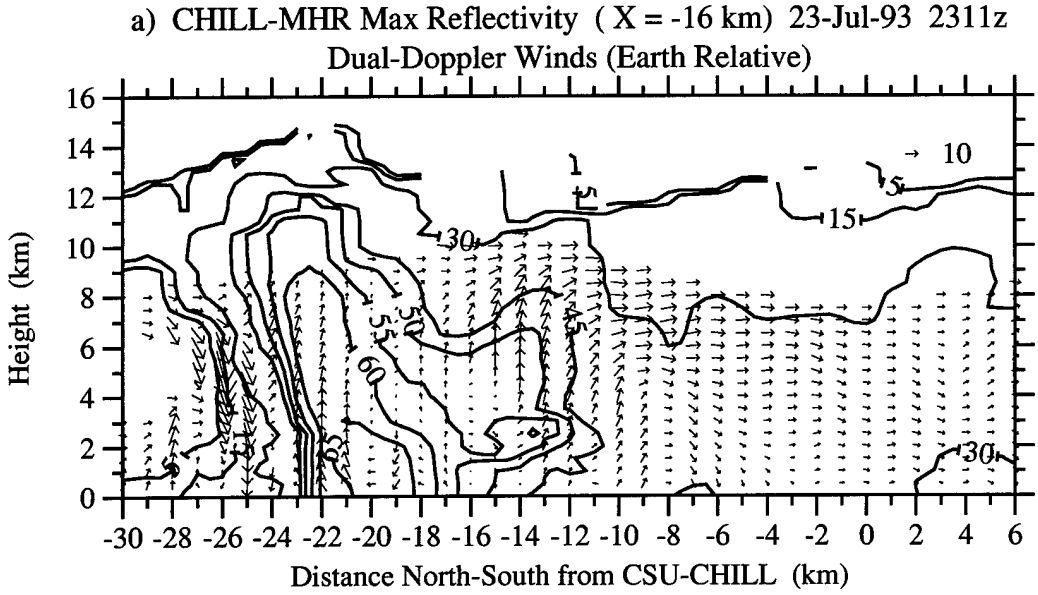

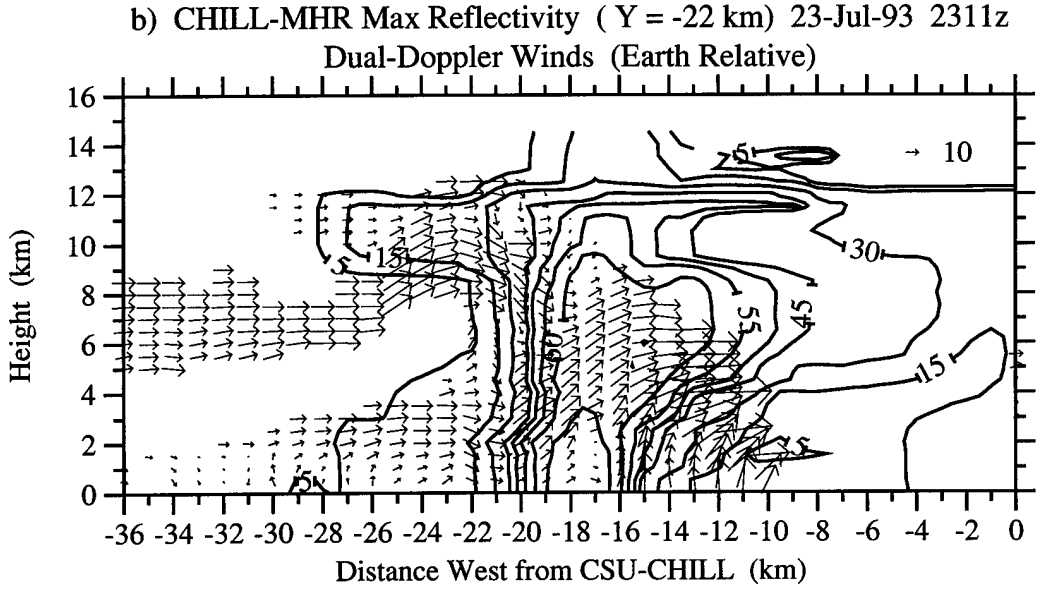

Fig. 4.35 As in Fig. 4.30 except vertical cross-sections at 2311 UTC. (a) X= -16 km, (b) Y= -22 km.

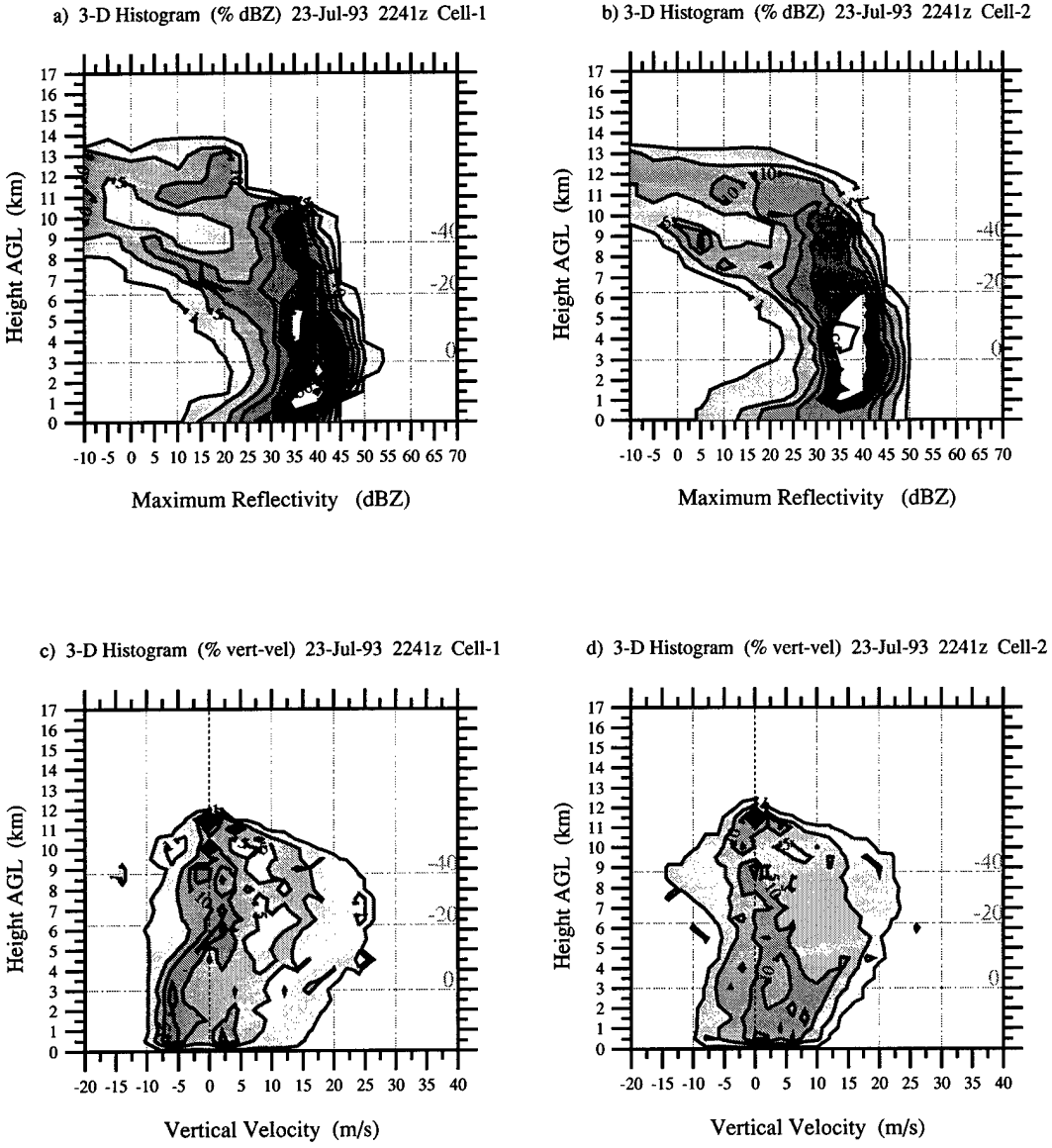

Fig. 4.36 Three-dimensional histograms (CFADs) of radar reflectivity and vertical velocity from 23 July 1993 at 2241 UTC. Contours are percent frequency of occurrence of a value at a given height. Data contour interval is 5% starting at 5%. A 1% contour is included to show distribution outliers. Positive vertical velocity is upward. Horizontal dashed lines denote DEN 0000 UTC, 24 July 1993, sounding temperature (°C). (a) cell-1 reflectivity, (b) cell-2 reflectivity, (c) cell-1 vertical velocity, (d) cell-2 vertical velocity.

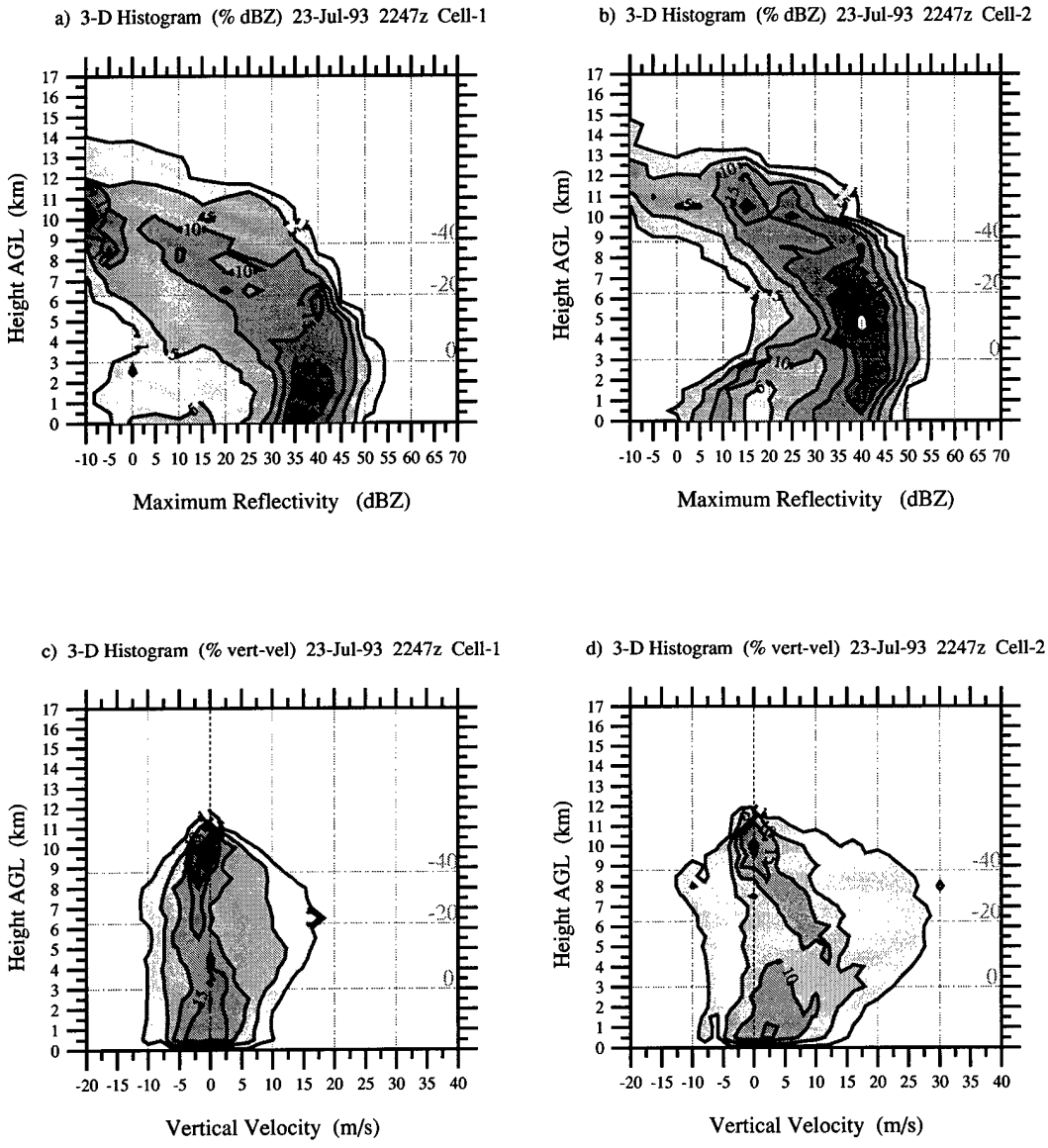

Fig. 4.37 As in Fig. 4.36 except at 2247 UTC.

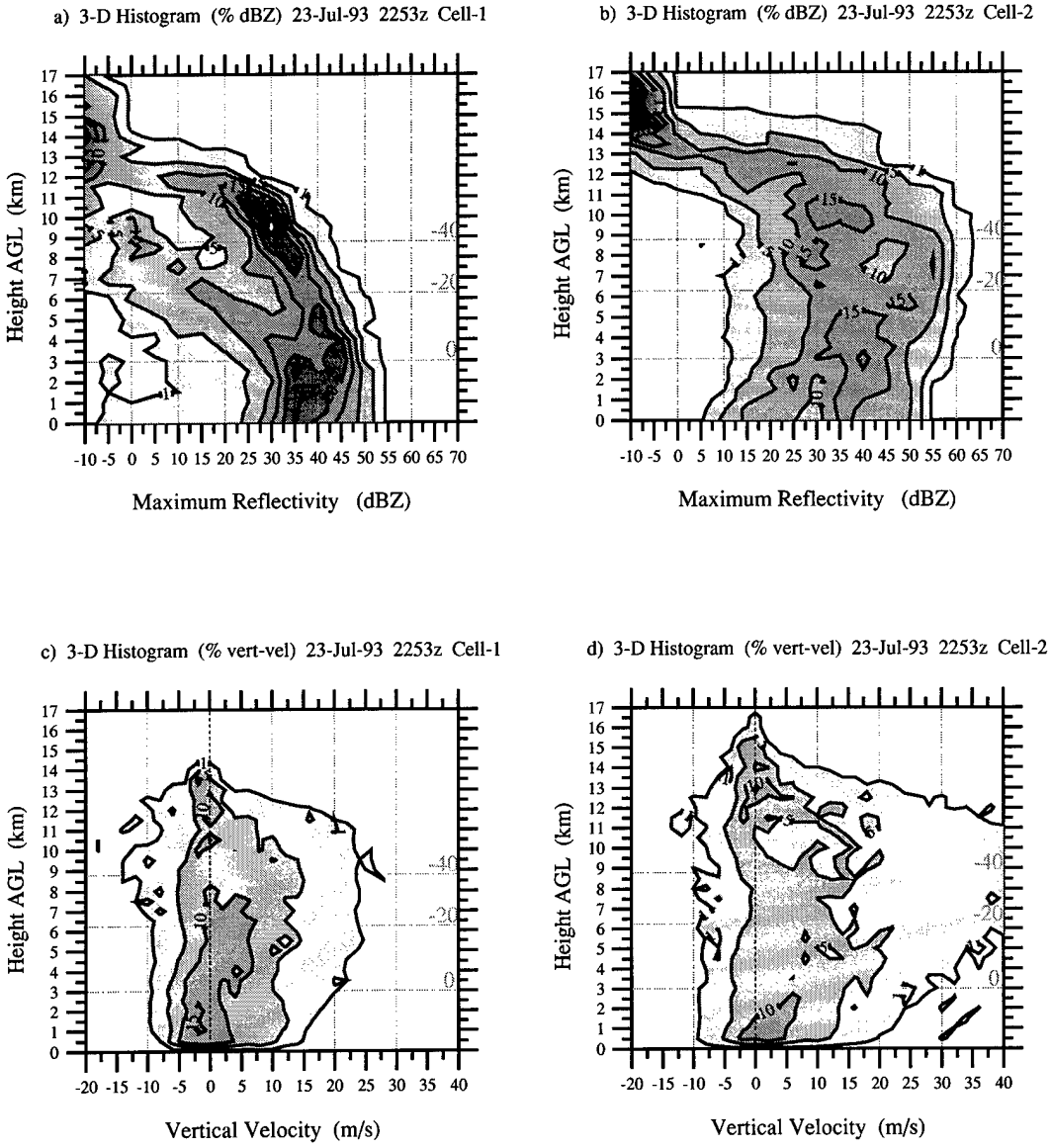

Fig. 4.38 As in Fig. 4.36 except at 2253 UTC.

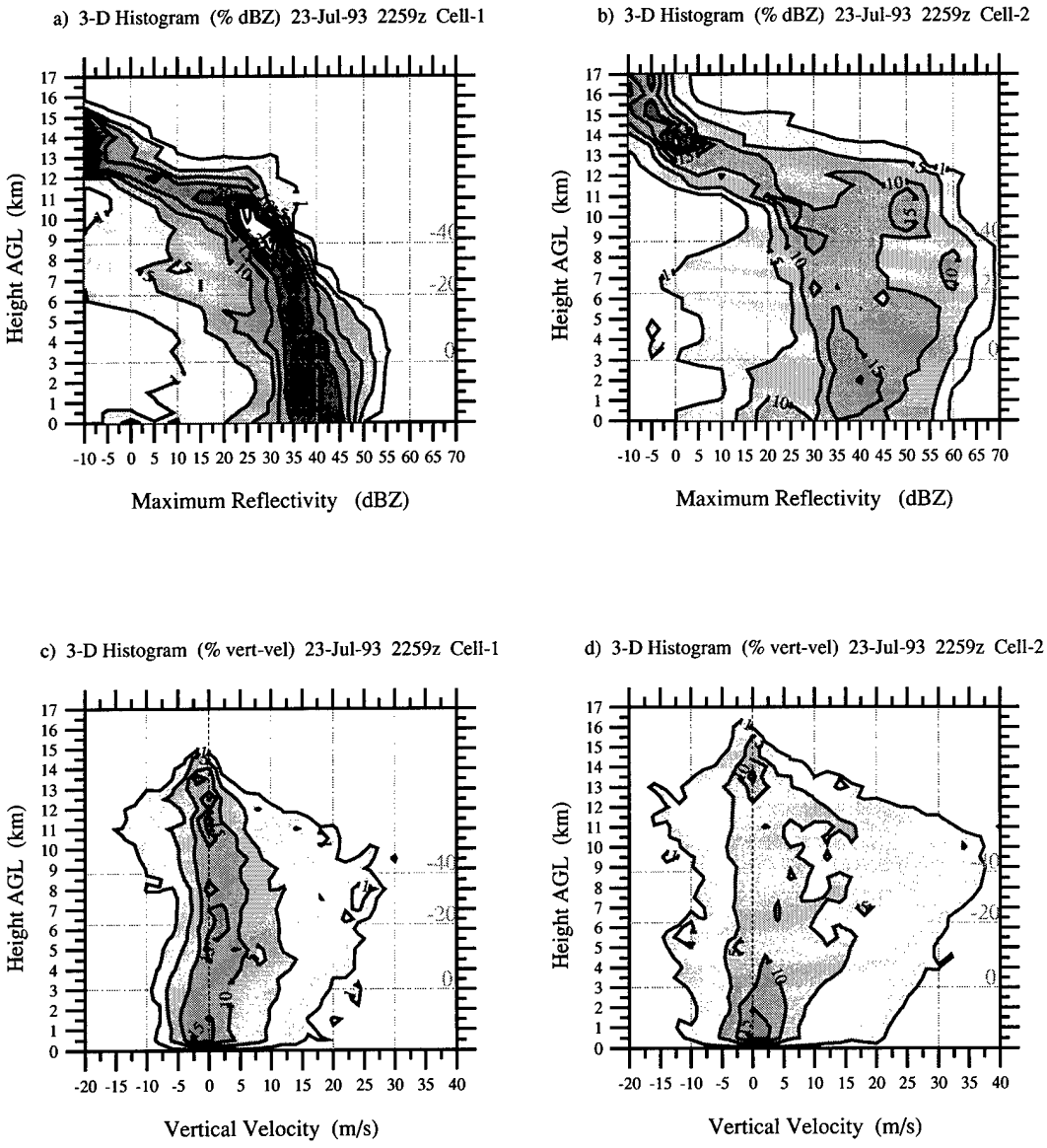

Fig. 4.39 As in Fig. 4.36 except at 2259 UTC.

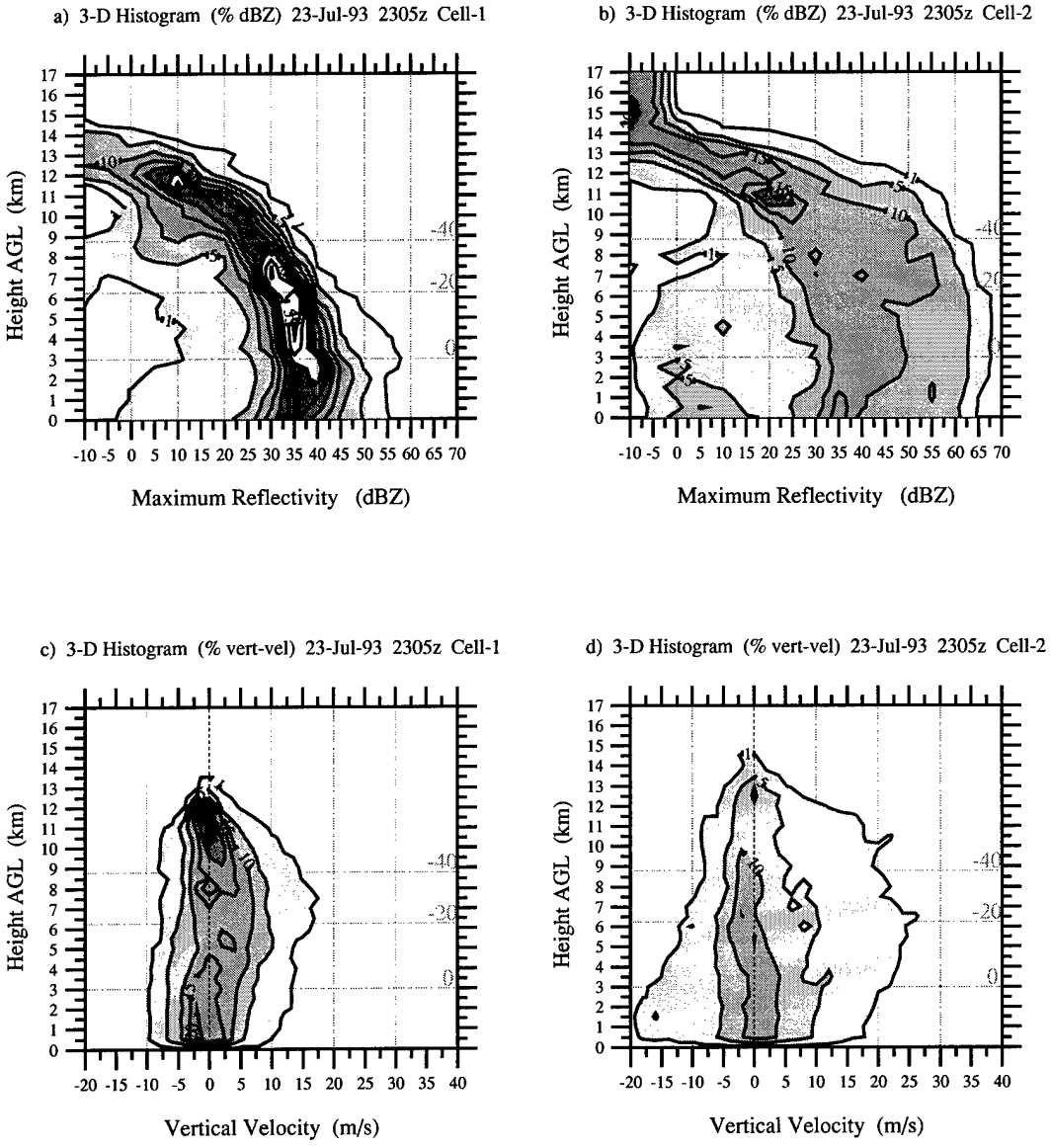

Fig. 4.40 As in Fig. 4.36 except at 2305 UTC.

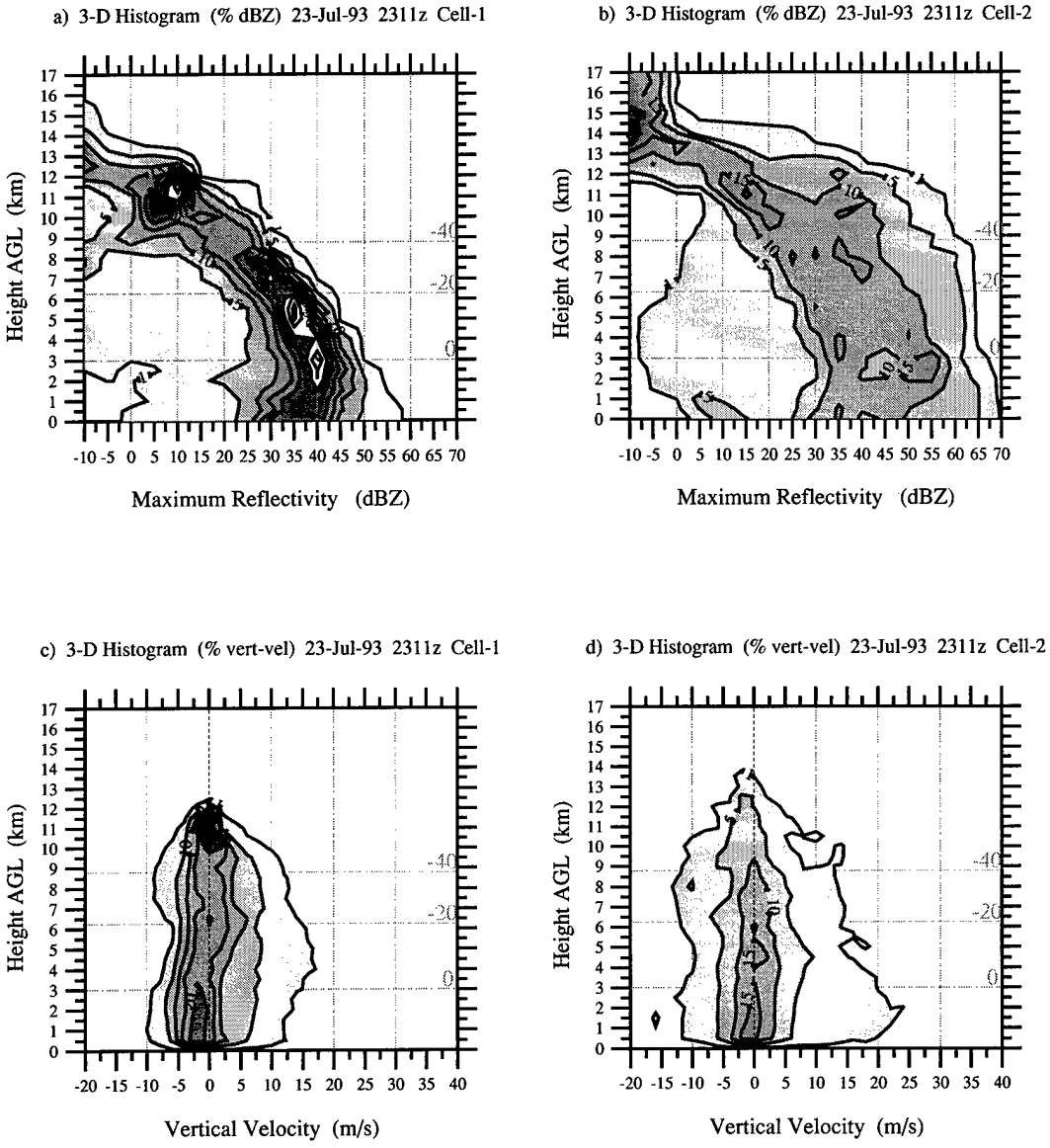

Fig. 4.41 As in Fig. 4.36 except at 2311 UTC.

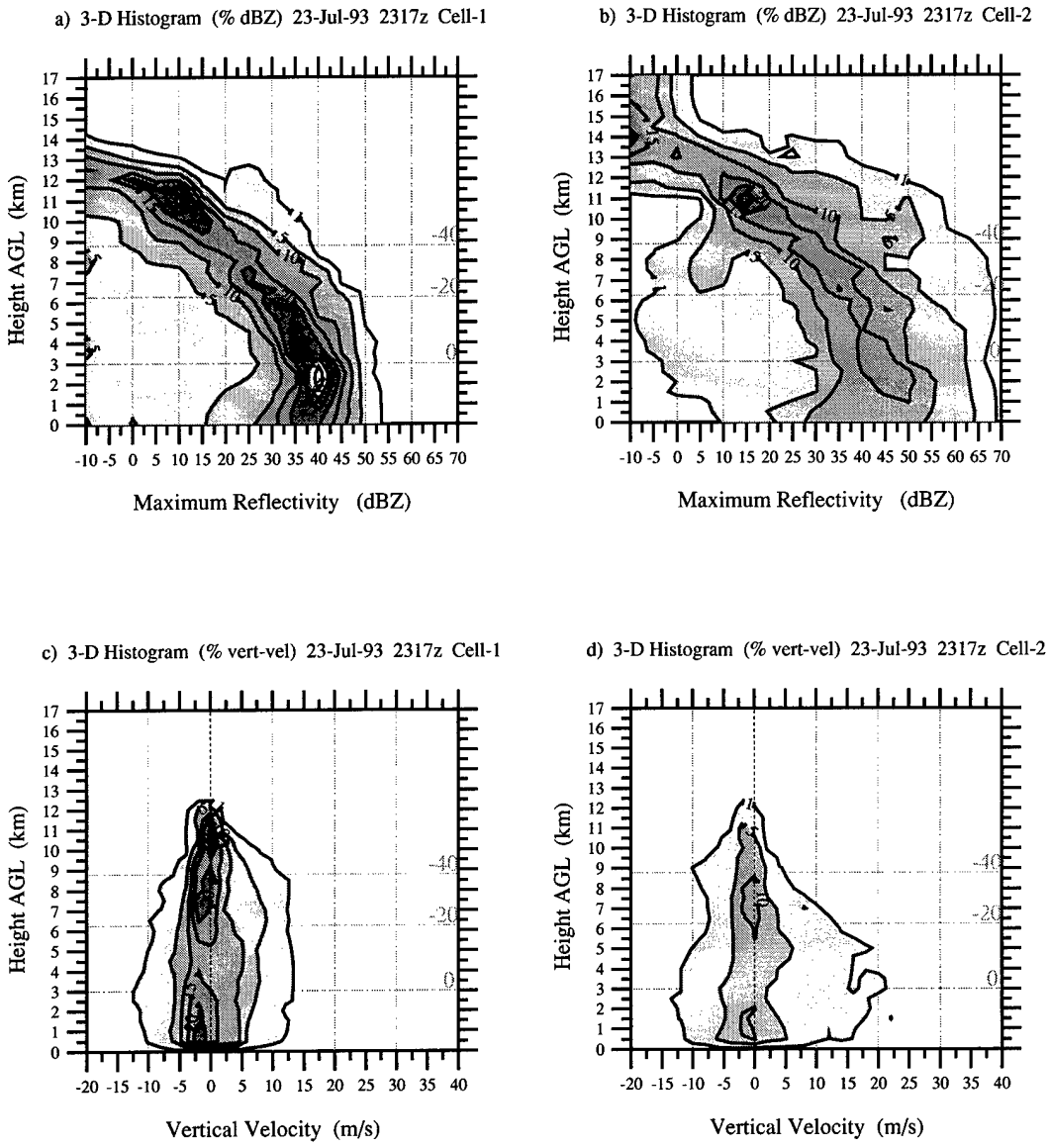

Fig. 4.42 As in Fig. 4.36 except at 2317 UTC.

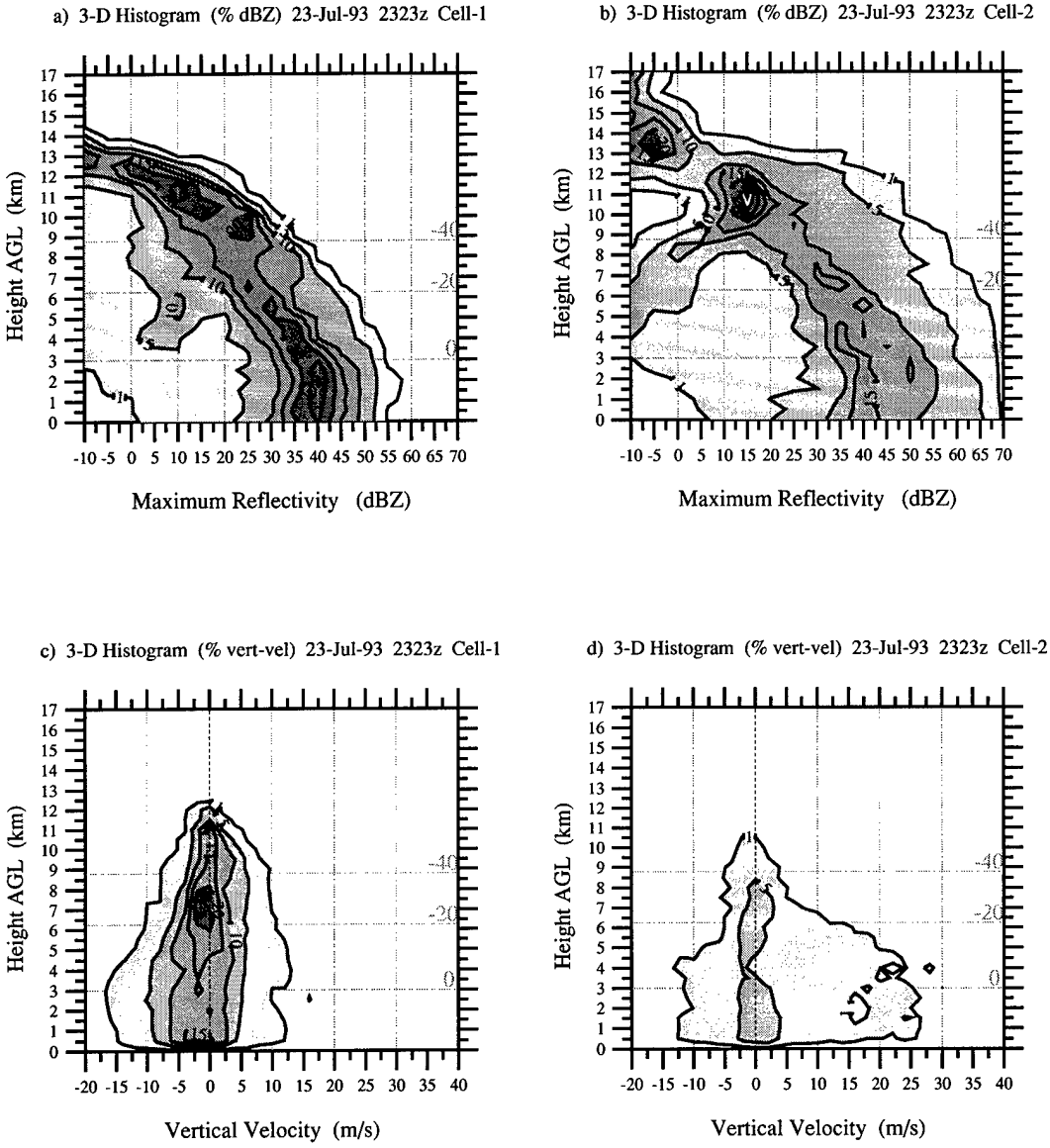

Fig. 4.43 As in Fig. 4.36 except at 2323 UTC.

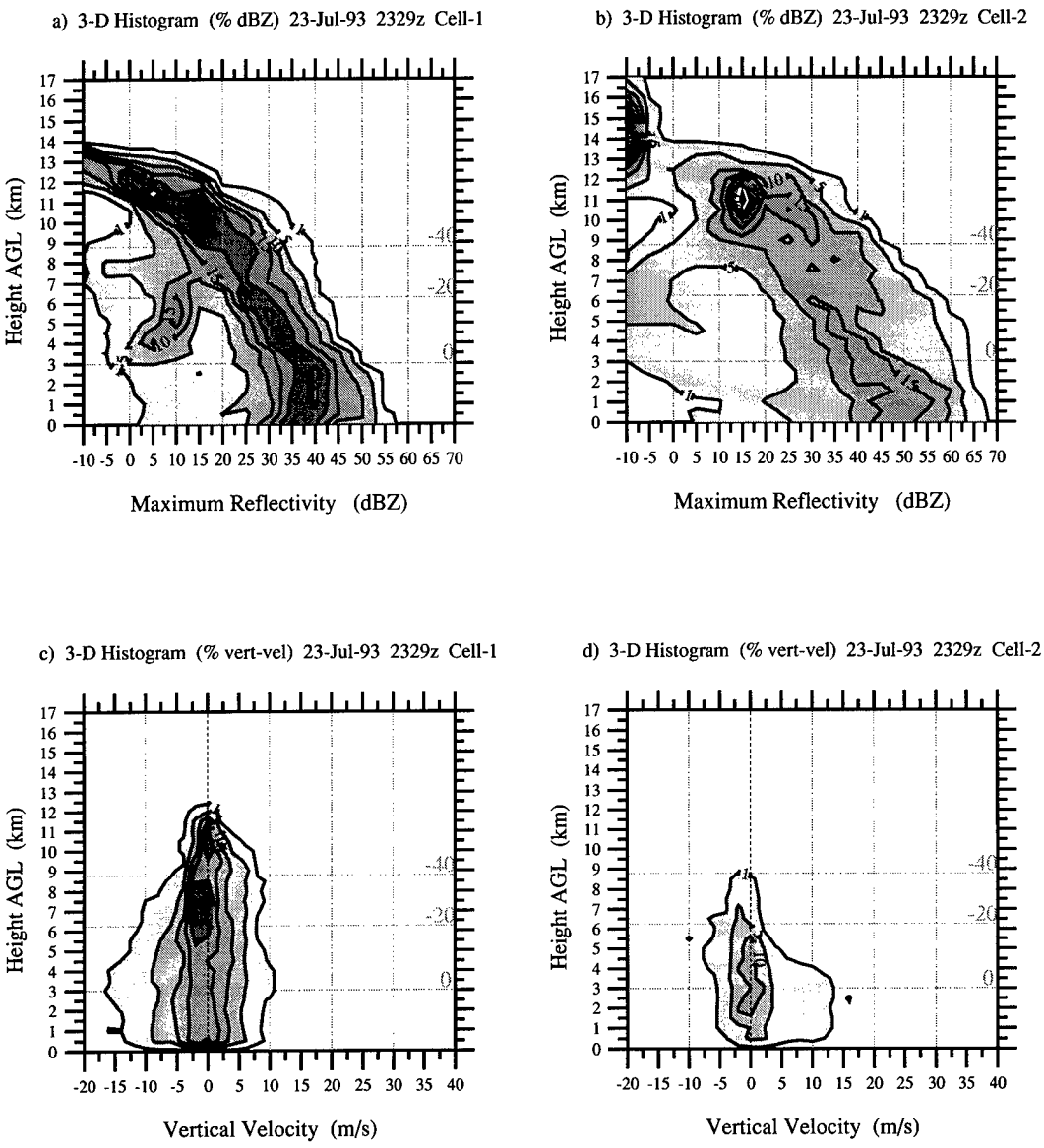

Fig. 4.44 As in Fig. 4.36 except at 2329 UTC.

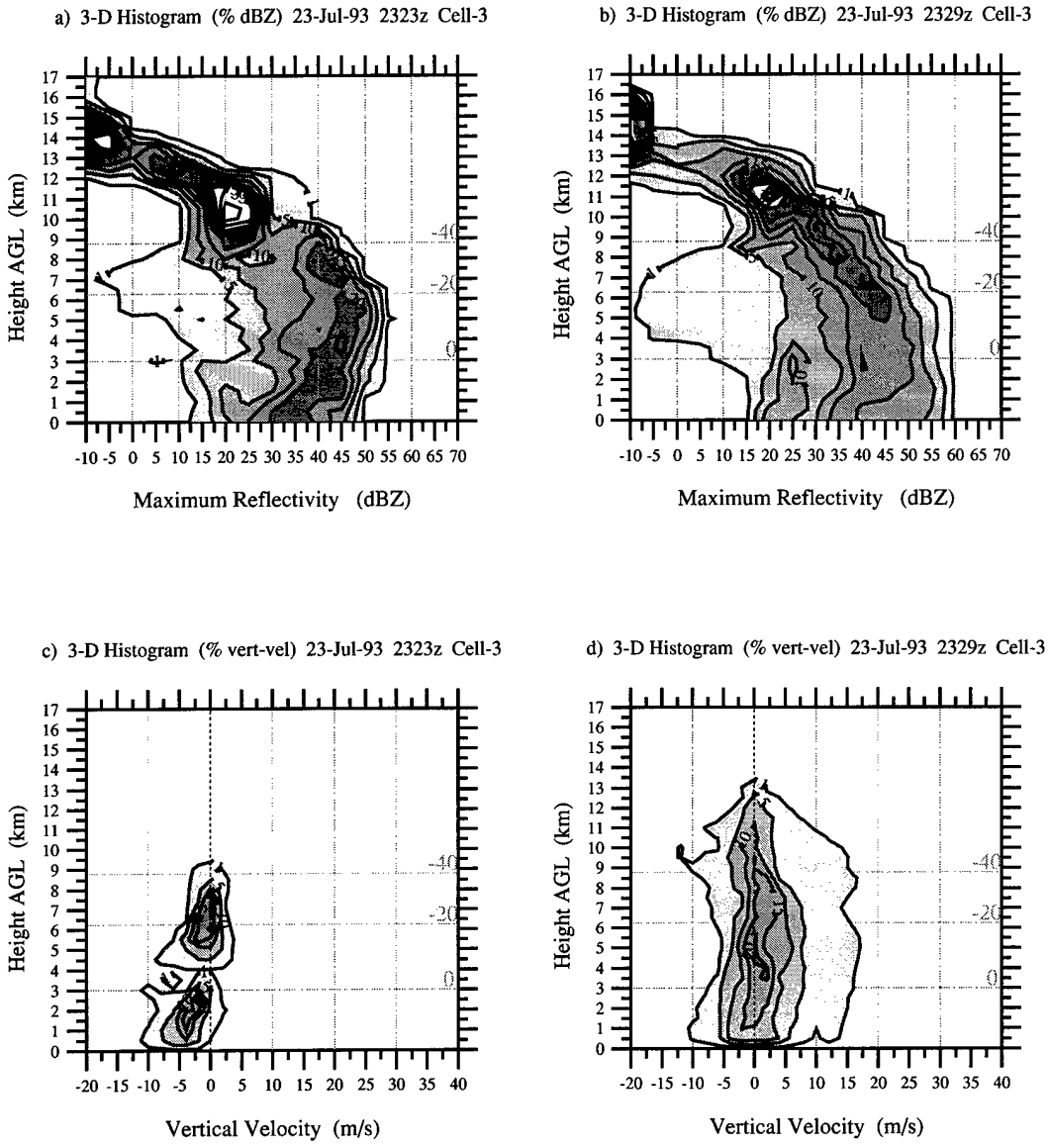

Fig. 4.45 As in Fig. 4.36 except for cell-3. (a) reflectivity at 2323 UTC, (b) reflectivity at 2329 UTC, (c) vertical velocity at 2323 UTC, (d) vertical velocity at 2329 UTC.

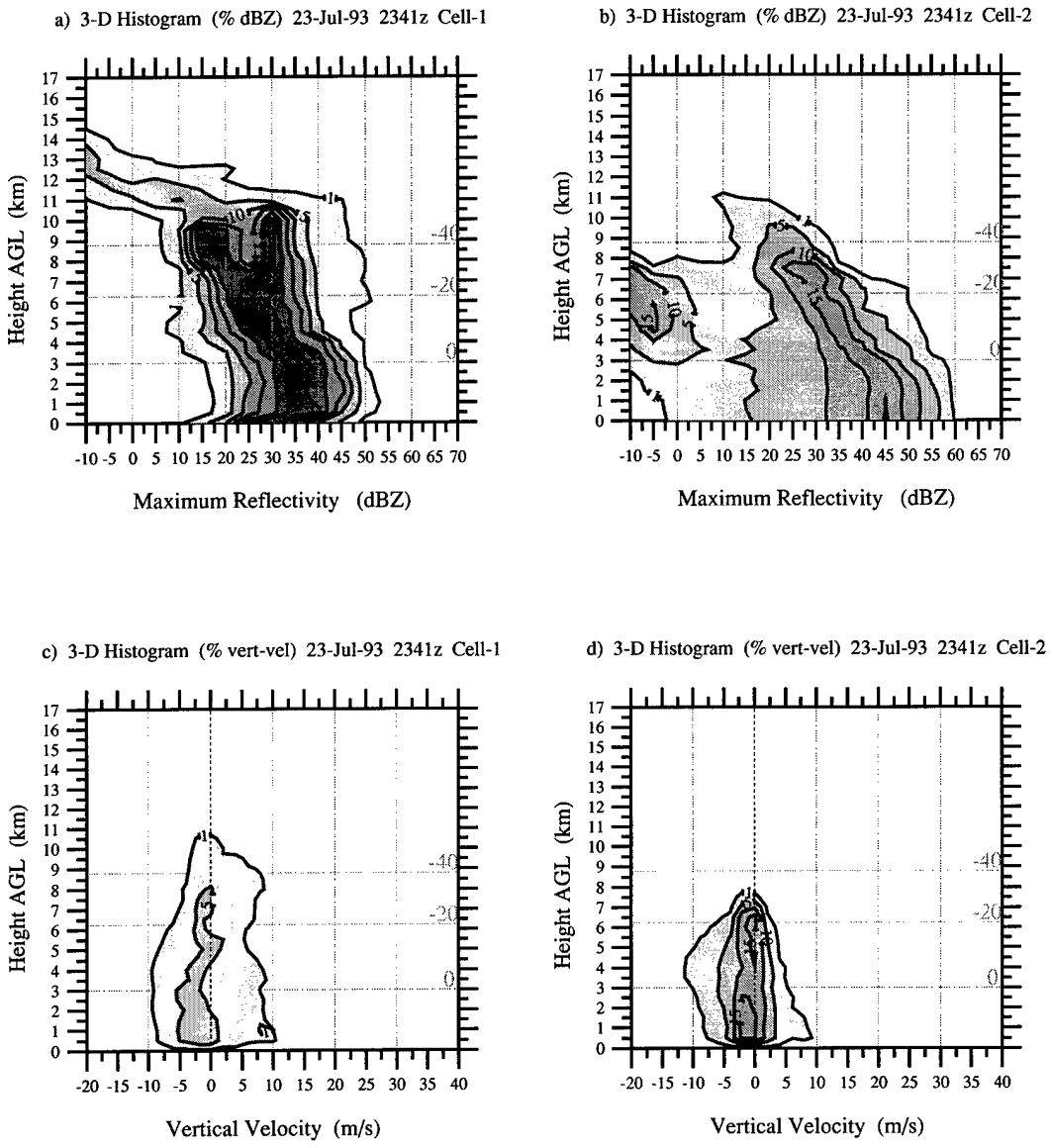

Fig. 4.46 As in Fig. 4.36 except at 2341 UTC.

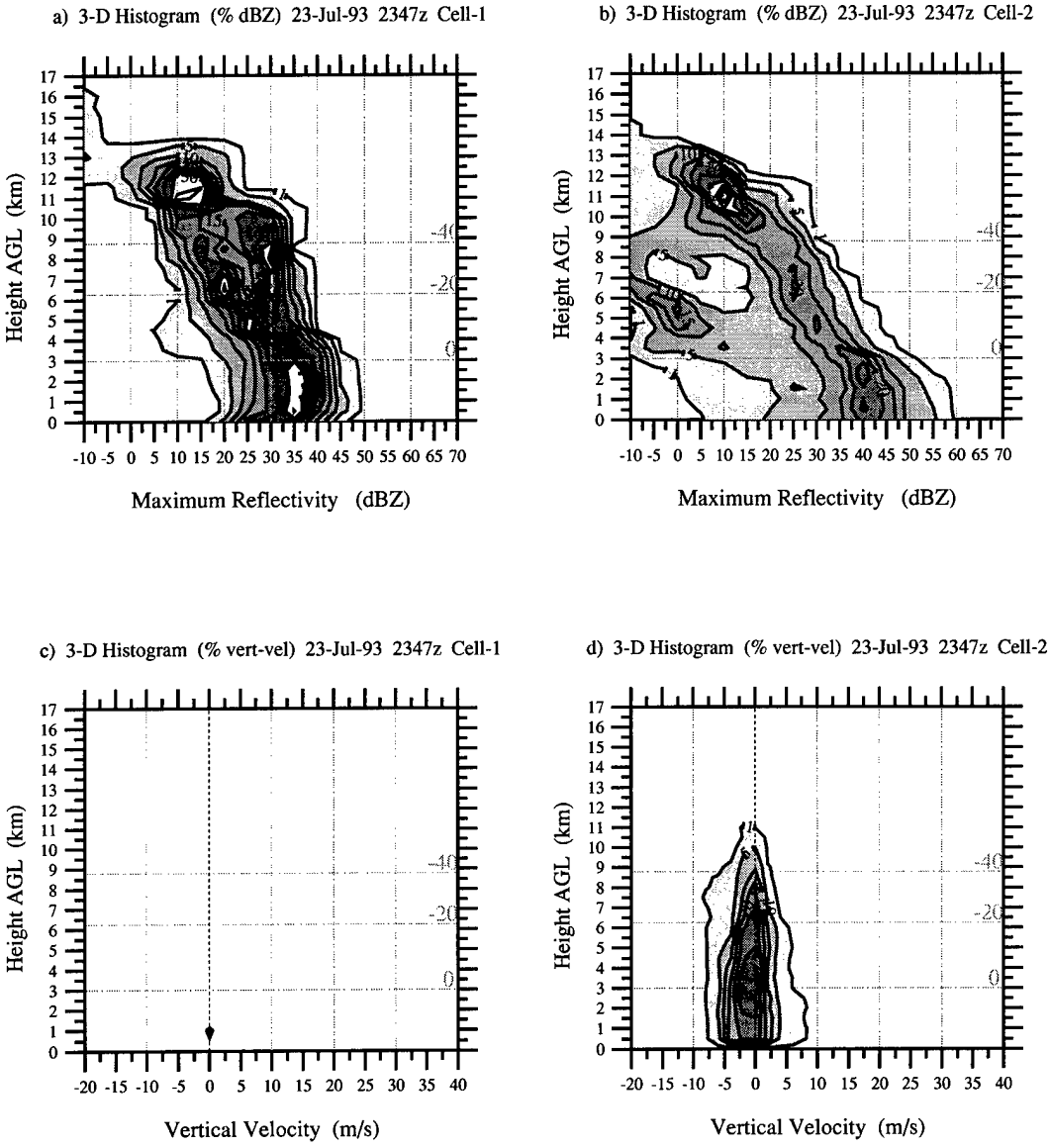

Fig. 4.47 As in Fig. 4.36 except at 2347 UTC.

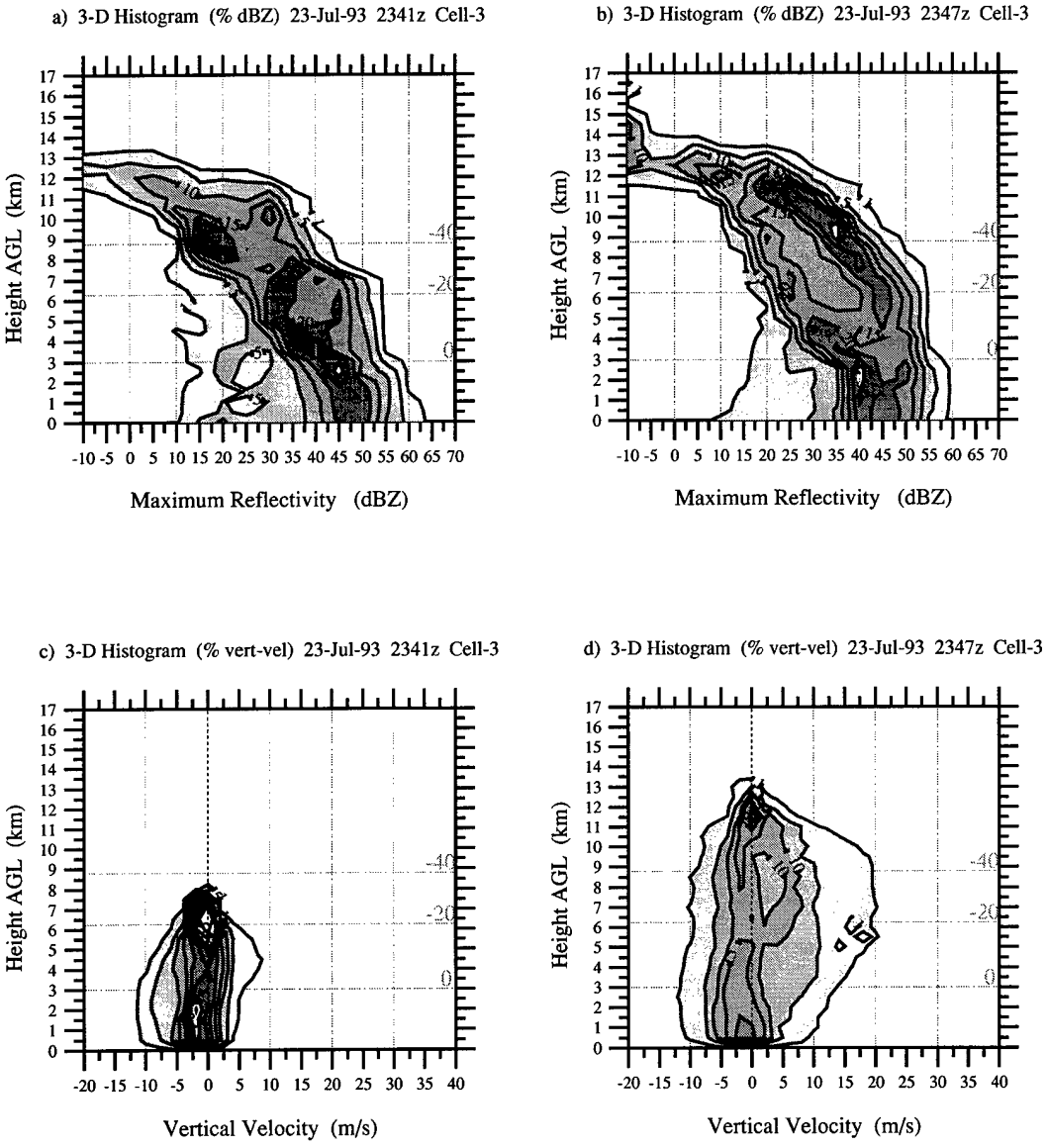

Fig. 4.48 As in Fig. 4.36 except for cell-3. (a) reflectivity at 2341 UTC, (b) reflectivity at 2347 UTC, (c) vertical velocity at 2341 UTC, (d) vertical velocity at 2347 UTC.

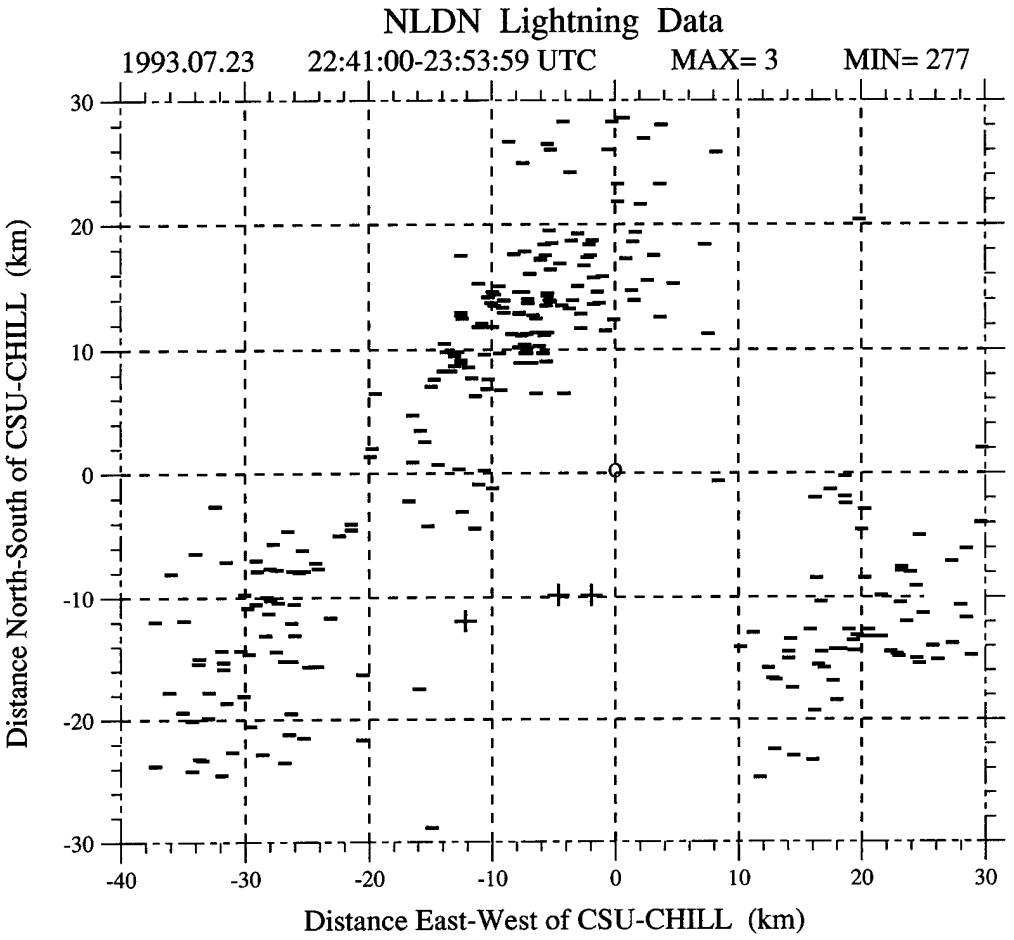

Fig. 4.49 Cloud-to-ground lightning detected by the NLDN from 2241 to 2353 UTC on 23 July 1993. Flash polarity is shown. MAX and MIN are the total number of positive and negative flashes respectively. CSU-CHILL is located at the grid origin.

CHAPTER 5

CASE STUDY 2: NONMESOCYCLONE TORNADO

The microphysical, kinematic, and electrical characteristics of a severe multi-cell thunderstorm observed on 7 June 1995, in northeastern Colorado are described in this chapter. This storm system was the basis of widespread reports of large hail (up to 5 cm diameter), associated crop damage, and sightings of five short-lived, weak tornadoes within a two-hour period (National Weather Service local storm report). Polarimetric radar data was used to infer bulk-hydrometeor types and updraft regions. Single-Doppler radar techniques where employed in the investigation of the evolution of storm rotation and characteristics of the observed CG lightning flashes.

5.1 Synoptic Conditions

Similar to case study 1 (Chapter 4), the meteorological conditions of 7 June 1995 met the criteria described by Doswell's "day-2" scenario for a typical High Plains severe thunderstorm outbreak. A cold front had passed through northern Colorado on 6 June and had become quasi-stationary through the Texas and Oklahoma panhandles. Figure 5.1 depicts the surface conditions at 0600 MDT (Mountain Daylight Time). A surface low pressure center was located near the Four Corners region. Surface temperatures reached 24°C in northeastern Colorado with dewpoint temperatures exceeding 8.8°C by the onset of convection. Surface winds were light and variable with a northeasterly trend in the morning but gradually veered to the southeast by early evening.

At the 500 mb level (Fig. 5.2), a strong closed low was present over the Great Basin with Colorado in a region of weak vorticity and temperature advection. Winds at the 500 mb level over Colorado were in excess of 20 m s^{-1} and a shortwave ridge was present over western Nebraska. Figure 5.3 depicts the 300 mb map at 0600 MDT. The closed low is still obvious over the Great Basin with a jet streak rotating into northeastern Colorado placing this region under its right front quadrant. This quadrant is not typically a favorable region for dynamical forcing of thunderstorms. However, diffluent flow was apparent over northeast Colorado and southwest Nebraska at this time. Winds over Colorado were approximately 36 m s^{-1} at this level.

The NCAR mobile rawindsonde observation (Fig. 5.4) in the region of interest depicted an adiabatic environment from the surface up to a capping frontal inversion at 680 mb (1714 MDT). Above this inversion, the atmosphere was conditionally stable up to 400 mb with the tropopause located at 210 mb. Winds were backing slightly below the inversion but weakly veered above it with slight speed shear present. Modifying this sounding to represent maximum surface dry-bulb and dewpoint temperatures produced only low-to-moderate CAPE values of 752 J kg^{-1} and vertical shear magnitudes of 12.3 m s^{-1} (over the lowest 6 km). These values are not indicative of supercell generation and generally lead to ordinary or multi-cell thunderstorms. However, the sounding did indicate a very low value of convective inhibition (CIN) which would allow the utilization of the positive CAPE with very little forcing required. The hodograph generated from this sounding (Fig. 5.5) shows disorganization near the surface (consistent with generic air-mass type thunderstorms) but tends toward becoming a "straight-line" hodograph aloft. This pattern is more typical of multi-cell storms (Bluestein, 1993).

The Platteville, Colorado wind profiler (Fig. 5.6) indicated veering of the surface winds with time, toward a more southeasterly (upslope) direction. Near the time of interest (1900 MDT) there was favorable directional and speed shear with height. The winds in the upper-levels were strong (40 m s^{-1}) and out of the southwest.

As with the previous case study, this synoptic pattern is not indicative of the typical severe thunderstorm found throughout the Great Plains and Midwest regions. However, most of the key ingredients did exist for the origination of High Plains severe weather outlined by Doswell. The strong capping inversion indicated on the 1714 MDT sounding was a primary factor, allowing the thermodynamic conditions to build until severe weather could be initiated.

5.2 Radar Analysis

Although this storm system passed within observing range of the Denver WSR-88D (KFTG) and CSU-CHILL radars, a dual-Doppler analysis was not feasible because of the scanning strategy employed by KFTG (precipitation mode versus severe storm mode). Also, the CSU-CHILL was not able to scan the top of the storm due to its close proximity, and hence, was unable to sample the upper-level divergence. Multiparameter radar techniques were briefly investigated to help determine bulk-hydrometeor types and infer updraft regions and intensity. Azimuthal shear was calculated for the time period surrounding the formation of a weak tornado. Three-dimensional histograms were constructed to gain insight into the volume reflectivity patterns.

5.2.1 Storm Morphology

Severe thunderstorm activity was widespread in northeastern Colorado during the early evening hours of 7 June 95. The CSU-CHILL was supporting a summer-time field

operation and its radar-directed chase teams observed large hail (up to 4 cm diameter) and heavy rain while intercepting a strong echo core shortly after 1800 MDT (this is the storm under investigation in this chapter). During the subsequent hour, this storm system tracked to the northeast and produced three reported short-lived tornadoes and generated numerous reports of large hail throughout a sparsely populated region of Weld County, Colorado. Radial velocity data indicated that the low-level inflow to the storm was from the east. By 1900 MDT, a severe cell had passed within 15 km to the south-southeast of the CSU-CHILL radar site. Because of its proximity to the radar, several unique small-scale patterns were identifiable in the radar's reflectivity and radial velocity fields. An irregular curtain of hail extended to the surface adjacent to the storm's main updraft region and was the location of a confirmed weak tornado at 1856 MDT. The CSU-CHILL was operated in a sector scan mode and followed the storm's motion.

Figures 5.7 and 5.8 depict the storm evolution from 1830 to 1951 MDT along with the associated CG lightning flashes detected by the NLDN. Radar images used in this overview are from KFTG and are presented as 1.0 km CAPPIs in 12-minute increments. The CG lightning flashes annotated occurred from the start of the particular radar volume to the start of the following volume. MAX and MIN values indicate the number of detected positive and negative CG flashes respectively. The small circle at the origin represents the location of the CSU-CHILL radar.

Figure 5.7a shows the start of the developing hail curtain (X= -7 km, Y= -17 km) protruding along the southern flank of the northern-most cell. During a longer period encompassing this analysis (1748 to 2048 MDT) Carey and Rutledge (1996b) reported that over 68% of all detected CG flashes were of positive polarity with peak positive flash rates

of 7 min^{-1}. By 1853 MDT (Fig. 5.7c), the hail curtain (appearing as a flanking line with high reflectivity between two echo cores) was fully formed (centered near X= 1 km, Y= -12 km). Noteworthy is the position of the predominant positive lightning flashes upshear of the low-level reflectivity core. Figure 5.7c is the closest volume depicted near the time of the observed tornado located 3 miles southwest of Kersey, Colorado at 1856 MDT (approximately located at X= 2.3 km and Y= -9.6 km and annotated with a small "T"). During the 35-minute evolution shown in Fig. 5.7, the northern cell moved slowly (<6 m s^{-1}) almost due east while the cell to its south was moving faster to the northeast. Figure 5.7d (1951 MDT) depicts the merger of these two cells.

The continued evolution of this storm system is shown in Fig. 5.8. During this time period (1916 to 1951 MDT) the storm continued to slowly propagate to the east-northeast while pulsating in intensity, shape, and CG lightning production. This system persisted in the production of large hail and several more small tornadoes for the next 2 hours while taking on more squall-line characteristics. Cloud-to-ground lightning activity monitored until 2048 MDT remained predominately positive in polarity.

5.2.2 Multiparameter Investigation

The main investigation of this storm centered around the observation of a tornado at 1856 MDT. To better understand the microphysical composition of this thunderstorm and infer some basic kinematic properties, multiparameter radar data was briefly analyzed. The term multiparameter refers to the transmission and reception of orthogonal, linear-polarized waves, preferably of the same pulse volume (Doviak and Zrnić, 1993). In the case of the CSU-CHILL radar, these orthogonal waves are transmitted on an alternating basis, with each pulse separated by 1 ms. Multiparameter radar allows inferences of hydrometeor

characteristics such as particle size, shape, thermodynamic phase, and spatial orientation. Besides the conventional horizontal reflectivity, Z_h, two multiparameter variables were used in this study: 1) differential reflectivity, Z_{dr} and 2) specific differential phase, K_{dp}.

Differential reflectivity is used as an indicator of particle shape (oblateness) and orientation and is defined as

$$Z_{dr} = 10\log_{10}(Z_h/Z_v) \ [\text{dB}] \tag{5.1}$$

where $Z_{h,v}$ is the copolar radar reflectivity factor of a horizontally and vertically polarized wave respectively. For a single Rayleigh target

$$Z_{h,v} = (\pi^5/\lambda^4) \ |K_w^2| \ D_{h,v}^6 \ [\text{dBZ}] \tag{5.2}$$

where λ is the radar wavelength, $|K_w^2| = 0.93$ is the complex index of refraction for water, and $D_{h,v}$ is the horizontal and vertical particle diameter respectively. Equations (5.1) and (5.2) show that Z_{dr} is related to the reflectivity weighted mean axis ratio of the particle which is a known function of equivalent drop diameter. Raindrops with diameters ≥ 1 mm deform into oblate spheroids, due to aerodynamic forces, with a preferred orientation of the major axis being horizontal and the eccentricity dependent on equivalent spherical diameter (Pruppacher and Beard, 1970). Therefore, Z_{dr} is positive for raindrops and increases for larger drop sizes. Hail and graupel particles tend to be more spherically symmetric or exhibit random tumbling and result in $Z_{dr} \approx 0$. Even though ice crystals and aggregates may not be spherical or may be prolate, the combination of low bulk density and low dielectric factor typically results in low Z_{dr} values.

Specific differential phase, K_{dp}, is the calculated range derivative of differential phase, ϕ_{dp}. Differential phase is a result of forward scattering through a medium such as hydrometeors. The differential phase is measured by examining the phase shift that develops

between the horizontal and vertical radar returns as a wave propagates through an anisotropic medium. Differential phase is defined as

$$\phi_{dp} = \phi_{hh} - \phi_{vv} \text{ [degrees]} \tag{5.3}$$

where ϕ_{hh} is the cumulative phase shift for the complete round trip between the radar and resolution volume for a horizontally polarized transmitted and received electromagnetic wave and ϕ_{vv} is the vertically polarized equivalent. Spherical hydrometeors theoretically produce equal phase shifts for either polarization. Any differential phase will be due to the non-spherical nature of the hydrometeors, especially those particles with substantial dielectric factors such as oblate raindrops (Doviak and Zrnić, 1993). Jameson (1985) has demonstrated that K_{dp} is nearly linearly related to rainfall rate. Several advantages of K_{dp} measurements shown by Chandrasekar et al. (1990) are 1) it is independent of radar receiver/transmitter amplitude calibrations, 2) it is essentially immune to partial beam filling, 3) it is unaffected by attenuation, 4) there is usually little bias due to the presence of hail, and 5) it is relatively insensitive to drop-size distribution. These advantages are rooted in K_{dp}'s independence from signal amplitude measurements.

Figure 5.9 is an example of multiparameter measurements obtained during the intense phase of the hail curtain (1849 MDT) and prior to the tornado observation. The thin line of moderate to high reflectivity separating the two cells to the northwest/southeast of each other (Fig. 5.9a) was originally thought to be a flanking line or storm outflow boundary. Upon closer inspection of the Z_{dr} and K_{dp} values, it became evident that this region consisted of mostly hail with little or no raindrops. In Fig. 5.9a, only Z_{dr} values of -0.5, 0, and 0.5 dB are contoured for clarity. Given this thin area of high reflectivity, Z_{dr} values are uniformly between -0.5 and 0 dB consistent with the presence of large hail. Furthermore, K_{dp} values

are low in this region in contrast to the other high reflectivity areas of the storm indicating the lack of liquid precipitation in the hail curtain region. The north-south dashed line in Fig. 5.9a represents the vertical cross-section of Fig. 5.9b. The reflectivity pattern of the cross-section shows the vertical extent of this "thin line." Hence, the realization that this was not a shallow feature associated with the storm's low-level outflow. The reflectivity also shows an intense core suspended above a bounded weak echo region (BWER). Z_{dr} measurements in this BWER are positive, well-above the freezing level (1.7 km AGL), indicative of supercooled water droplets suspended and lifted upward by a strong updraft. The source of these supercooled drops was most likely melted ice particles being recycled into the echo core. Between 9.5 and 12.5 km south of the radar, there are regions of high reflectivity and low Z_{dr} ($\approx$ 0) inferring the presence of large hail near the surface. Closer to the radar, an area of stratiform-type precipitation can be presumed by the horizontal gradient of Z_{dr} below the freezing level caused by the melting of graupel into oblate raindrops. This area is coincident with the region of high K_{dp} shown in Fig. 5.9a.

To better formulate an understanding of the spatial structure of this storm, a three-dimensional surface of 55 dBZ reflectivity (1849 MDT) was constructed (Fig. 5.10), representing the area depicted in Fig. 5.9a. The angle of view is from the east-southeast with the radar located to the right of the page. Evident in this figure is the BWER coincident with the implied updraft, the large hail/ice mass suspended aloft, the connection between the hail curtain and the northwest echo core of the storm, and a physical connection aloft between the two main echo core regions. An additional overhang of the suspended high reflectivity mass is visible and would have been more dramatic given a broader radar sector scan at the higher elevation angles. It is proposed that this storm's intense updraft of supercooled

droplets aided in the rapid production of large hail. This suspended ice mass was so great that not only did hail fall through the main echo core of the storm (mixed with heavy liquid precipitation) but much of it descended along side (south) of the updraft region forming a large "curtain" of hail. Drag-induced downdrafts were assumed to be significant in this region from the fallout of large hail. This horizontal shear vorticity induced between a curtain of rapidly descending large hail and an intense updraft is the proposed origin of rotation of the observed tornado. The possible tilting of this horizontal vorticity into the vertical, by the updraft, along with amplification through stretching is the tornadogenesis mechanism proposed and is consistent with the observations of Chapter 4. Similarly, the large hail and ice mass aloft is suggested to play an important role in the dominant production of positive CG lightning.

5.2.3 Tornado Vortex Signature

The tornado vortex signature (TVS) was examined using the RDSS software to view radar data in polar coordinate form. Two separate elevation scans at different times were chosen which best illustrate the complex nature and evolution of this storm. Figure 5.11 illustrates the best example of the TVS associated with the observed tornado. This is a PPI (plan position indicator) scan taken at an elevation angle of 9.6° at 1901 MDT. The reflectivity field (Z_h) is located on the left scan and radial velocity (V_r) is presented on the right scan. Negative (positive) magnitudes of radial velocity indicate motion toward (away from) the radar and are represented by cold (warm) colors. The low-level structure of the hail curtain contained several reflectivity "holes." Three such holes can be noticed in this PPI scan. The first one is located along the 170° radial at 11 km, the second is along the 163° radial at 10 km, and the third is located at an azimuth of 152° at a distance of 12 km.

These three distinct areas correspond exactly with small inbound/outbound radial velocity couplets (or TVS). The most pronounced TVS is located at 163° azimuth at a distance of 10 km from the CSU-CHILL radar. This feature is the closest temporally and spatially to the reported tornado southwest of Kersey, Colorado, at 1856 MDT. Rough estimates of azimuthal shear taken directly from the PPI produce very significant values in the range of 30×10^{-3} s^{-1}. A larger area of rotation (rotation is implied by adjacent areas of outbound and inbound radial velocities through symmetry) existed at this elevation angle (170° radial at 12-13 km) and is indicative of the mesocyclone.

Figure 5.12 (1907 MDT) shows that the storm had undergone substantial change in just 6 minutes. The mesocyclone (165° radial at 11 km) appeared stationary as the bulk of the reflectivity core and hail curtain translated to the east. A small hook echo was now apparent (155° radial at 9 km) and was coincident with the TVS. It is not clear if this TVS was the same feature previously located in the hail curtain and had become embedded in the larger circulation or if this was a new TVS primarily associated with the mesocyclone.

5.2.4 Azimuthal Shear

Azimuthal shear was calculated for selected radar volumes near 1900 MDT. CAPPI plots were constructed at 1.5 km and vertical cross-sections were taken through the shear feature most likely associated with the tornado. Azimuthal shear is contoured in increments of 4×10^{-3} s^{-1} starting with a value of 6×10^{-3} s^{-1}. As in the previous chapter, extreme values of shear were reduced after undergoing interpolation.

Figure 5.13 shows the situation during the first detectable stages of the TVS. A weak shear feature is located at X= -1 km and Y= -12 km and is located along the hail curtain. A more prominent feature is located to the west and is an indication of the mesocyclone of the

storm. Figure 5.14 shows a vertical slice through the TVS. These cross sections show the location relative to the hail curtain and indicate that the majority of azimuthal shear was above the surface at 1.5 km. The northern part of the azimuthal shear associated with the mesocyclone can be seen in Fig. 5.14b at X= -5 km.

At 1854 MDT (Fig. 5.15), the azimuthal shear associated with the tornado had increased slightly. This CAPPI is closest in time to the actual tornado sighting and its approximate location is labeled with a small "T." This feature is located as anticipated, at the interface of the updraft and hail-induced downdrafts. Figure 5.16a demonstrates that the TVS associated azimuthal shear had vertically elongated, was located closer toward the updraft, and was now apparent near the surface. This observation is consistent with the proposed stretching mechanism. Figure 5.16b indicates that additional and substantial azimuthal shear existed at various points along the hail curtain but were still located above the surface. The northern portion of the mesocyclone is visible at X= -2 km and does not appear to be physically linked to the TVS.

Figure 5.17 (1859 MDT) corresponds with the PPI of Fig. 5.11. The strong TVS is the dominant feature of both figures. Peak azimuthal shear values are contoured at 22×10^{-3} s^{-1} and are somewhat less than those estimated from Fig. 5.11, as anticipated from the interpolation process. The additional radial velocity couplets located along the hail curtain are also visible in Fig 5.17. The vertical-cross sections of Fig 5.18 indicate that there is no longer a physical separation of the TVS and mesocyclone. It is not clear at these temporal resolutions if the TVS rotated into the mesocyclone or if the larger circulation translated faster to the east and was overtaking the TVS.

By 1904 MDT (Fig. 5.19), the hook echo feature is apparent in the reflectivity field along with the coincident strong azimuthal shear (X= 4 km and Y= -9.5 km). The mesocyclone (X= 2 km and Y= -9 km) had intensified and its proximity to the TVS is evident in this figure but, once again, the exact evolutionary process undergone is not determinable at these temporal resolutions. The formation of a shear zone or line has become more apparent along the leading edge of the hail curtain. The vertical cross-sections shown in Fig. 5.20 indicate that the location of the TVS relative to the hail curtain is vastly different than 6 minutes earlier. Figure 5.20a indicates a vertical tilting of this shear feature with its most intense region located above the surface at 1.5 km. Although Fig. 5.19 shows that the TVS and mesocyclone are horizontally separated at 1.5 km AGL, Fig. 5.20b implies that they are vertically linked. As previously mentioned, it is not clear if this TVS was a continuation of the feature which spawned the short-lived tornado or if this was an entirely new development.

5.2.5 Three-Dimensional Histogram Analysis

Three-dimensional histograms were constructed in this case study from a moving 40 km x 40 km column following the storm motion. Since this storm differed drastically from the previous case study in positive CG lightning frequency and duration, the histogram analysis did not prove as useful for contrasting the time evolution of lightning. These histograms were also useful only up to 8 km since failure to scan the top of the storm closest to the radar would lead to a biased normalization. Figure 5.21 depicts four histograms from 1854 to 1909 MDT and are very representative of the many volumes analyzed. These histograms show a broad distribution of reflectivities with high modal values and the existence of strong reflectivities well-above the mixed-phase region similar to those found

during the strong convective development stage of cell-2 in the 23 July 1993 case study of Chapter 4.

5.3 Cloud-to-Ground Lightning Observations

The main observations of CG lightning were presented along with the storm morphology discussed in Section 5.2.1. The CG lightning detected during this storm (over 68% positive) was considered anomalous since only 3% of all CG lightning detected in the northern Rocky Mountain region is typically of positive polarity (Fuquay, 1982). Through the analyses presented in previous sections, several observations are consistent with the production of positive cloud-to-ground flashes as developed in previous studies. From the synoptic overview, both the profiler and upper-air soundings demonstrated the existence of strong upper-level wind shear that not only aided the generation of strong thunderstorms, but likely allowed an all-ice region of the storm to be displaced upshear of the main reflectivity core. The vertical cross-sections, three-dimensional surface plot, and histograms all confirmed the existence of high reflectivities suspended in the upper-level of the storm above the presumably negatively charged mixed-phase region. Assuming that these ice crystals are positively charged invoking a normal polarity charge dipole process (Williams, 1989), this would create the "tilted-dipole" hypothesized by MacGorman and Burgess (1994) in their study of dominant positive CG lightning-producing tornadic storms. This tilted-dipole would allow the positively charged ice aloft to effectively "see" the ground providing a path for discharge. Complicating this issue are the interactions between the negatively charged region and this upper positive region and associated intracloud (IC) lightning. It is presumed that the low negative CG flash rates are indicative of high IC lightning activity and that any positive flashes are generated from the unneutralized ice located downshear of the main echo

core. During an investigation of this same storm system, Carey and Rutledge (1996b) did show high IC rates during at least one phase of this storm as it moved within range of a mobile flat plate antenna. They also discovered negative values of K_{dp} above and adjacent to the glaciated tops of the tilted precipitation echoes during the period of highest positive CG flash rate (1943 to 1958 MDT). These negative K_{dp} values would be indicative of ice crystals vertically orientated in a strong electric field (Metcalf, 1995).

One common factor in both case studies between the hypothesized tornado formation mechanisms and the production of abnormally high positive CG lightning was the existence of a strong updraft. A strong updraft provides the necessary lifting required to generate and suspend large charged regions higher in the tropopause compared to weaker updrafts. These higher-than-normal charged regions are hypothesized to be generating high IC flash rates (at a time when negative CG flashes are very infrequent). Furthermore, the strong environmental shear aloft allows the upper positive region to be horizontally displaced from the main storm core, thereby promoting positive ground flashes. It is also speculated that the low negative CG flash rates are a consequence of the large mass of the mixed-phase region. These storms appear to have such high precipitation rates that the negatively charged region effectively "rains-out" before adequate electric potential can be built between it and the earth's surface. This would also leave the lighter positively-charged crystals suspended aloft without any IC discharge mechanisms, thus allowing a higher probability of ground discharge. It is most likely, as with most physical phenomena, that several of these key factors contribute to the generation of dominant positive CG lightning.

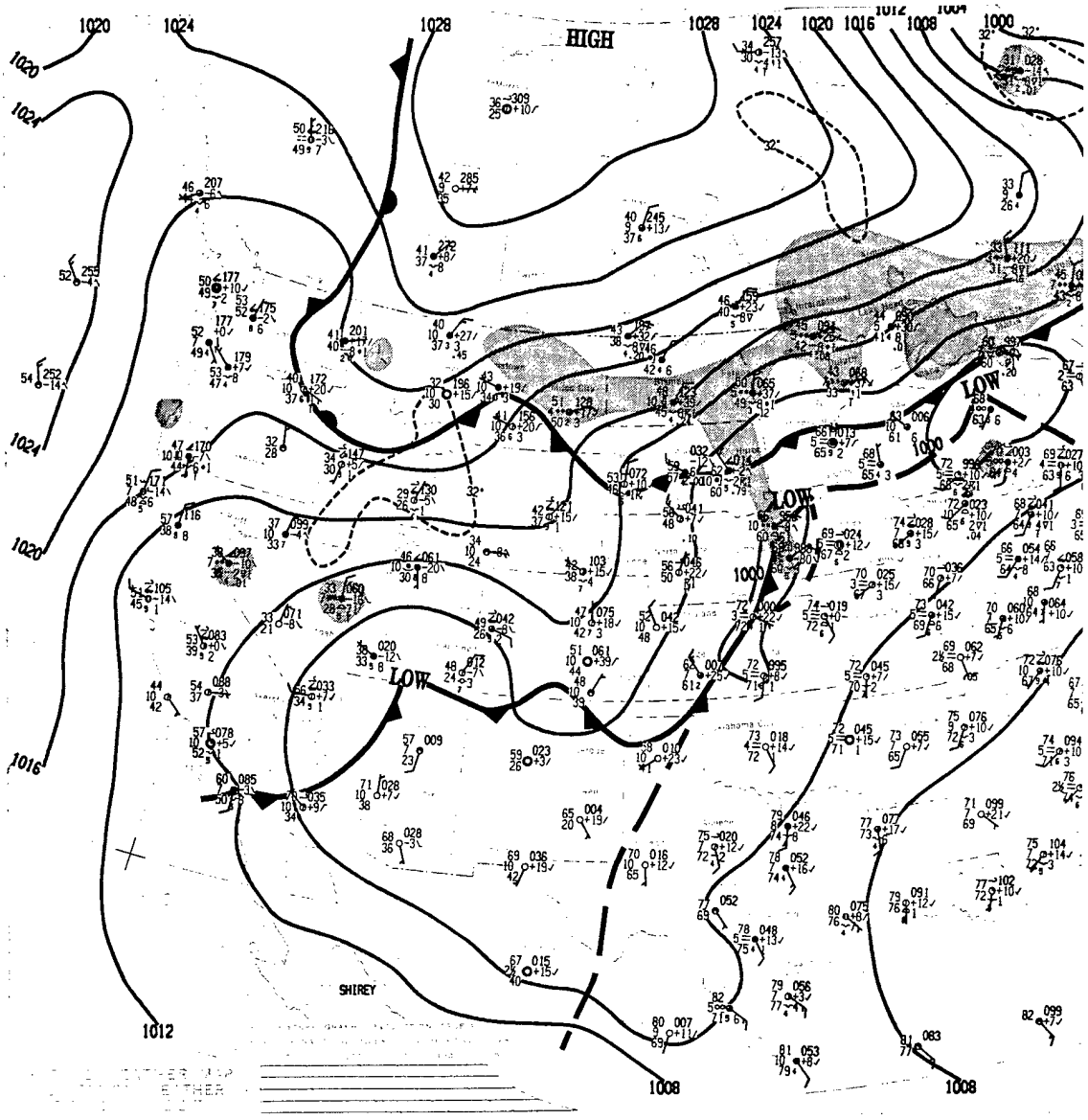

Fig. 5.1 Surface weather chart with frontal analysis of western United States on 7 June 1995 at 0600 MDT. Areas of precipitation are indicated by shading.

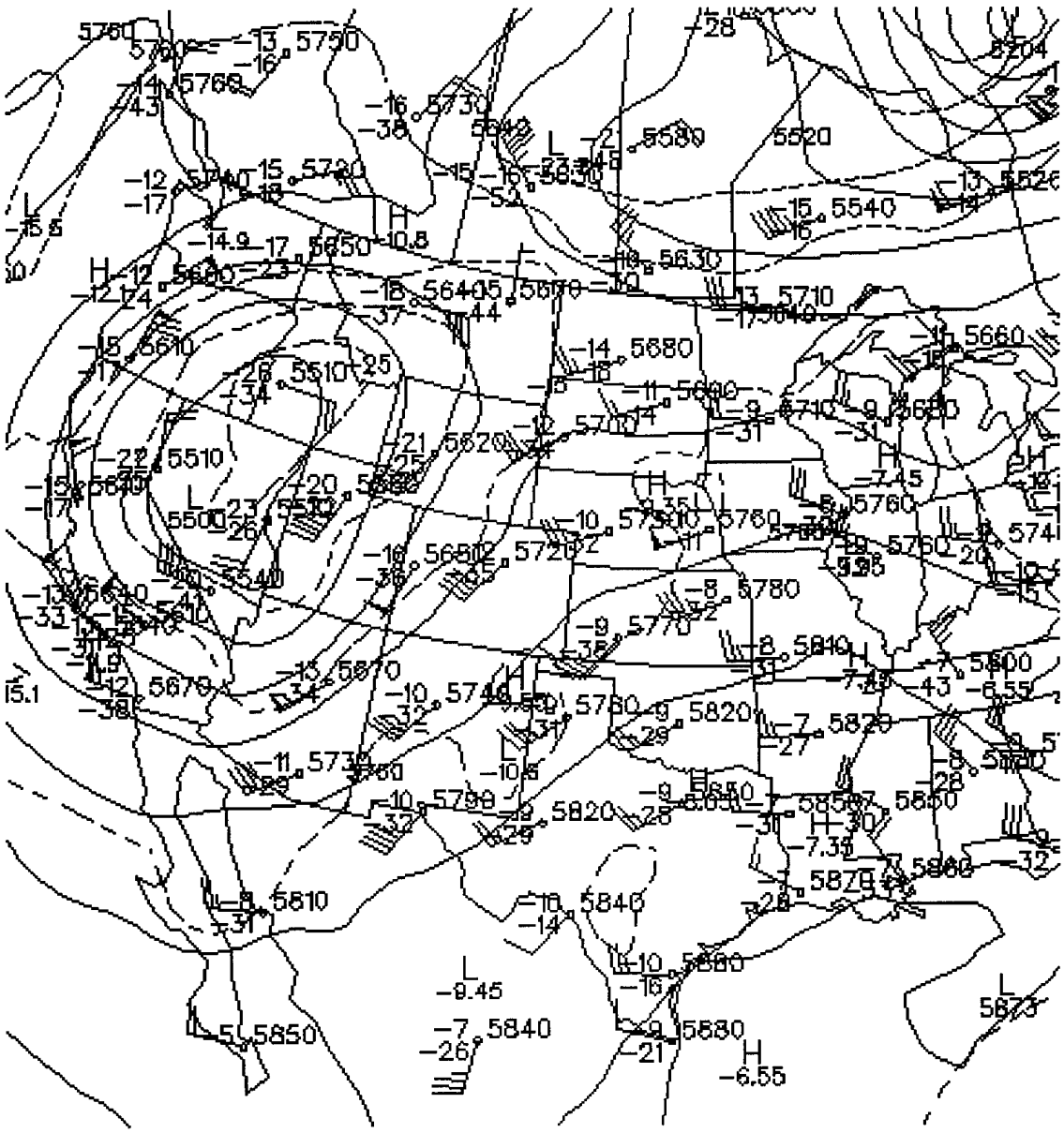

Fig. 5.2 500 mb height analysis of western United States on 7 June 1995 at 0600 MDT.

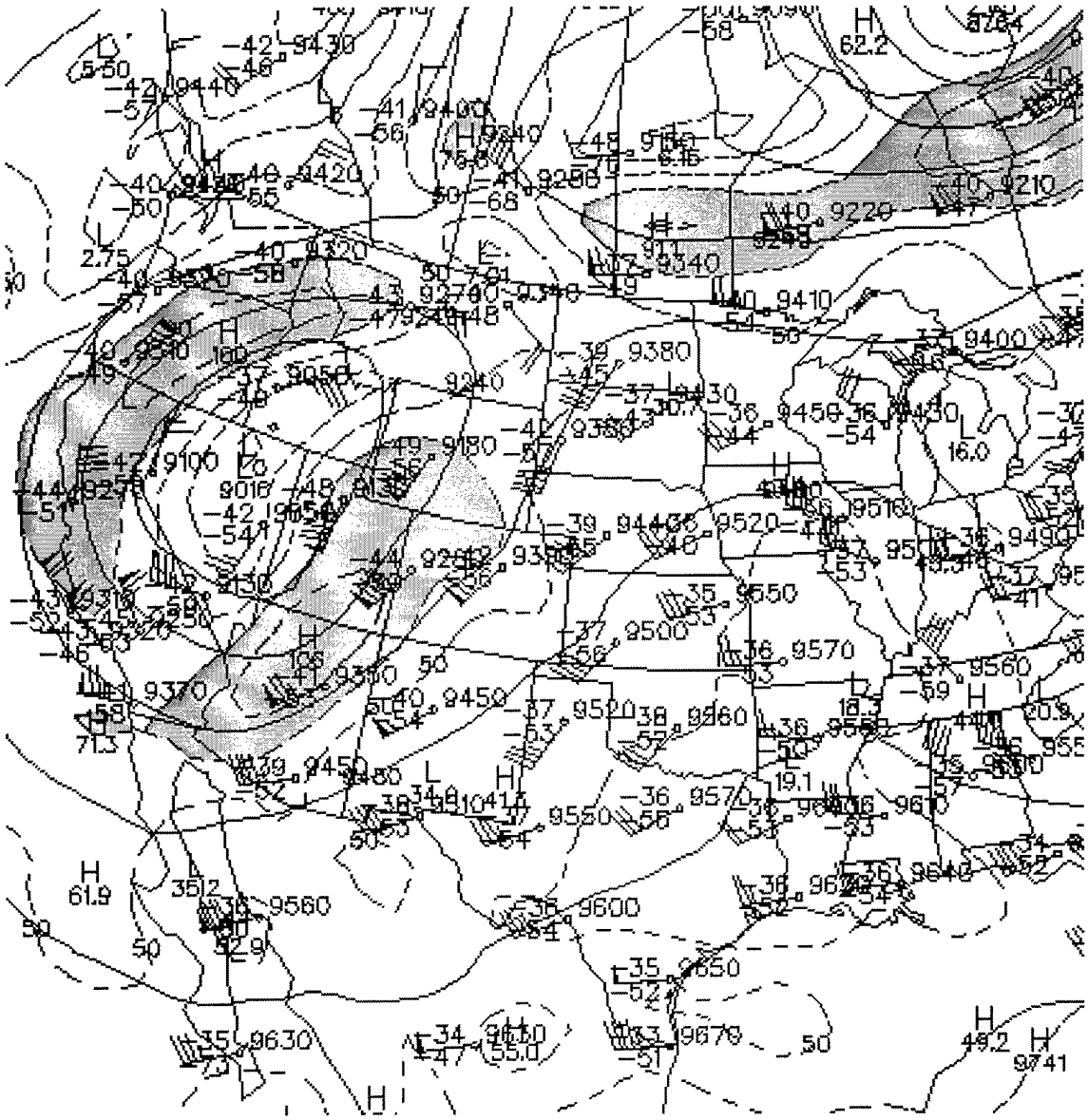

Fig. 5.3 300 mb height analysis of western United States on 7 June 1995 at 0600 MDT.

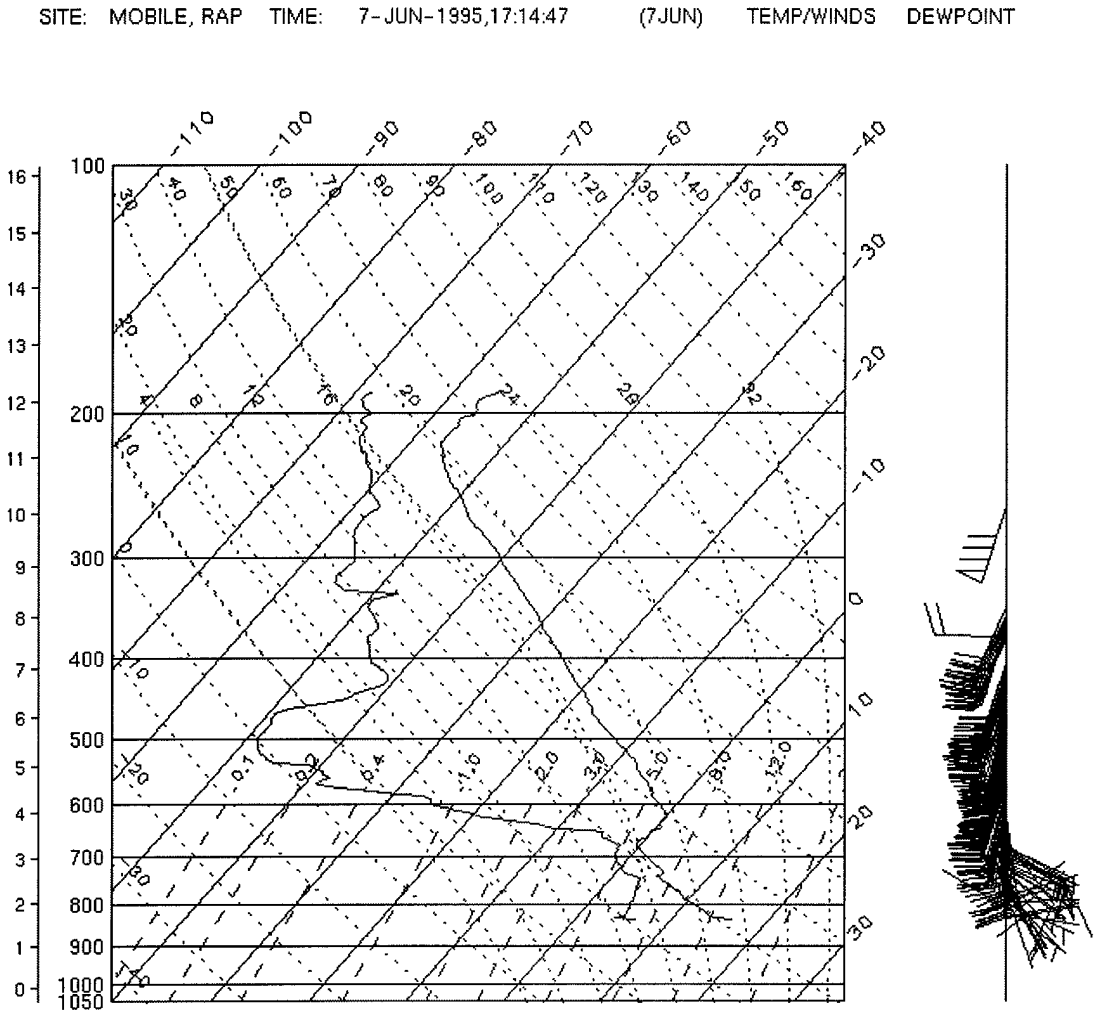

Fig. 5.4 Skew T - Log P plot of upper air sounding data taken by an NCAR mobile sounding facility in northeastern Colorado on 7 June 1995 at 1714 MDT. Wind barbs are in m s^{-1} and temperature is in °C.

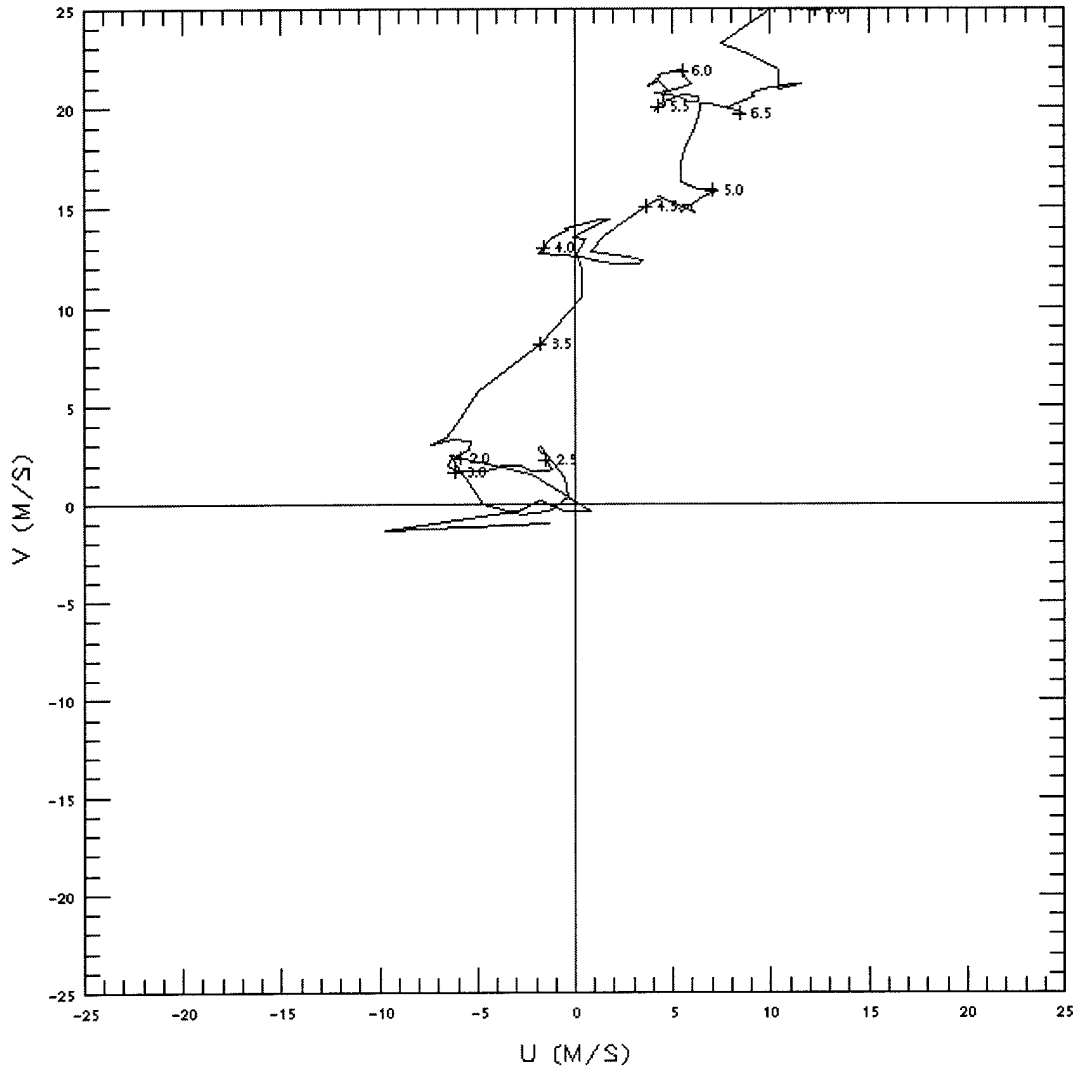

Fig. 5.5 Hodograph of lowest 8 km (MSL) of 1714 MDT NCAR sounding on 7 June 1995. Points are labeled at 500 m intervals.

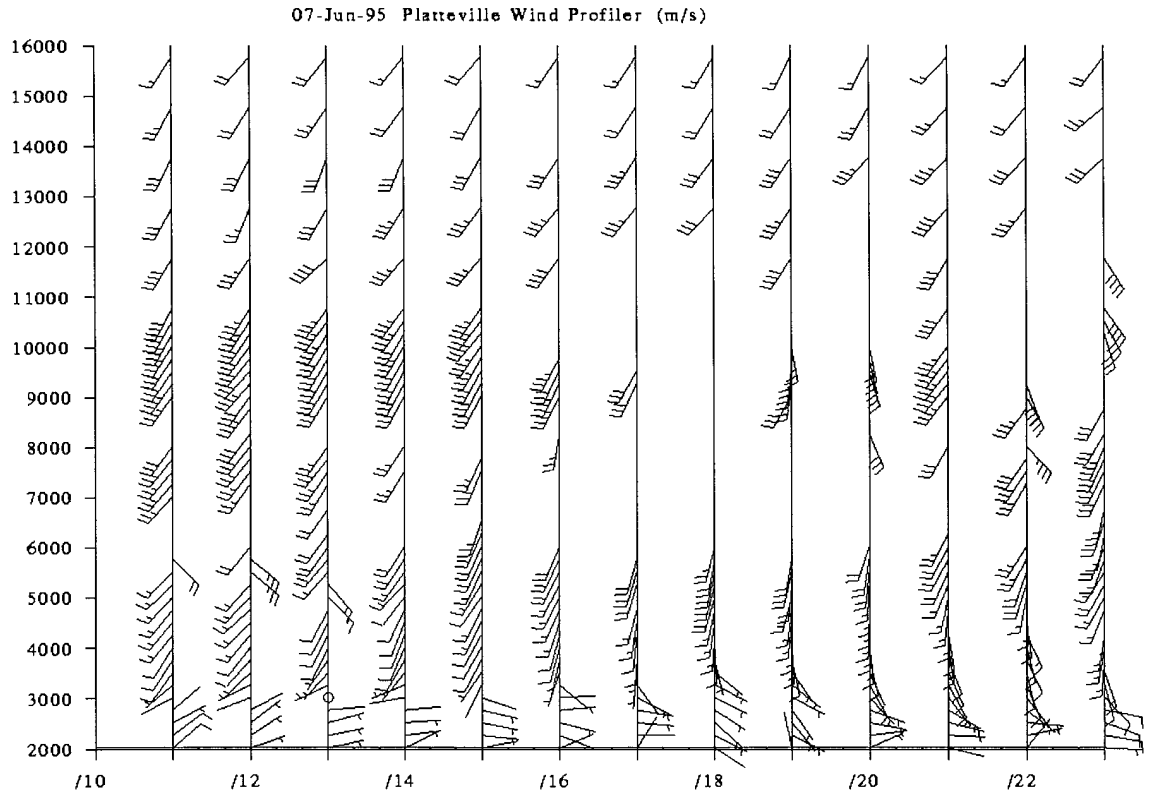

Fig. 5.6 Platteville, Colorado, wind profiler horizontal winds on 7 June 1995 from 1000 to 2300 MDT.

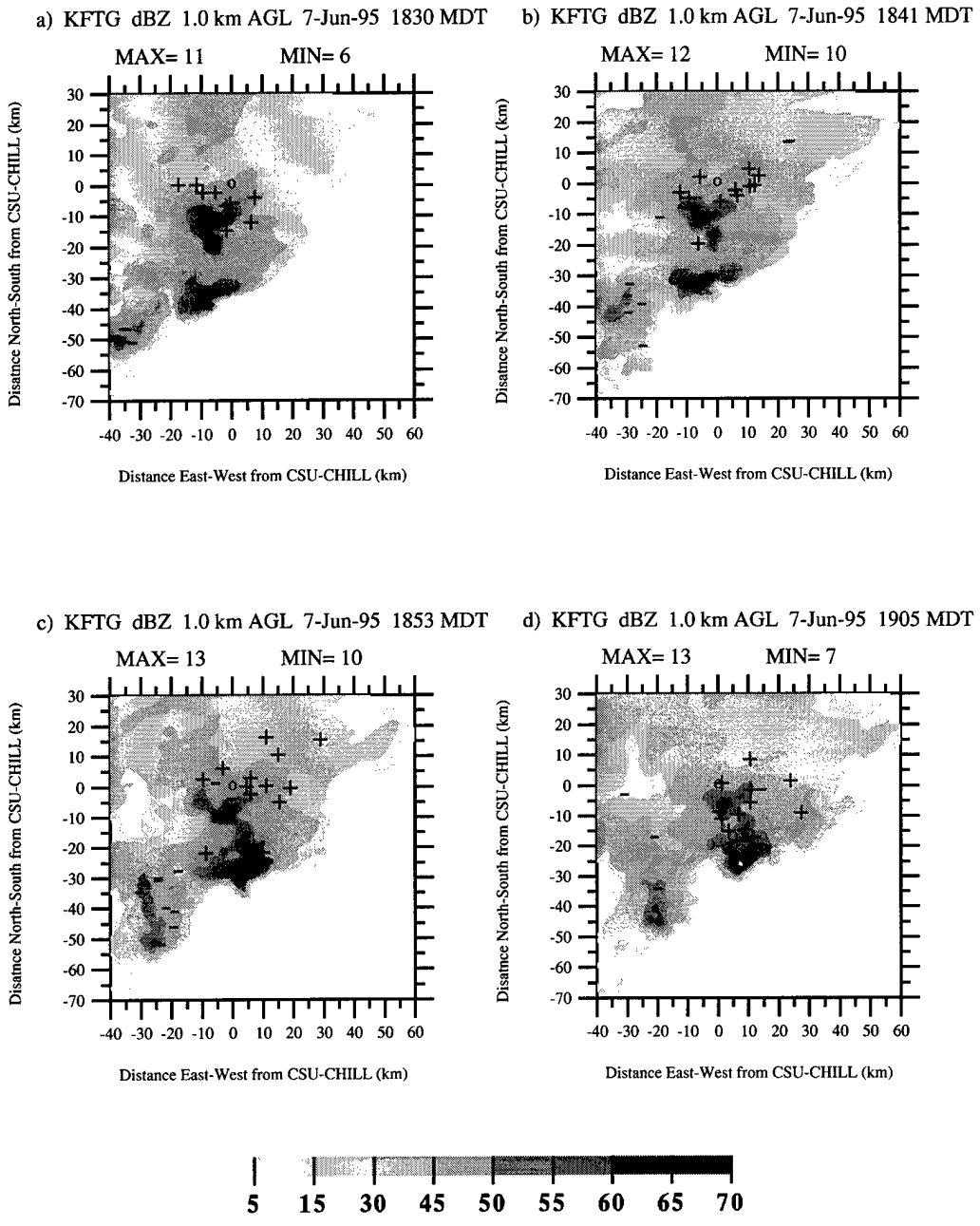

Fig. 7.5 1.0 km (AGL) CAPPIs of reflectivity. CG flash locations and polarity are shown. MAX and MIN values correspond to the total number of positive and negative flashes respectively. Areas with reflectivities >70 dBZ are not shaded. (a) 1830 MDT, (b) 1841 MDT, (c) 1853 MDT, (d) 1905 MDT.

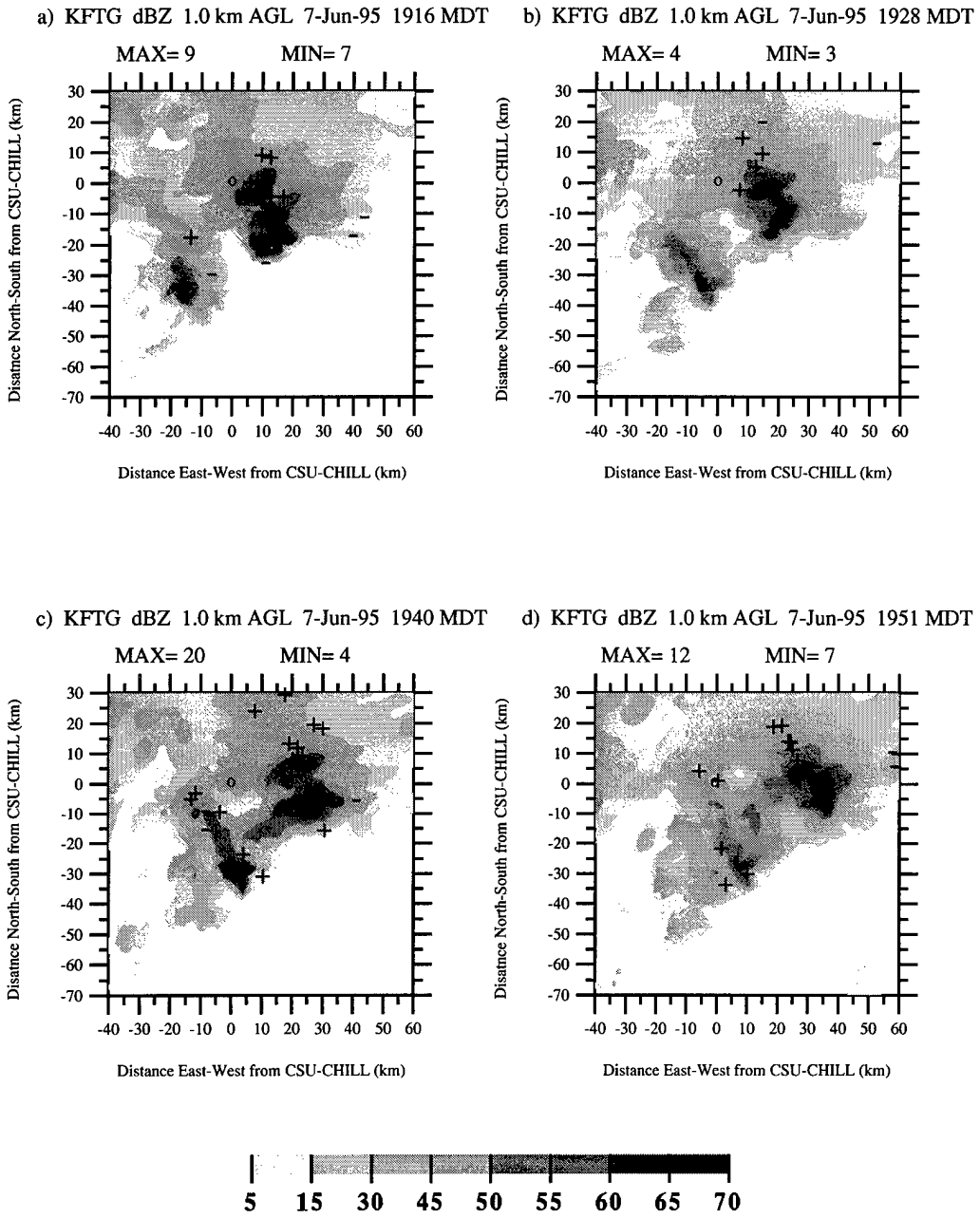

Fig 5.8 As in Fig. 5.7. (a) 1916 MDT, (b) 1928 MDT, (c) 1940 MDT, (d) 1951 MDT.

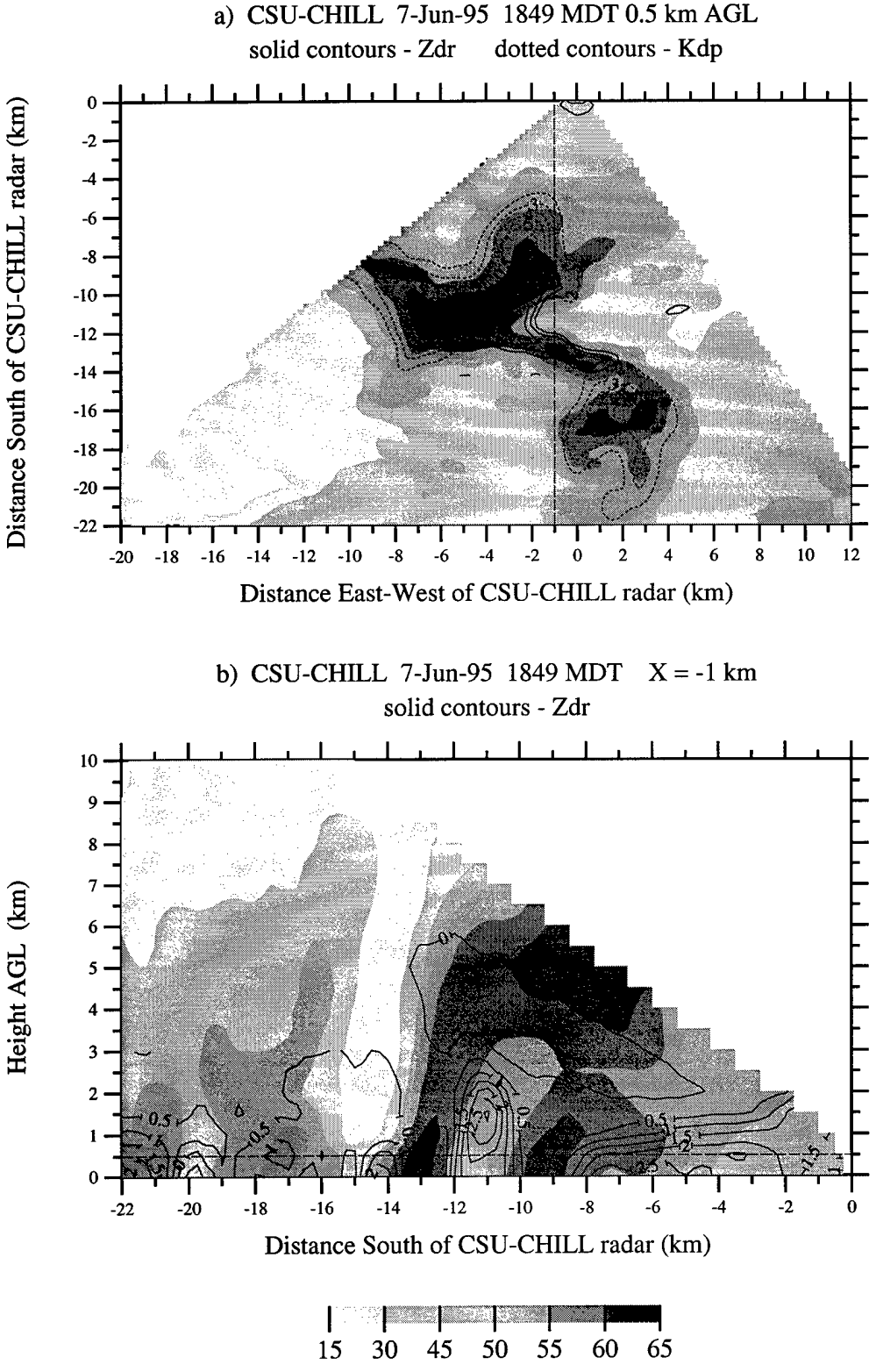

Fig. 5.9 CSU-CHILL radar reflectivity (shaded) and multiparameter fields (contoured) on 7 June 1995 at 1849 MDT. (a) 0.5 km CAPPI with solid contours of differential reflectivity-Z_{dr} [dB] and dotted contours of specific differential phase-K_{dp} [° km^{-1}], (b) vertical cross-section at X= -1 km with contours of Z_{dr}.

Fig. 5.10 Three-dimensional view of the 55 dBZ reflectivity surface observed by the CSU-CHILL radar on 7 June 1995 at 1849 MDT. This thunderstorm is located south of the radar and the viewer's location is from the east-southeast.

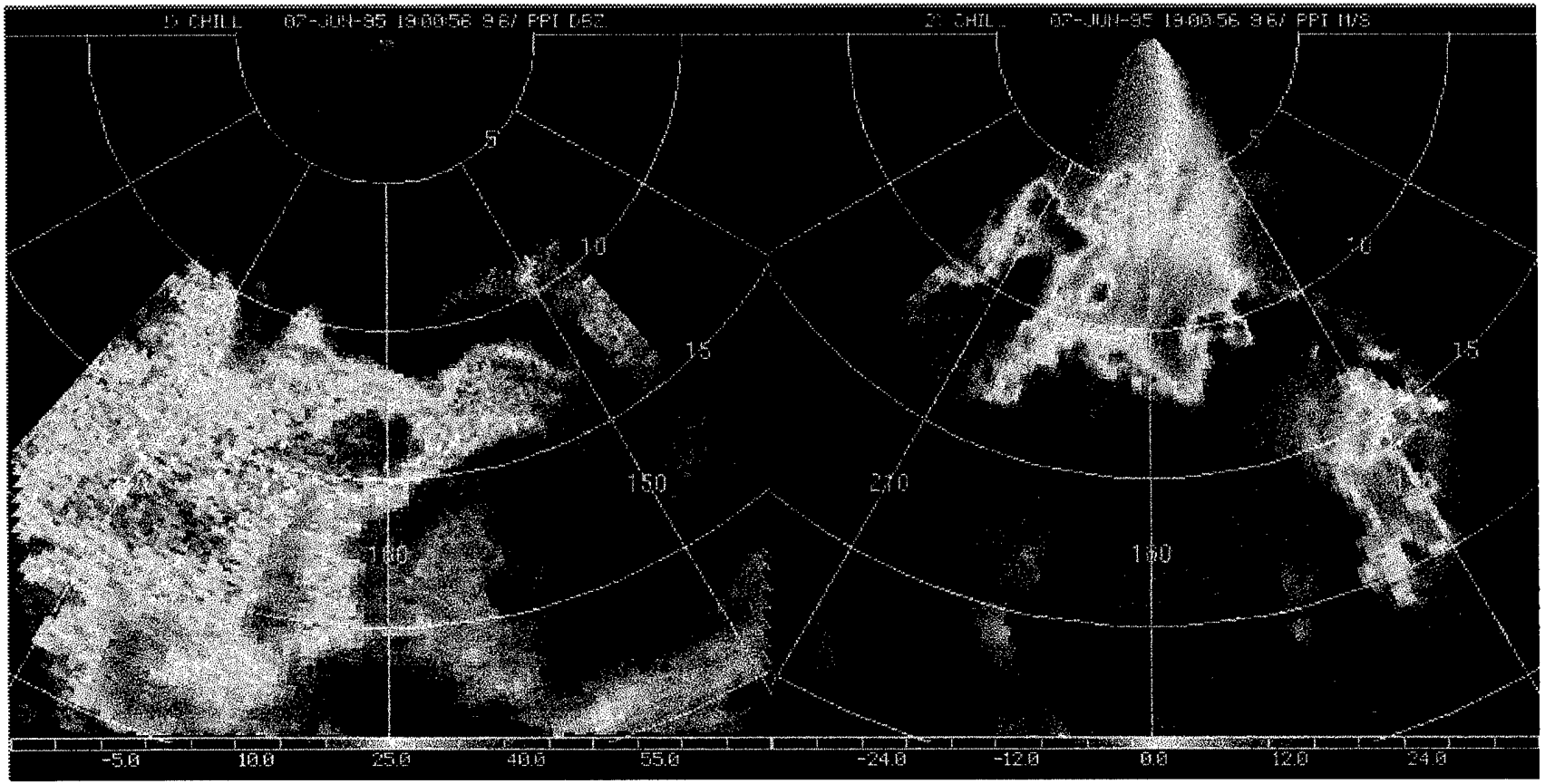

Fig. 5.11 Elevation scan of 9.6° from the CSU-CHILL radar on 7 June 1995 at 1900 MDT. Left: Reflectivity. Right: radial velocity. The color scale for the magnitudes is shown at the bottom. Standard convention is used for radial velocity where negative (cool tones) indicate motion toward the radar and positive values (warm tones) indicate motion away. Range rings are every 5 km.

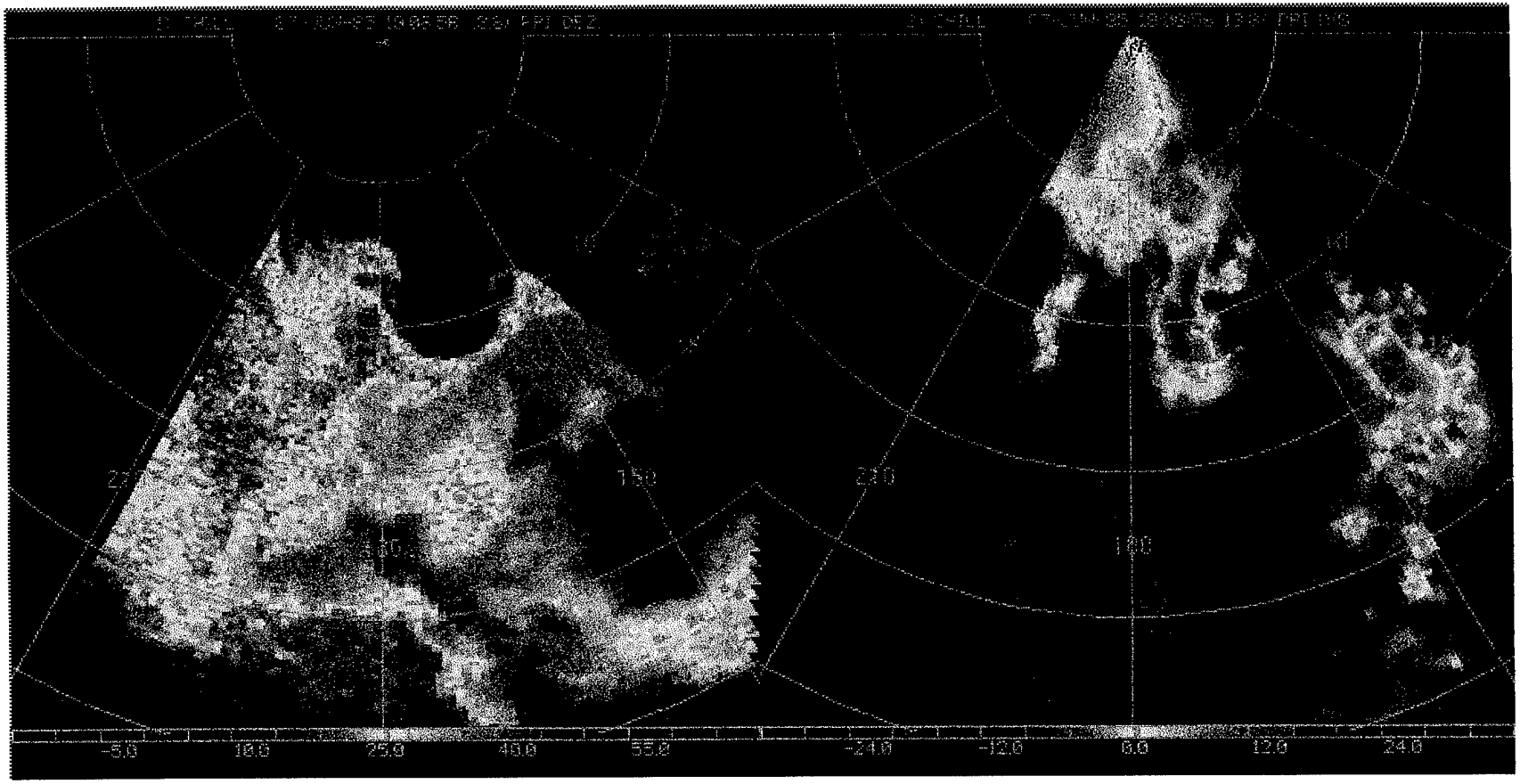

Fig. 5.12 As in Fig. 5.11 except for an elevation scan of 13.8° at 1906 MDT.

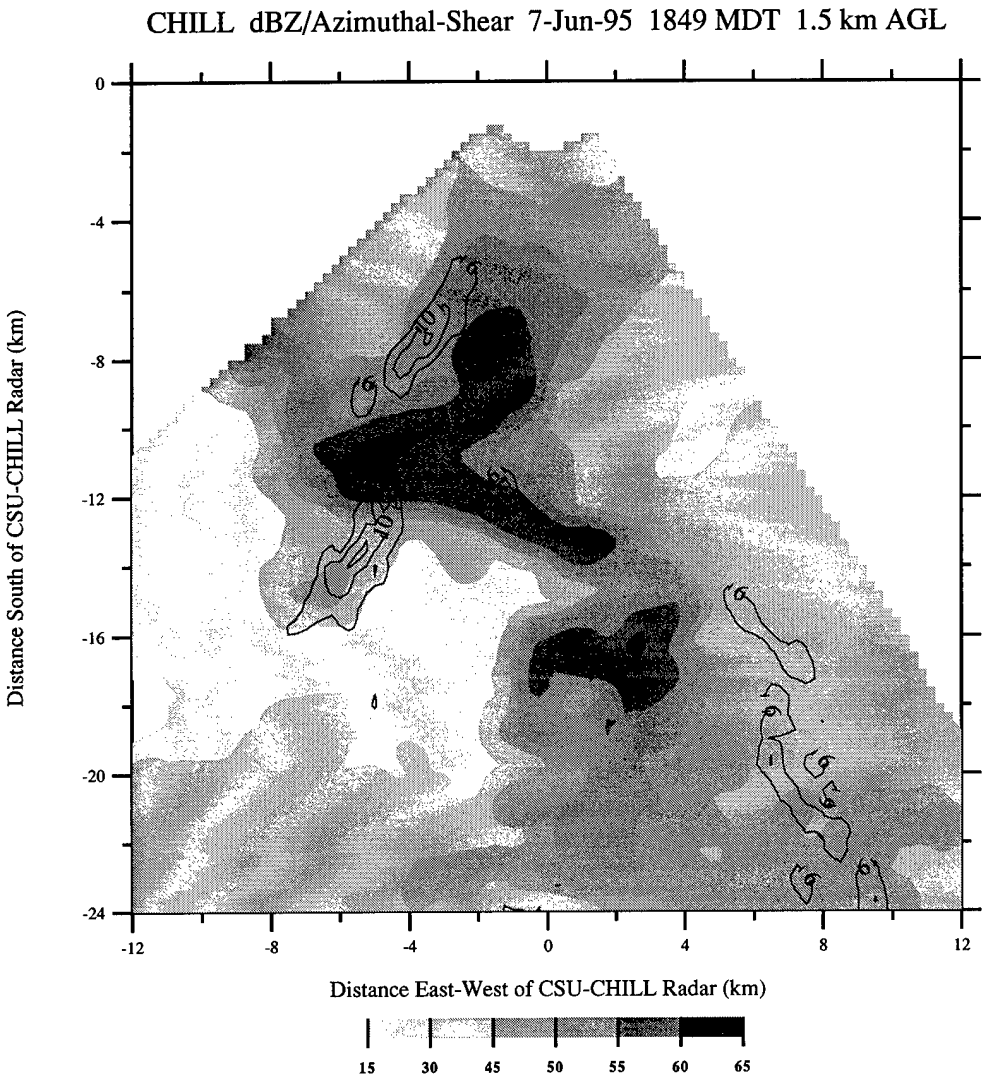

Fig. 5.13 1849 MDT 1.5 km CAPPI of CSU-CHILL reflectivity (shaded) and azimuthal shear (contours). Azimuthal shear is contoured every 4 x 10^{-3} s^{-1} starting at 6 x 10^{-3} s^{-1}.

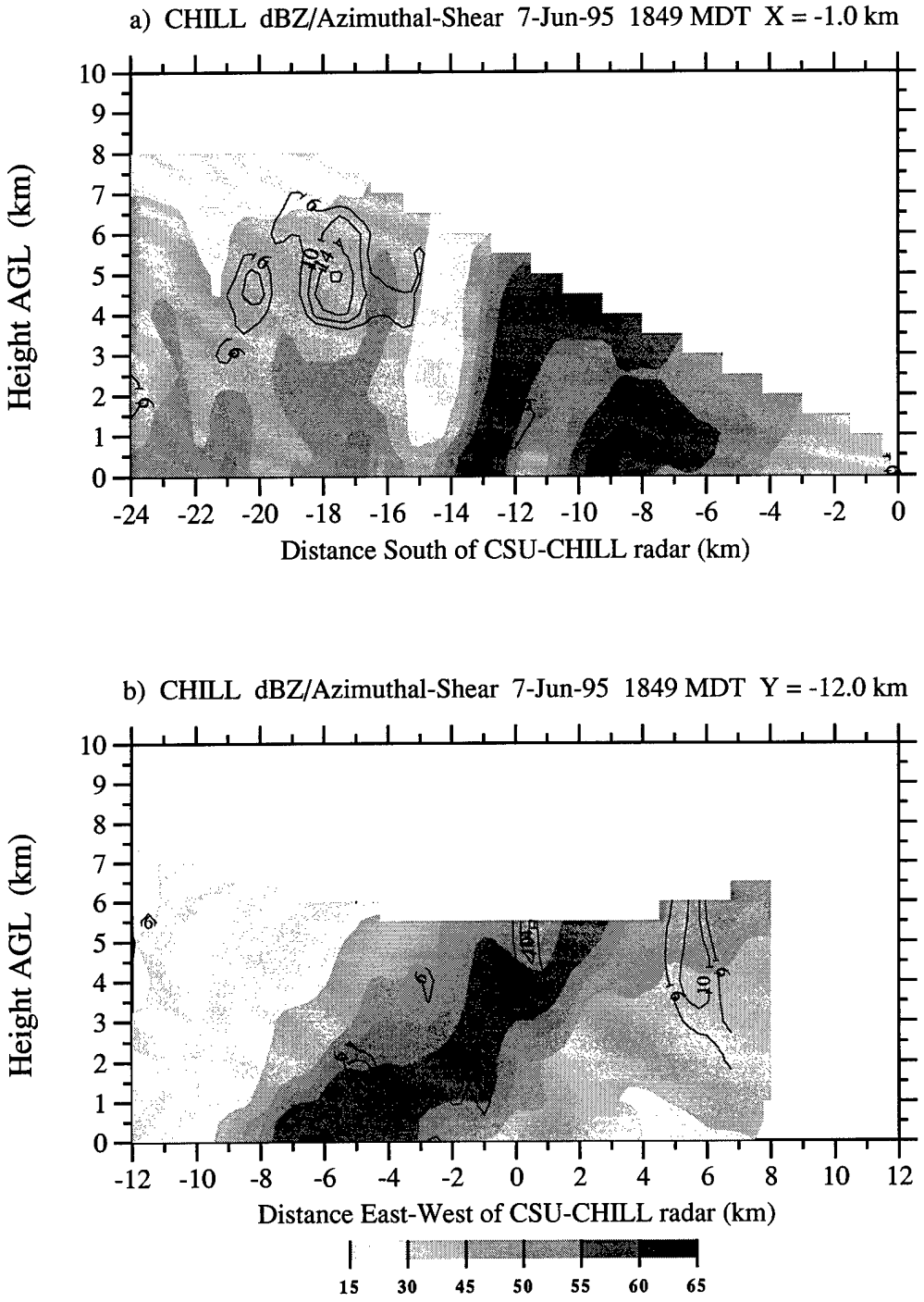

Fig. 5.14 As in Fig. 5.13 except for 1849 MDT vertical cross-sections. (a) X= -1.0 km, (b) Y= -12.0 km.

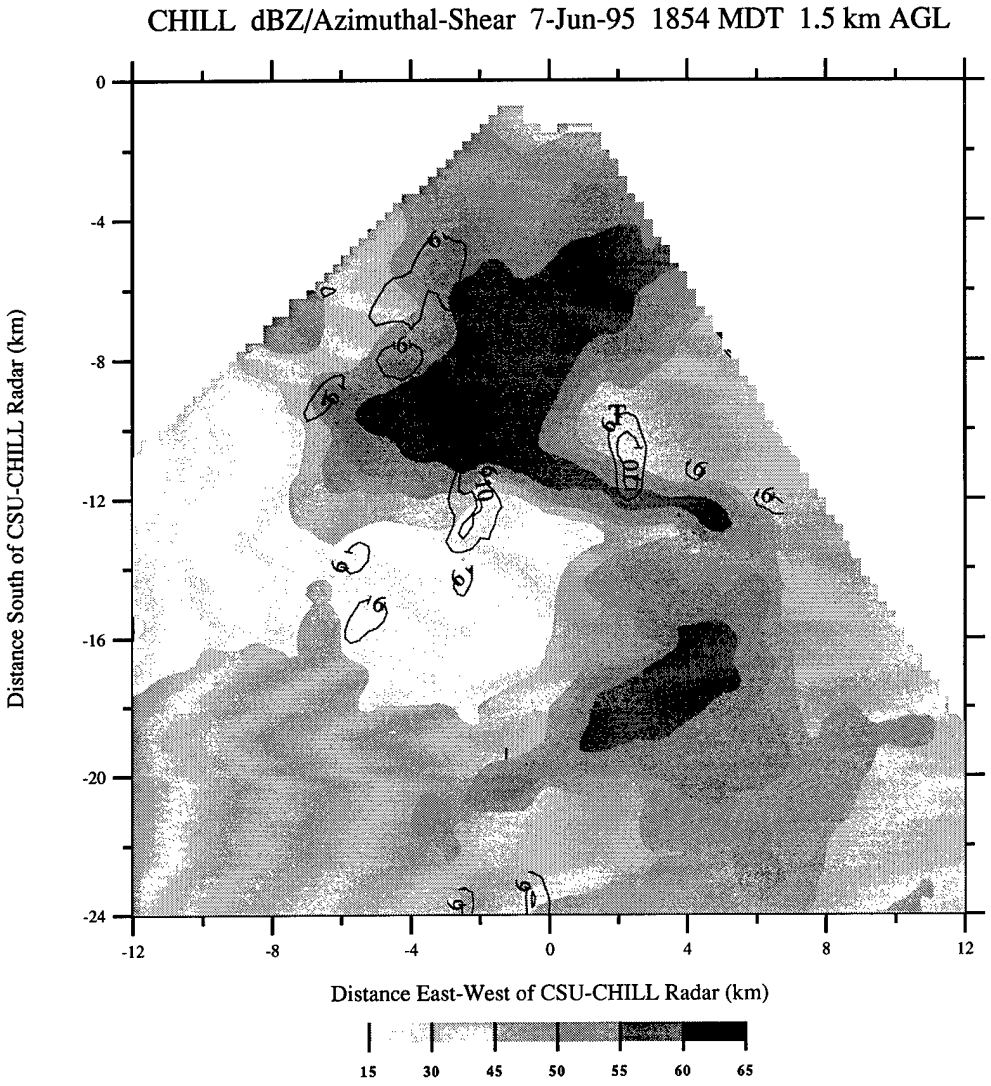

Fig. 5.15 As in Fig. 5.13 except for 1854 MDT. Approximate location of observed tornado is indicated by "T."

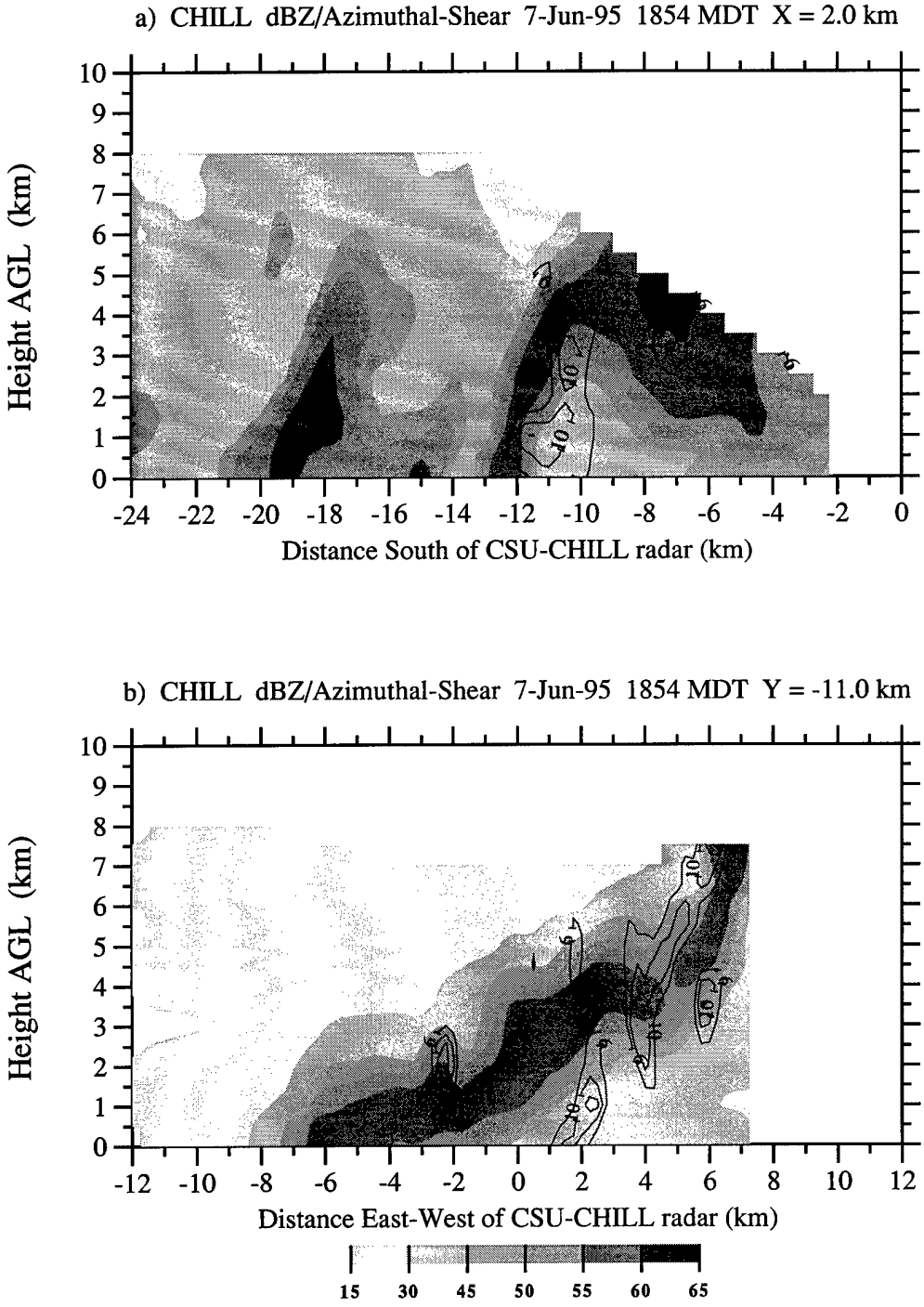

Fig. 5.16 As in Fig. 5.13 except for 1854 MDT vertical cross-sections. (a) X= 2.0 km, (b) Y= -11.0 km.

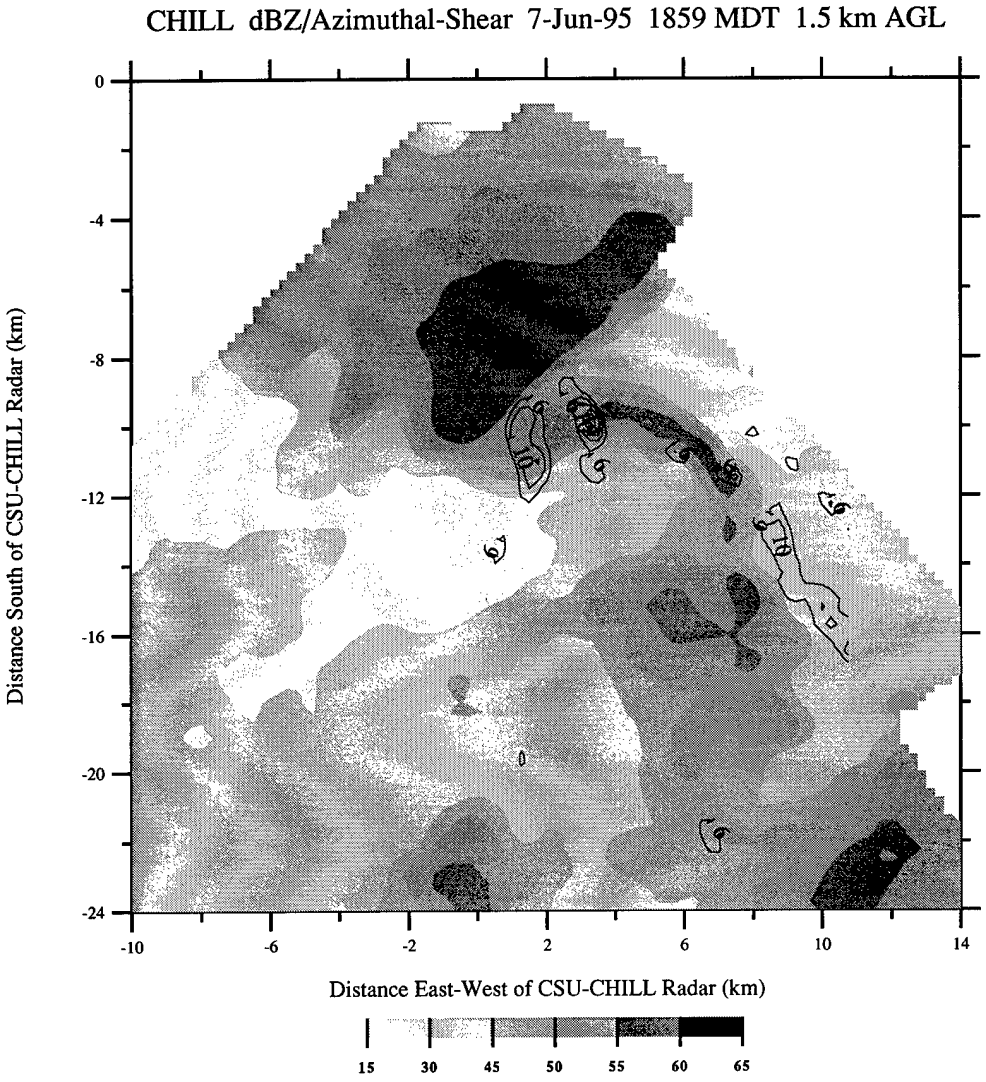

Fig. 5.17 As in Fig. 5.13 except for 1859 MDT.

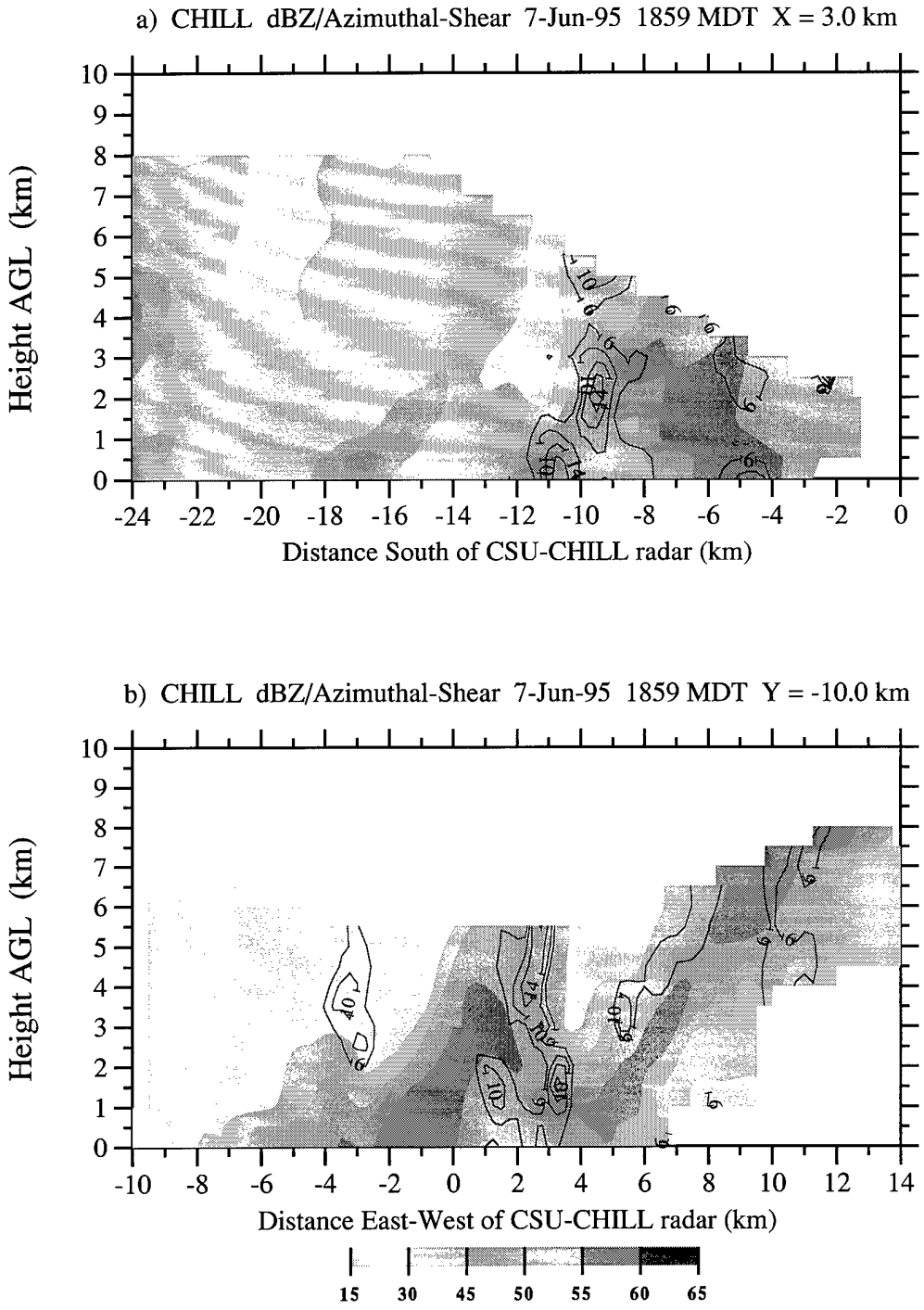

Fig. 5.18 As in Fig. 5.13 except for 1859 MDT vertical cross-sections. (a) X= 3.0 km, (b) Y= -10.0 km.

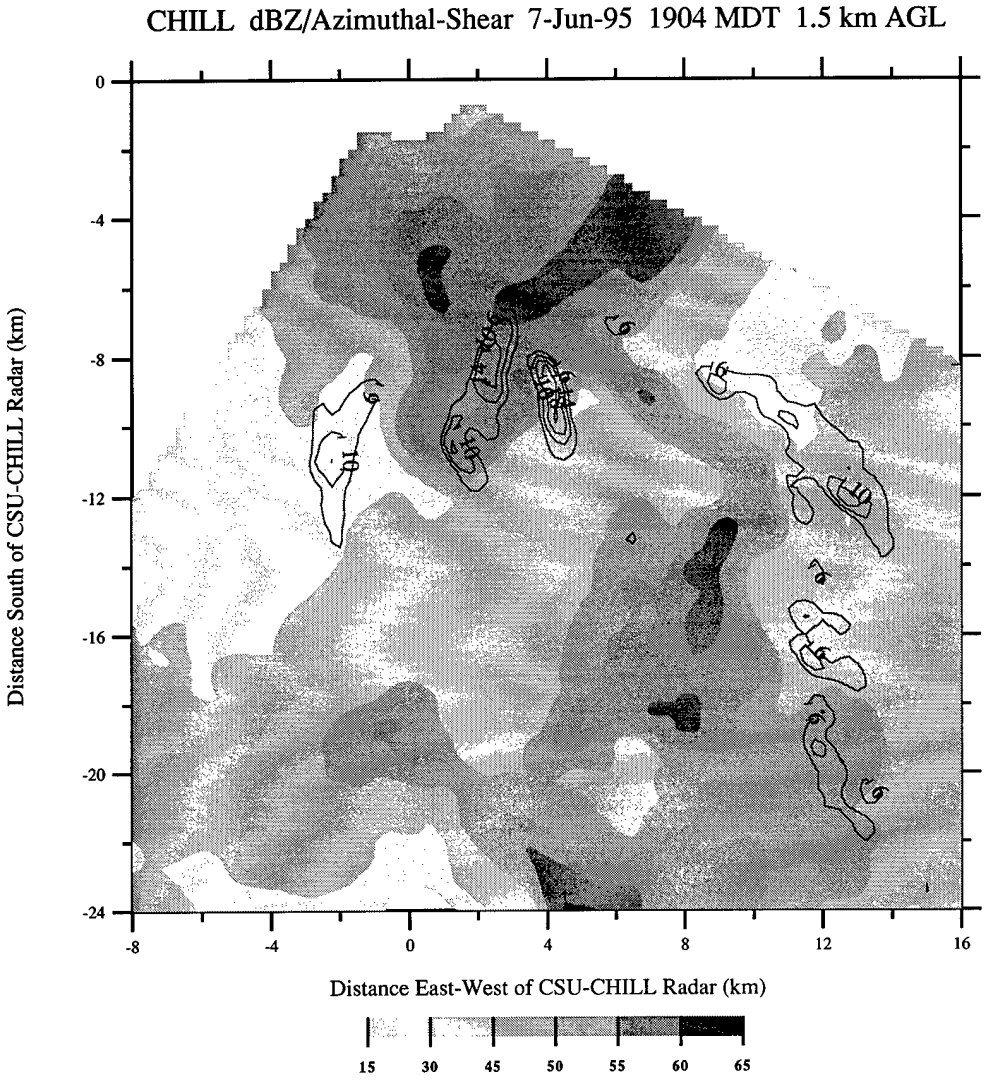

Fig. 5.19 As in Fig. 5.13 except for 1904 MDT.

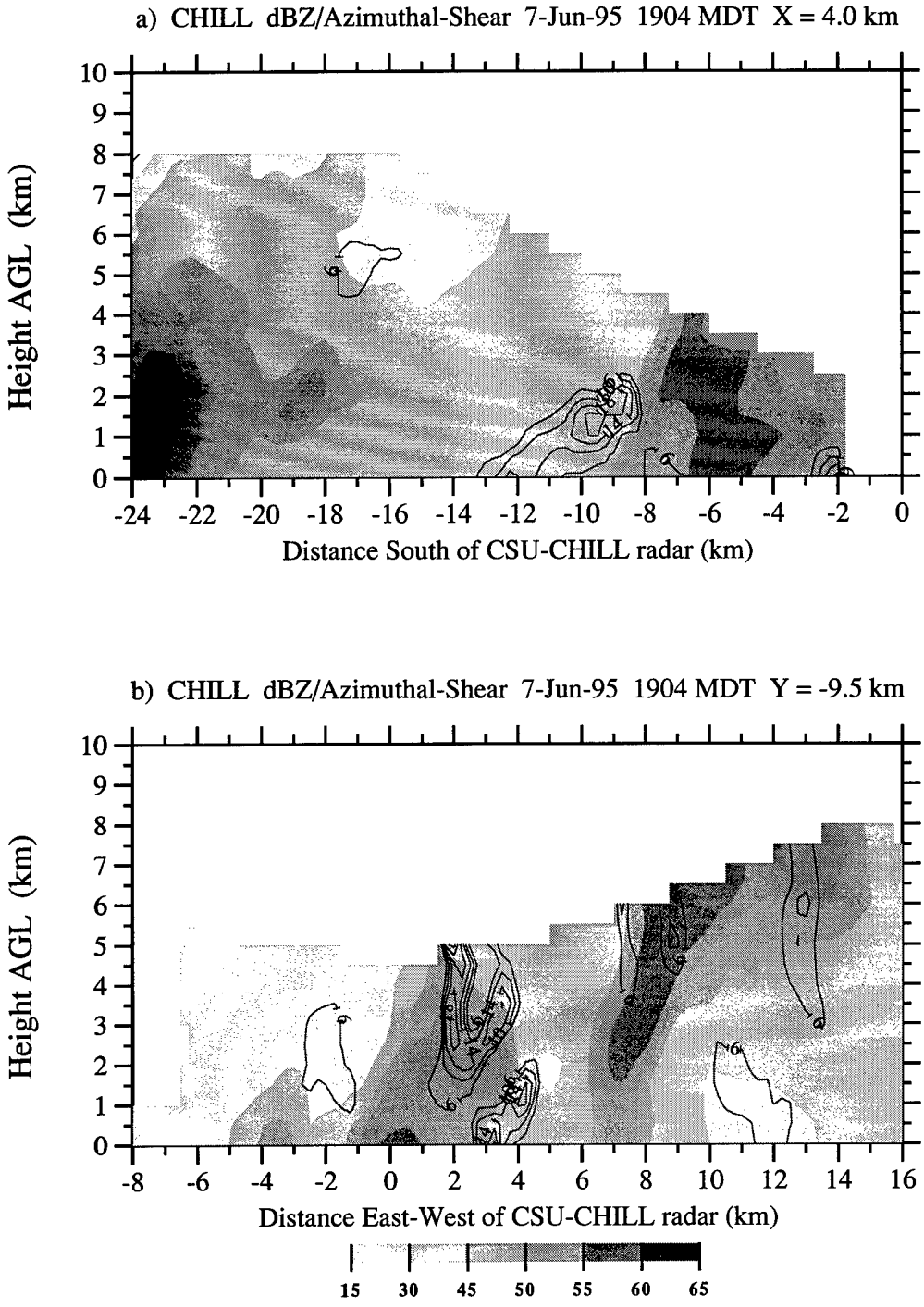

Fig. 5.20 As in Fig. 5.13 except for 1904 MDT vertical cross-sections. (a) X= 4.0 km, (b) Y= -9.5 km.

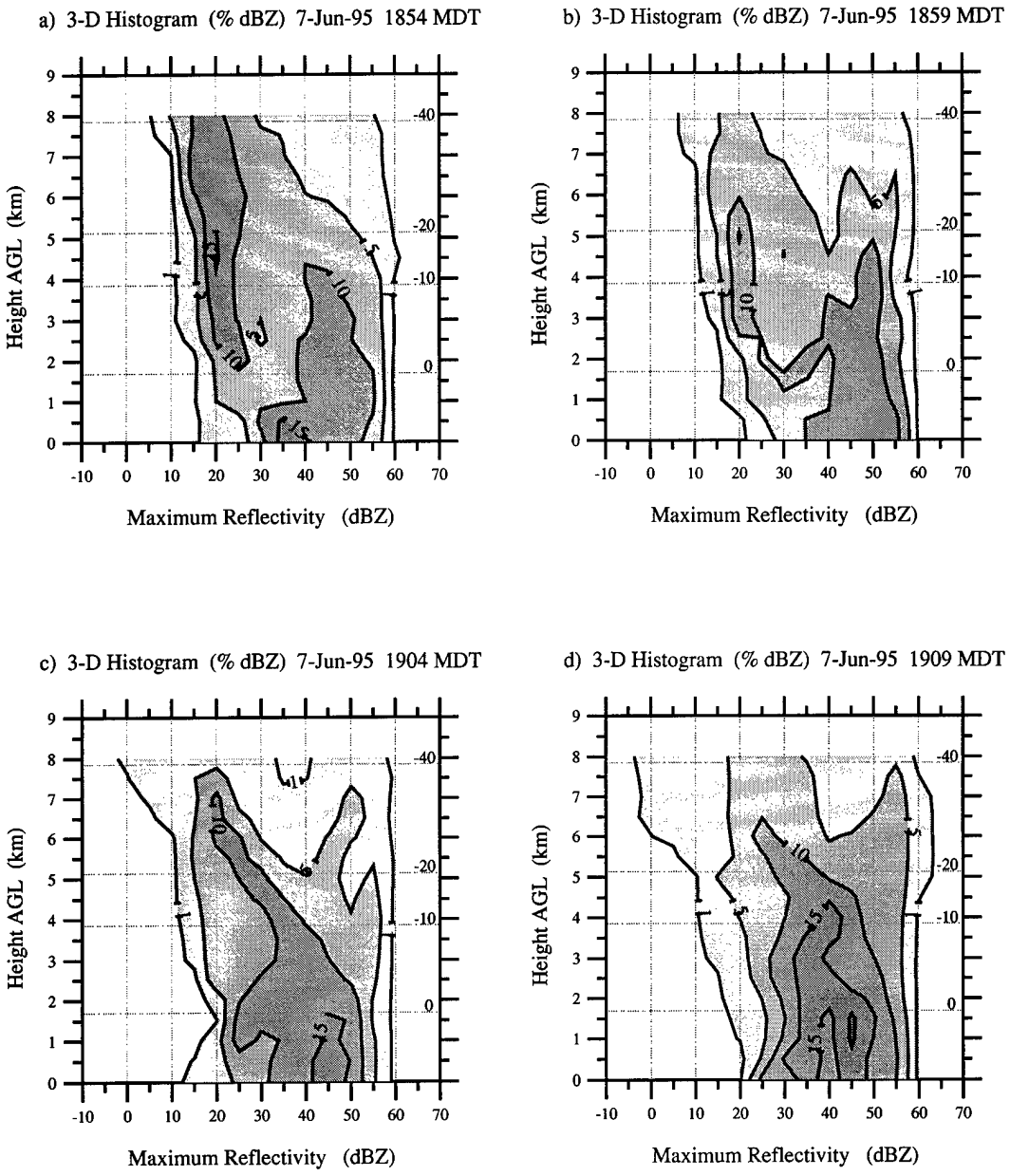

Fig. 5.21 Three-dimensional histograms (CFADs) of radar reflectivity from 7 June 1995. Contours are percent frequency of occurrence of reflectivity at a given height. Data contour interval is 5% starting at 5%. A 1% contour is included to show distribution outliers. Horizontal dashed lines denote NCAR 1774 MDT sounding temperatures (°C). (a) 1854 MDT, (b) 1859 MDT, (c) 1904 MDT, (d) 1909 MDT.

CHAPTER 6

DISCUSSION AND CONCLUSIONS

The goal of this study was to examine the kinematic, microphysical, and electrical characteristics of two multi-cell thunderstorms which occurred in northeastern Colorado. The synoptic situation in which these thunderstorms developed was similar to those described by Doswell (1980) in his investigation of typical High Plains severe thunderstorm events. These particular thunderstorms were chosen for this thesis because both produced weak short-lived tornadoes and cloud-to-ground (CG) lightning dominated by positive flashes. Through various radar analysis methods, an effort was made to infer the origins of rotation, tornado formation mechanism, and storm structure responsible for the observed CG lightning pattern. Radar data was obtained from the CSU-CHILL and NCAR Mile High radars and CG lightning flashes were recorded by the National Lightning Detection Network. Both single- and dual-Doppler radar methods were employed. Single-Doppler techniques included polarization-diverse measurements, the calculation of azimuthal shear, histogram analyses, the investigation of constant altitude and vertical cross-section displays, and the examination of the raw reflectivity and radial velocity fields. Dual-Doppler analyses were primarily used to determine vertical motions.

6.1 Observations and Comparisons Between Case Studies

The thunderstorm of 23 July 1993, investigated in the first case study, contained a cell that initially produced moderate rates of negative CG lightning and then ceased CG

activity as the cell underwent rapid intensification as evident by the three-dimensional histogram analysis. Once this cell reached its mature phase, downdrafts ensued, the manifestation of heavy precipitation and descending hail evaporatively cooled its environment, and a storm outflow boundary was created. This cell then produced its final three CG flashes concurrent with the development of the downdrafts. These flashes were all of positive polarity and were hypothesized to have originated from a positively charged region consisting of ice crystals in the upper-levels of the storm. The presence of positively charged ice crystals at low temperatures is consistent with the laboratory results of Takahashi (1978).

This research revealed that large radar reflectivities existed high in the storm above the -40°C level where a homogeneous mixture of ice crystals must exist. Furthermore, these positive flashes discharged to the surface, upshear of the main reflectivity core, where one would expect to find cirrus anvil clouds known to be composed of all ice. This configuration of an upper-level positively charged region, horizontally displaced from the negatively charged mixed-phase region, has been previously labeled a "tilted-dipole" by MacGorman and Burgess (1994).

It was presumed that frequent intracloud discharges were occurring between the main negative and positive charge regions, once the initial negative CG phase terminated, since charge separation mechanisms in the updraft would continue to generate sufficient storm electrification. This assumption would explain the complete absence of negative CG flashes once the strong updrafts developed and suspended a large negatively charged mass higher in the storm and closer to the upper positively-charged ice region. Intense updrafts would magnify the electric field between these two regions (by placing the charge centers closer

together higher in the storm) and increase the probability of reaching breakdown potential. It was noted that once this cell began its dissipation phase, it did so rapidly, while leaving much of the less dense ice mass suspended aloft. This rapid descent of precipitation and hail, presumably negatively charged, would create a large vertical expansion of the mixed-phase region and consequently lower the negative charge density, perhaps below breakdown potential. This event could explain the lack of negative CG flash regeneration as the negatively charged region approached closer to the Earth's surface. Therefore, it is hypothesized that the positive flashes dominated the CG activity because of a combination of the tilted-dipole effect and the descent and decreasing charge density of the negative mixed-phase region.

The intense updraft which allowed the above lightning episode to transpire created a situation favorable for the generation of strong and rapid downdrafts. This downward moving cold pool generated an outflow boundary at the surface indicated by the propagation of a radar-identified gust front. Enhanced horizontal vorticity was generated along this boundary which may have been tilted into the vertical. However, a precise tilting mechanism was not evident in this analysis. Once the region of enhanced low-level vorticity became coincident with a strong updraft, vortex stretching could explain the rapid intensification to tornadic magnitudes.

The second case study of 7 June 1995 exhibited similar characteristics to the 1993 case. This multi-cell storm also produced dominant positive CG lightning and a weak short-lived tornado. Although a similar mechanism will be argued to explain the formation of the tornado and positive CG flashes, significant differences did exist between the two cases. The thunderstorm of 7 June 1995 was longer-lived and perhaps more violent than the previous

case judging by the frequency of reported tornadoes and large hail and sustained large positive CG flash rates. A most unique feature of this thunderstorm was the presence of a vertical hail "curtain" extending from the upper-levels of the storm to the surface. Multiparameter radar observables indicated that little or no rain was present in this region as compared to the main echo core. The examination of only low- to mid-level radar scans would not have revealed this particular feature. The true physical structure of this storm was more clearly decipherable after the generation of a constant reflectivity three-dimensional surface plot. By visualizing this three-dimensional surface, the extent of the large suspended hail region was realized. It was concluded that the formation of this reflectivity feature resulted from the inability of the updraft to sustain such a large ice mass aloft. The resulting curtain of hail rapidly descended along the southern periphery of the updraft core.

Common to the generation of high positive CG flash rates with little or no negative CG lightning was the upper-level environmental shear, the vertical displacement of high reflectivity regions, a large ice mass present aloft, and an intense updraft. Although the growth and decay stages were not analyzed, the similarity between these two cases was evident during the mature phases of the storms. Additional evidence, pointing to the origin of the positive CG flashes, was provided by Carey and Rutledge (1996b) who observed negative specific differential phase (K_{dp}) shifts high in the storm above a tilted precipitation core and situated above the ground strike point of positive CG flashes. Negative values of K_{dp} aloft are suspected to be caused by the vertical orientation of ice crystals under the influence of a strong electric field. The observations of this storm appear to be consistent with the electrical characteristics of the earlier case study. Figure 6.1 is a conceptual model which illustrates the anomalous CG lightning characteristics observed in this study.

The tornado vortex signature associated with the visually-confirmed tornado was located along the interface of the updraft and the hail-induced downdraft of the hail curtain. The strong intensity of the updraft was inferred through observations of a positive differential reflectivity (Z_{dr}) column extending well above the freezing level. It is surmised that the close proximity of the updraft and this downdraft region was a fertile breeding ground for horizontal vorticity which could easily be tilted by the strong updraft and further amplified through stretching in this region of the storm. The number of radial velocity couplets located along the hail curtain adds some validity to this statement. Even though the mid-level mesocyclones of these cases co-evolved with the tornadoes' associated shear features, these rotation centers appear to be physically distinct. Conversely, this study is not implying that the mesocyclone did not create an environment favorable for the generation of the gust front and hail curtain or the formation of the tornadoes. These observations do suggest that the paradigm of a cascade of vorticity from the mesocyclone to the low-level tornado, envisioned in the "classical supercell" conceptual model, may not hold for all High Plains multi-cell storms. Although no evidence of a direct link between the "anomalous" CG lightning patterns and the formation of weak tornadoes was found, the main ingredient which appears absolutely essential for both phenomena is the existence of a well-organized and intense updraft. It is believed that an intense updraft capable of generating a thunderstorm which produces a dominance of positive CG lightning (when previous studies have shown that 97% of all CG flashes are of negative polarity in the Rock Mountain region) is also capable of producing an environment conducive to nonmesocyclone tornadoes. The dominance of positive CG lightning is characterized by the lack of negative CG flashes. Had there been a large number of negative CG flashes as typically expected, the electrification

of these storms may not have been judged anomalous. Therefore, dominant positive CG lightning storms could also be considered deficient negative CG producers.

6.2 Future Research

This study could only infer the bulk microphysical and kinematic characteristics of two positive lightning and weak tornado-producing thunderstorms occurring on the High Plains. With the advances in polarimetric-diverse radar observations, more accurate classifications of hydrometeor types should become available. In situ measurements are difficult to obtain, especially with the severe convection present in this study and could not provide the spatial resolution of radar observations. Therefore, it is imperative that the classification of hydrometeors through multiparameter weather radar observations be further refined and verified if significant advances are to be made.

A necessary tool for electrification studies would be a three-dimensional lightning detection and mapping system capable of sensing both cloud-to-ground and intracloud flashes along with their origins and discharge points. Indeed, such a lightning mapping system will be operational in northeastern Colorado during the summer of 1996 in support of the STERAO experiment. Further research also needs to be conducted on the charge carried by precipitation. The charge on precipitation particles is not clearly understood and requires additional laboratory and in situ measurements.

Many researchers have concentrated on the origin and formation of strong (F3 to F5) tornadoes most likely because of the widespread human injury and physical damage they inflict. Because of the low frequency of strong tornadoes in the High Plains, many have perceived that tornadoes are rare in association with High Plains thunderstorms. Obviously, the numerous tornado sightings from a single thunderstorm episode on 7 June 1995

contradict that perception. Researchers need to shift some attention away from investigating supercell thunderstorms toward multi-cell storms, concentrating on the origins of the low-level vertical vorticity with high spatial and temporal resolution. Perhaps closer inspection will reveal that the majority of tornadoes do not descend from a parent mesocyclone but rather co-evolve with it.

A goal of any severe storm research should be its application towards enhancing the detection and warning capabilities of the operational forecaster. A better understanding of nature and the atmosphere is a wonderful and fascinating process and should be readily shared with the operational community. More direct relationships between the observed CG lightning patterns and the occurrence of large hail and tornadoes would prove invaluable in the issuance of warnings to the general public.

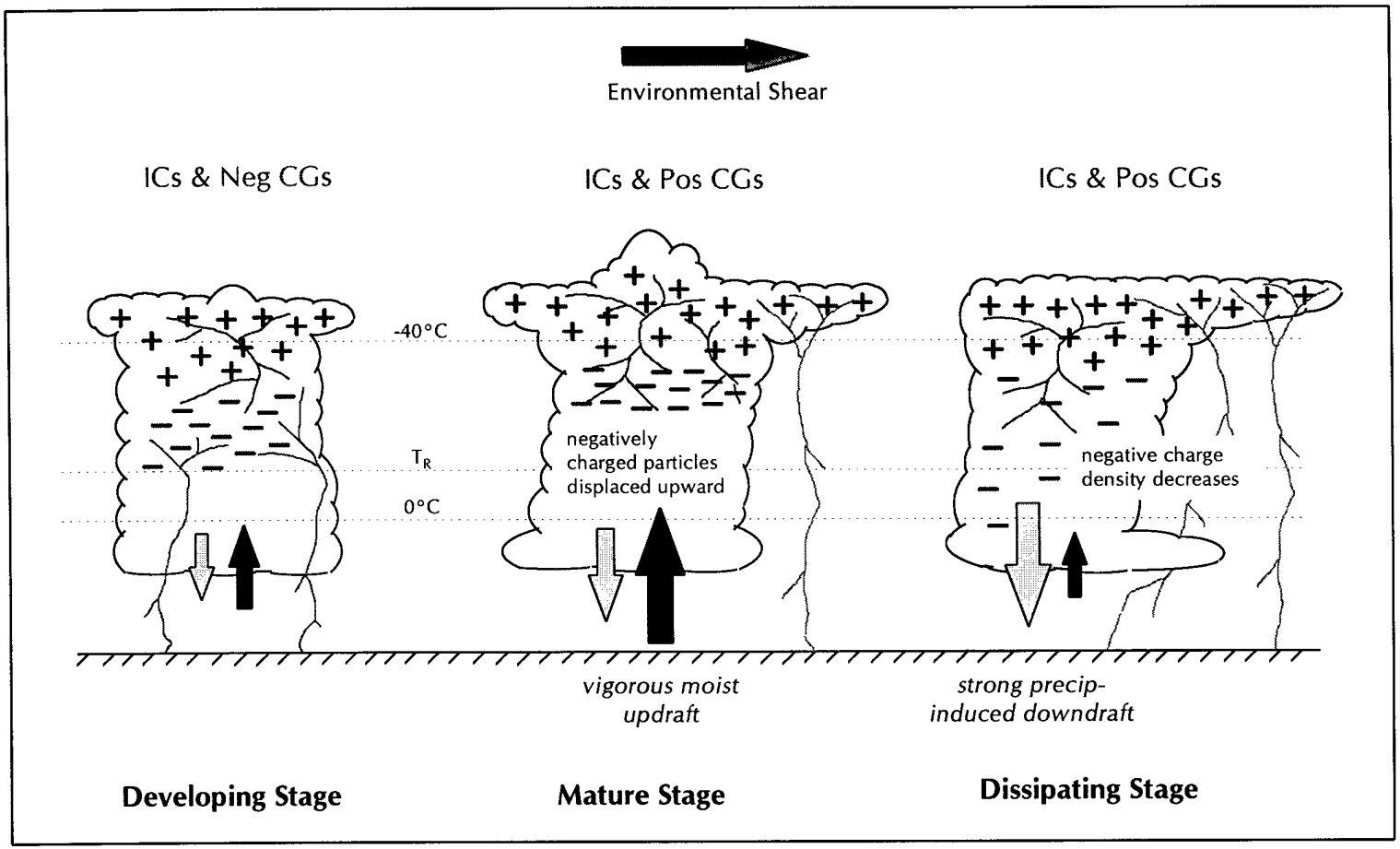

Fig. 6.1 Conceptual model depicting the life cycle of an anomalous CG lightning storm. The CG lightning pattern is considered anomalous because of the high ratio of positive to negative flashes. Left: Normal charge distribution resulting in a majority of negative CG flashes. Middle: Displacement of negative charge region along with strong upper-level shear resulting in dominant positive CG flashes. Right: Rapid collapse of mixed-phase region along with horizontal displacement of ice crystals allowing positive CG flashes to dominate.

REFERENCES

Armijo, L., 1969: A theory for the determination of wind and precipitation velocities with Doppler radar. *J. Atmos. Sci.,* **26,** 570-573.

Atlas, D., 1963: Radar analysis of severe storms. *Meteor. Monogr.,* No. 27, Amer. Meteor. Soc., 177-220.

Barnes, S. L., 1980: Report on a meeting to establish a common Doppler radar data exchange format. *Bull. Amer. Meteor. Soc.*, **61,** 1401-1404.

Battan, L. J., 1973: *Radar Observations of the Atmosphere.* University of Chicago Press, 324 pp.

Bluestein, H. B., 1985: The formation of a "landspout" in a "broken-line" squall line in Oklahoma. Preprints, *14th Conf. On Severe Local Storms*, Indianapolis, Amer. Meteor. Soc., 267-270.

——, 1993: *Synoptic-Dynamic Meteorology in Midlatitudes, Vol II: Observations Theory of Weather Systems.* Oxford University Press, 594 pp.

Bohne, A. R., and R. C. Srivastava, 1975: Random errors in wind and precipitation fall speed measurement by a triple Doppler radar system. *Lab. for Atmos. Probing Rep.*, No. 37, University of Chicago, 44 pp.

Brady, R. H., and E. Szoke, 1988: The landspout - A common type of northeast Colorado tornado. Preprints, *15th Conf. on Severe Local Storms*, Baltimore, Amer. Meteor. Soc., 312-315.

——, and ——, 1989: A case study of nonmesocyclone tornado development in northeast Colorado: Similarities to waterspout formation. *Mon. Wea. Rev.,* **117,** 843-856.

Brown, R. A., D. W. Burgess, J. K. Carter, L. R. Lemon and D. Sirmans, 1975: NSSL dual-Doppler radar measurements in tornadic storms: A preview. *Bull. Amer. Meteor. Soc.,* **56,** 524-526.

——, L. R. Lemon, and D. W. Burgess, 1978: Tornado detection by pulsed Doppler radar. *Mon. Wea. Rev.,* **106,** 29-38.

Browning, K. A., and F. H. Ludlam, 1962: Airflow in convective storms. *Quart. J. Roy. Meteor. Soc.,* **88,** 117-135.

Burgess, D. W., 1976: Single-Doppler radar vortex recognition. Part I: Mesocyclone signatures. Preprints, *17th Conf. on Radar Meteor.*, Seattle, Amer. Meteor. Soc., 97-103.

——, L. R. Lemon, and R. A. Brown, 1975: Tornado characteristics revealed by Doppler radar. *Geophys. Res. Lett.*, **2**, 183-184.

——, R. J. Donaldson, and P. R. Desrochers, 1993: Tornado detection and warning by radar. *The tornado: Its structure, dynamics, predictions and hazards, AGU Monogr.,* No. 79, Amer. Geophys. Union, 203-221.

Carey, L. D., and S. A. Rutledge, 1995: Positive cloud-to-ground lightning in severe hailstorms: A multiparameter radar study. Preprints, *27th Conf. on Radar Meteor.*, Vail, Amer. Meteor. Soc., 629-632.

——, and ——, 1996a: A multiparameter radar case study of the microphysical and kinematic evolution of a lightning producing storm. *Meteor. Atmos. Phys.*, **59,** 33-64.

——, and ——, 1996b: Electrical and multiparameter radar observations of a severe hailstorm. Preprints, *10th Int. Conf. on Atmospheric Electricity,* Osaka, Int. Commission of Atmos. Electricity, (in press).

Chandrasekar, V., V. N. Bringi, N. Balakrishnan, and D. S. Zrnić, 1990: Error structure of multiparameter radar and surface measurements of rainfall. Part III: Specific differential phase. *J. Atmos. Oceanic Technol.,* **7,** 621-629.

Cooley, J. R., 1978: Cold air funnel clouds. *Mon. Wea. Rev.*, **106**, 1368-1372.

Cressman, G. P., 1959: An operational objective analysis system. *Mon. Wea. Rev.,* **87,** 367-374.

Davies-Jones, R. P., 1979: Dual-Doppler radar coverage area as a function of measurement accuracy and spatial resolution. *J. Appl. Meteor.,* **9,** 1229-1233.

——, 1986: Tornado dynamics. *Thunderstorm Morphology and Dynamics,* E. Kessler, ed., University of Oklahoma Press, 197-236.

Doswell, C. A., 1980: Synoptic-scale environments associated with High Plains severe thunderstorms. *Bull. Amer. Soc.,* **61,** 1388-1400.

——, and D. W. Burgess, 1993: Tornadoes, and tornadic storms: A review of conceptual models. *The tornado: Its structure, dynamics, prediction, and hazards, AGU Monogr.,* No. 79, Amer. Geophys. Union, 161-172.

Doviak, R. J., and D. S. Zrnić, 1993: *Doppler Radar and Weather Observations,* 2nd ed. Academic Press, 562 pp.

Engholm, C. D., E. R. Williams, and R. M. Dole, 1990: Meteorological and electrical conditions associated with positive cloud-to-ground lightning. *Mon. Wea. Rev.,* **118,** 470-487.

Forbes, G. S., 1981: On the reliability of hook echoes as tornado indicators. *Mon. Wea. Rev.,* **109,** 1457-1466.

——, and R. M. Wakimoto, 1983: A concentrated outbreak of tornadoes, downbursts, and microbursts, and implications regarding vortex classifications. *Mon. Wea. Rev.*, **111,** 220-235.

Fujita, T. T., 1979: Objectives, operations, and results of Project NIMROD. Preprints, *11th Conf. On Severe Local Storms,* Kansas City, Amer. Meteorol. Soc., 259-266.

——, 1981: Tornadoes and downbursts in the context of generalized planetary scales. *J. Atmos. Sci.*, **38**, 1511-1534.

Fuquay, D. M., 1982: Positive cloud-to-ground lightning in summer thunderstorms. *J. Geophys. Res.,* **87,** 7131-7140.

Gaskell, W., 1979: Field and laboratory studies of precipitation charge. Ph.D. dissertation, University of Manchester.

Goodge, G. W., Ed., 1993: *Storm Data.* NOAA, U. S. Dept. of Commerce, 304 pp.

Illingworth, A. J., and J. Latham, 1977: Calculations of electric field structure and charge distributions in thunderstorms. *Quart. J. Roy. Meteor. Soc.,* **103,** 281, 295.

Jameson, A. R., 1985: Microphysical interpretation of multiparameter radar measurements in rain. Part III: Interpretation and measurement of propagation differential phase shift between orthogonal linear polarizations. *J. Atmos. Sci.,* **42,** 607-614.

JDOP Staff, 1979: Final report on the Joint Doppler Operational Project (JDOP) 1976-1978. *NOAA Tech. Memo. ERL NSSL-86*, 84 pp.

Klemp, J. B., 1987: Dynamics of tornadic thunderstorms. *Ann. Rev. Fluid Mech.*, **19,** 369-402.

Krider, E. P., R. C. Noggle, A. E. Pifer, and D. L. Vance, 1980: Lightning direction-finding systems for forest fire detection. *Bull. Amer. Meteor. Soc.*, **61,** 980-986.

Leise, J. A., 1981: A multidimensional scale-telescoped filter and data extension package. *NOAA Tech. Memo. ERL WPL-82*, 20 pp.

Lemon, L. R., 1980: Severe thunderstorm radar identification techniques and warning criteria. *NOAA Tech. Memo. NWS NSSFC-3,* 60 pp.

——, D. W. Burgess, and R. A. Brown, 1978: Tornadic storm airflow and morphology derived from single-Doppler radar measurements. *Mon. Wea. Rev.*, **106,** 48-61.

Lhermitte, R. M., 1964: Doppler radars as severe storm sensors. *Bull. Amer. Meteor. Soc.*, **45,** 587-596.

MacGorman, D. R., and W. L. Taylor, 1989: Positive cloud-to-ground lightning detection by direction-finder network. *J. Geophys. Res.*, **94,** 13,313-13,318.

——, and K. E. Nielsen, 1991: Cloud-to-Ground lightning in a tornadic storm on 8 May, 1986. *Mon. Wea. Rev.*, **119,** 1557-1574.

——, and D. W. Burgess, 1994: Positive cloud-to-ground lightning in tornadic storms and hailstorms. *Mon. Wea. Rev.*, **122,** 1671-1697.

Metcalf, J. I., 1995: Radar observations of changing orientations of hydrometeors in thunderstorms. *J. Appl. Meteo.*, **34,** 757-772.

Mohr, C. G., and L. J. Miller, 1983: CEDRIC—A software package for Cartesian space editing, synthesis and display of radar fields under interactive control. Preprints, *21st Conf. on Radar Meteor.*, Edmonton, Amer. Meteor. Soc., 569-574.

Nelson, S. P., and R. A. Brown, 1987: Error sources and accuracy of vertical velocities computed from multiple-Doppler radar measurement in deep convective storms. *J. Atmos. Oceanic Technol.*, **4,** 233-238.

Orville, R. E., Jr., 1991: Lightning ground flash density in the contiguous United States—1989. *Mon. Wea. Rev.*, **119,** 573-577.

——, R. W. Henderson, and L. F. Bosart, 1983: An East Coast lightning detection network. *Bull. Amer. Meteor. Soc.*, **64,** 1029-1037.

Oye, R., and R. E. Carbone, 1981: Interactive Doppler editing software. Preprints, *20th Conf. on Radar Meteor.,* Boston, Amer. Meteor. Soc., 683-689.

Peterson, W. A., 1992: Cloud-to-ground lightning in tropical mesoscale convective systems. M. S. thesis, Colorado State University, Fort Collins, 225 pp.

Price, C., and D. Rind, 1993: What determines the cloud-to-ground lightning fraction in thunderstorms? *Geophys. Res. Lett.,* **20,** 463-466.

Pruppacher, H. R., and K. V. Beard, 1970: A wind tunnel investigation of the internal circulation and shape of water drops falling at terminal velocity in air. *Quart. J. Roy. Meteor. Soc.,* **96,** 247-256.

Rankine, W. J. M., 1901: *A Manual of Applied Mechanics,* 16th ed. Charles Griffin and Company, 574-578.

Reap, R. M., and D. R. MacGorman, 1989: Cloud-to-ground lightning: Climatological characteristics and relationships to model fields, radar observations, and severe local storms. *Mon. Wea. Rev.,* **117,** 518-535.

Rust, W. D., D. R. MacGorman, and R. T. Arnold, 1981: Positive cloud-to-ground lightning flashes in severe storms. *Geophys. Res. Lett.,* **8,** 791-794.

——, ——, and S. J. Goodman, 1985: Unusual positive cloud-to-ground lightning in Oklahoma storms on 13 May 1983. Preprints, *14th Conference on Severe Local Storms,* Boston, Amer. Meteor. Soc., 372-375.

Rutledge, S. A., and D. R. MacGorman, 1988: Cloud-to-ground lightning activity in the 10-11 June 1985 mesoscale convective system observed during the Oklahoma-Kansas PRE-STORM Project. *Mon. Wea. Rev.*, **116,** 1393-1408.

——, C. Lu, and D. R. MacGorman, 1990: Positive cloud-to-ground lightning in mesoscale convective systems. *J. Atmos. Sci.*, **47,** 2085-2100.

Saunders, C. P. R., W. D. Keith, and R. P. Mitzeva, 1991: The effect of liquid water on thunderstorm charging. *J. Geophys. Res.,* **96,** 11,007-11,017.

Seimon, A., 1993: Anomalous cloud-to-ground lightning in an F5-tornado-producing supercell thunderstorm on 28 August 1990. *Bull. Amer. Meteor. Soc.,* **74,** 189-203.

Stolzenburg, M., 1994: Observations of high ground flash densities of positive lightning in summertime thunderstorms. *Mon. Wea. Rev.*, **122,** 1740-1750.

Takahashi, T., 1978: Riming electrification as a charge generation mechanism in thunderstorms. *J. Atmos. Soc.*, **35,** 1536-1548.

Takeuti, T., M. Nakano, M. Nagatani, and H. Nakada, 1973: On lightning discharges in winter thunderstorms. *J. Meteor. Soc. Japan*, **51,** 494-496.

Vonnegut, B., 1963: Some facts and speculations concerning the origin and role of thunderstorm electricity, *Meteor. Monogr., No.* 5, 224-241.

Wakimoto, R. M., and J. W. Wilson, 1989: Non-supercell tornadoes. *Mon. Wea. Rev.*, **117,** 1113-1140.

——, and N. T. Atkins, 1996: Observations on the origins of rotation: The Newcastle tornado during VORTEX 94. *Mon. Wea. Rev.*, **124,** 384-407.

Wilczak, J. M., T. W. Christian, D. E. Wolfe, R. J. Zamora, and B. B. Stankov, 1992: Observations of a Colorado tornado. Part I: Mesoscale environment and tornadogenesis. *Mon. Wea. Rev.*, **120,** 497-520.

Williams, E. R., 1989: The tripole structure of thunderstorms. *J. Geophys. Res.*, **94,** 13,151-13,167.

Yuter, S. E. and R. A. Houze, 1995: Three-dimensional kinematic and microphysical evolution of Florida cumulonimbus. Part II: Frequency distributions of vertical velocity, reflectivity, and differential reflectivity. *Mon. Wea. Rev.*, **123,** 1941-1963.

Zrnić, D. S., and R. J. Doviak, 1975: Velocity spectra of vortices scanned with a pulse-Doppler radar. *J. Appl. Meteor.*, **14,** 1531-1539.